Oxidation Behavior and Irradiation Effects of Co-free FCC High Entropy Alloys for Nuclear Application

Peng Bi

Division of Materials Science and Engineering

Graduate School of Engineering

Hokkaido University

February 2023

Acknowledgements

Here I would like to express my heartfelt gratitude to everyone who supported me during the long journey of my study. Without their help, I could not get Ph. D. and grow up to a young researcher.

Firstly, I want to give my hearty thanks to my supervisor, Professor Naoyuki Hashimoto. We met at the first time in 2017 winter when I visit Hokkaido University as an internship student during my master's. The journey aroused my great interest in research of nuclear materials by TEM observation. Two years later, I joined Prof. Hashimoto's group as a doctor student. I appreciate that I can conduct both corrosion and irradiation research even though I did not have much background in irradiation study. Also, I want to give many thanks to the guidance on regular individual meeting and manuscript preparation, as well as the opportunities to join a lot of conferences. These academic training broadened my view of research and let me know the proper ways of thinking and solving problems independently, which would be the most precious treasure in my study.

Secondly, I would like to say thank you to my defense committee members, especially for the examiners: Professor Seiji Miura, Professor Shigenari Hayashi and Professor Shigehoto Isobe. They provided encouraging and constructive feedback, and the indispensable discussion and advice are very much appreciated.

Also, I want to give my thanks to the group members. Thanks to Professor Shigehoto Isobe for his timely advice and encouragement, and many thanks to Professor Oka in irradiation group for his enthusiastic discussions and technical support whenever I need it. Thanks to our assistant, Ms. Kobayashi, for her efficient support in the daily routines

providing us better research and living environment. Thanks to our group students and OBs, I really learned a lot from you, both the wisdom in experimental and the way of thinking. I will not forget your kindness and the good time we spent together.

Moreover, I would like to express my special thanks to Professor Shigenari Hayashi in the neighbor group. Hayashi sensei allowed me to conduct oxidation experiments in his lab and guided me with efficient and valuable discussions, he is the person who led me into high temperature oxidation research.

Furthermore, I would like to give my thanks to all the professors and technical staffs who support me during my study, especially for the technical support from Dr. Takashi Endo, Dr. Yongming Wang, Mr. Atsuki Sawa, Mr. Yu Uchida and Ms. Yurika Yamanouchi in Laboratory of Nano-Micro Material Analysis, Mr. Keita Suzuki in Laboratory of XPS analysis and Ms. Yuko Mori in Research Institute for Electronic Science, and the nano-indentation experiment support from Professor Kenichi Ikeda and Professor Ryuta Kasada (Tohoku University), ion irradiation experiment support from Professor Kiyohiro Yabuuchi (Kyoto University). Also, thanks to the project foundation in our group and thanks to China Scholarship Council for providing the scholarship for my oversea study.

Finally, I want to say thank you to my parents, for their continuous support and care over three decades. I will be stronger and make you proud of me, I believe.

Abstract

The research and development of advanced nuclear power systems are critically important for achieving the goals of carbon neutrality by 2060. Generation IV reactors such as supercritical water-cooled reactors (SCWR) and gas-cooled fast reactor (GFR) require much higher outlet temperatures (550-850°C) and radiation doses (up to 100-200 dpa), which are out of the tolerance limits of the current austenitic stainless steels and ferritic/martensitic steels. New structure materials with high corrosion and irradiation resistance are urgently required for extended use at high temperatures and high doses. Co-free high entropy alloys (HEA) attract many concerns due to the reduced radioactivity and high-temperature stability, which could be one of the candidate materials for next-generation nuclear reactor components. This dissertation contains research work attempting to develop Co-free Cu-containing HEAs and evaluate their oxidation and irradiation resistance by comparison with traditional alloys. The steam oxidation behavior and irradiation effects of these alloys were investigated.

First of all, a group of Co-free concentrated solid solution alloys (CSSA): CuNi, CuNiFe, $Cu_{0.3}$CrFeNi and $Al_{0.4}$CrCuFeNi$_2$ HEAs are successfully prepared by arc melting, followed by solution annealing process to obtain simple FCC structure. The alloys were oxidized in the atmospheres containing water vapor at 500, 600, and 700°C for 25 h in order to evaluate the oxidation performance. The oxidation of all the Cu containing alloys indicated parabolic behavior, and those appeared to have better corrosion resistance than normal 316 SS. The parabolic rate constant increased with increasing temperature. Cross-sectional electron probe microanalysis (EPMA) and X-ray diffraction (XRD) results revealed that the addition of Cr and Al significantly improved the oxidation resistance of

the alloys. $Al_{0.4}CrCuFeNi_2$ showed the best oxidation resistance in this study probably due to the formation of protective Cr_2O_3 and Al_2O_3 oxide scale.

Secondly, in order to understand the effect of Al content on the oxidation resistance of HEAs, three FCC-typed $Al_xCrCuFeNi_2$ HEAs (x = 0.2, 0.4, 0.6) with increasing Al concentration were selected to investigate the steam oxidation behavior at 700 °C. The invested HEAs show FCC matrix with ordered $L1_2$ nanoscale precipitates, and their Vickers microhardness increased with increasing Al content. The mass gain of each alloy follows the order of $Al_{0.6}CrCuFeNi_2$ < $Al_{0.4}CrCuFeNi_2$ < $Al_{0.2}CrCuFeNi_2$ after 100 h oxidation. $Al_{0.2}CrCuFeNi_2$ HEA showed two-stage oxidation kinetics with an initial fast-growing stage before 25 h and a slow-growing stage within 100 h, while $Al_{0.4}CrCuFeNi_2$ and $Al_{0.6}CrCuFeNi_2$ HEAs show single parabolic rate constants. Detailed analysis by XRD, EPMA and STEM element mapping shows that the lower solute concentration of Al in $Al_{0.2}CrCuFeNi_2$ alloy led to a discontinuous Al_2O_3 distribution and much thicker Fe-Ni rich spinel oxides formation. By increasing Al content, the oxide scale thickness decreased significantly by the establishment of continuous external Cr_2O_3 and Al_2O_3 oxide scales. The analysis of short-term oxidation indicates that the early formation of continuous Al_2O_3 scale in the initial stage of oxidation contributes to the enhanced oxidation resistance of high Al content alloys.

At last, the irradiation effects of $CrCu_{0.3}FeNi$ and $Al_{0.4}CrCuFeNi_2$ HEAs were evaluated by comparison with commercial 316L SS, and the irradiation-induced hardening were correlated with the irradiated microstructure by TEM observation. The specimens were irradiated with 6.4 MeV Fe^{3+} at 300 °C to a nominal damage peak of about 23 dpa at 1.5 μm using DuET facility. The surface morphology acquired by atomic force microscope (AFM) shows a decrease in step height from 7.2 nm in 316L to 4.6 nm

in $CrCu_{0.3}FeNi$, indicating a lower surface swelling of HEA. Nano-indentation experiments at a depth of 250 nm showed that $Al_{0.4}CrCuFeNi_2$ HEA exhibit lower irradiation hardening (0.8GPa) than 316L (1.5GPa), while the continuous stiffness measurement (CSM) indicated a comparable hardening of HEAs with 316L. The transmission electron microscope (TEM) microstructure observation by dark field images taken from the relrod of each specimen suggests that the HEAs have similar averaged number density of Frank loop with 316L in the whole damage region. However, 316L tends to show a higher loop number density than HEAs in a shallower depth while HEAs present a wider damage distribution and larger amount of defects than 316L in deeper irradiation area, which is consistent with the higher irradiation hardening tested by single depth indentation at 250 nm and a similar hardening behavior by CSM indentation (0-2 μm). The measured hardening and corresponding defect microstructure observed indicate a comparable irradiation resistance of $CrCu_{0.3}FeNi$ and $Al_{0.4}CrCuFeNi_2$ HEAs with 316L in the current irradiation condition.

This work indicated that Co-free $Al_{0.4}CrCuFeNi_2$ HEA possess outstanding oxidation resistance at high temperatures and comparable irradiation resistance with conventional stainless steels, which could be potential candidate materials for advanced nuclear reactors.

Contents

List of Figures

List of Tables

Chapter 1 Introduction

1.1 Materials for advanced nuclear energy system

Global warming is one the most serious problem to humanity. In order to achieve the goals of carbon neutrality by 2050, a major changing of the energy supply system is needed. Nuclear energy is considered to be a zero-CO_2 emission energy source, which could replace the consumption of fossil fuel energy sources economically in a sustainable way [1].

Currently, the most commertial applied reactors are mainly Generation II or Generation III light water reactors, including pressurized water reactor (PWR) and boiling water reactor (BWR). **Fig. 1.1** shows the schematic of key components in PWR [2]. The survice condition of structure materials in the primary circuit of PWR would combined with high temperature and pressure corrosion and irradiation. The outlet temperature between 290-320℃, total amount of irradiation dose about 7-80 displacement per atom (dpa, widely used as an exposure unit of damage levels for materials in radiation environments) in the whole operation lifetime. Conventional 304 and 316 SS were widely applied in the primary piping and core structures due to its considerable mechanical and corrosion properties and relative low costs. However, the fast-growing global electricity demand and the limited supply of uranium aroused much corncern for developing new advanced reactors with higher efficiency and longer lifetime with enhanced safety.

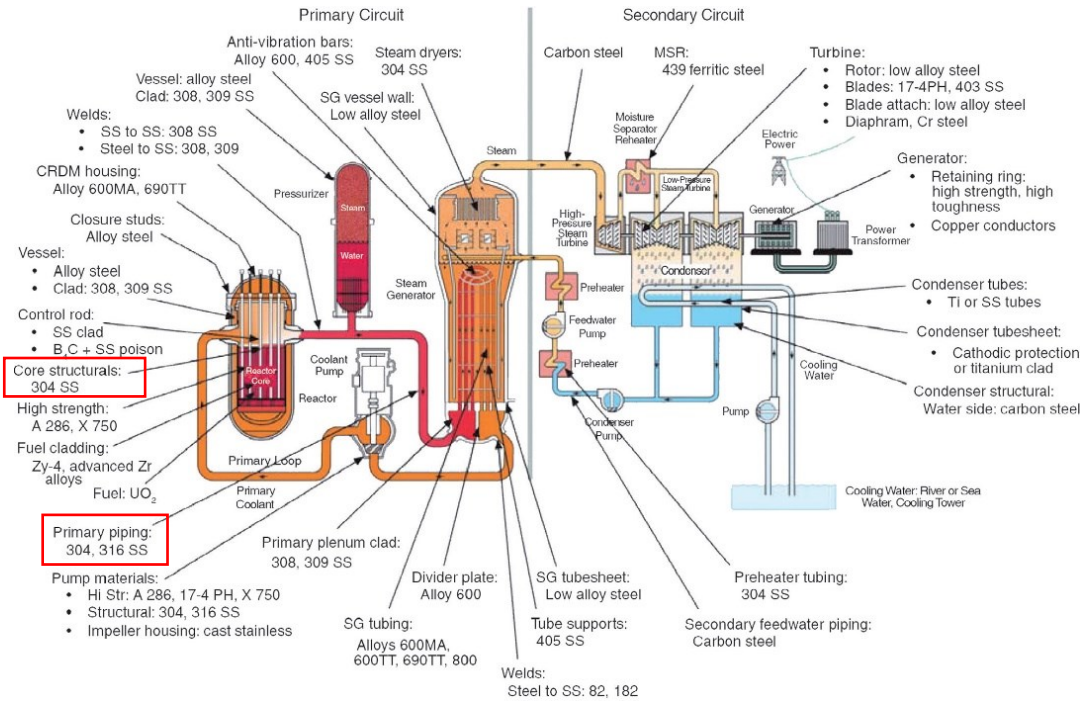

Fig. 1.1 Schematic of key components in pressurized water fission reactor [2].

Over the past 20 years, advanced reactor concepts as potential next-generation (Generation IV) nuclear power systems has been explored by the United States Department of Energy and the Generation IV International Forum (GIF). The objective was to identify concepts that had one or more of the following attributes: increased efficiency, generation of process heat to drive chemical processes such as the production of hydrogen, increased safety and reduction in waste generation. The GIF has selected six reactor technologies for further research and development: the supercriticalwater-cooled reactor (SCWR), the sodium fast reactor (SFR), the lead fast reactor (LFR), the very-high-temperature reactor (VHTR), the gas fast reactor (GFR) and the molten salt reactor (MSR). **Fig. 1.2** shows the temperature and dose requirements for in-core structural materials for the operation of the six proposed Generation IV advanced reactor concepts [2]. Note that almost all designs of the Generation IV concepts call for higher operating temperatures (>500°C) and radiation

damage levels (15-150 dpa) than those of Generation II - III reactors.

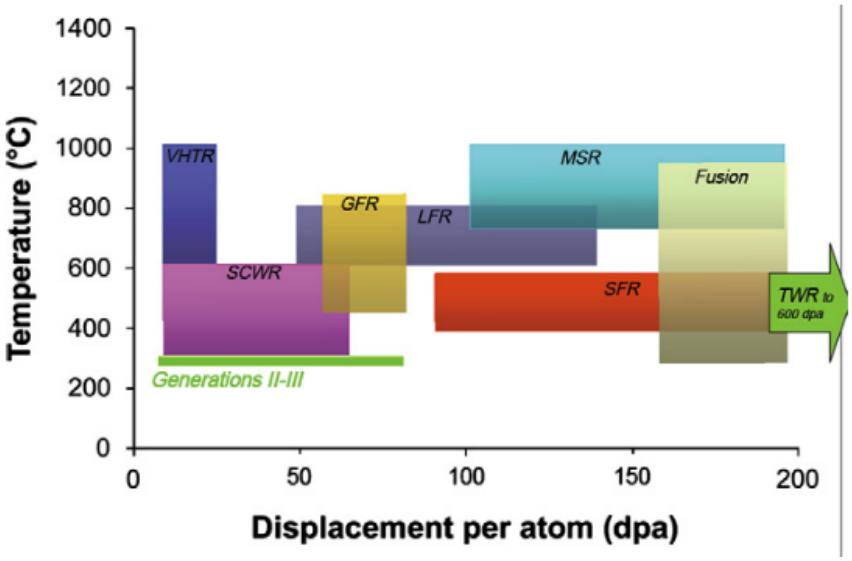

Fig. 1.2 Temperature and dose requirements for in-core structural materials for the operation of the six proposed Generation IV advanced reactor concepts, the traveling wave reactor and fusion reactor concepts. The dimensions of the colored rectangles represent the ranges of temperature and displacement damage for each reactor concept [2].

The materials challenges for the Generation IV reactor concepts come about because of the very high fuel temperatures, the intense radiation flux and coolant compatibility issues. Thus, the fuel, the cladding, the structural materials, the reactor vessel and the interaction of these materials with the coolants present the greatest challenges to new, more robust nuclear reactor concepts for the twenty-first century. Structural materials used in the cores of advanced reactors will face unprecedented combinations of temperature, radiation dose and stress. The major materials challenges for the current and next generation of water-cooled fission reactors are centered on corrosion and stress corrosion cracking of structural materials and neutron-induced embrittlement of reactor pressure vessels, along with improved fuel system reliability and accident tolerance issues.

Traditional austenitic stainless steel and ferritic-martensitic steel will face severe swelling and hardening under high temperature and high radiation dose, which can no longer meet the development needs of the next generation of nuclear reactors. Void swelling is an irradiation effect of volumatic change that can result in dimensional instability and undermine the safe operation of nuclear reactors. It occurs at homologous temperatures of 0.35-0.55 T_M, which for steels (325-650 °C) overlaps the temperature range of the reactor core for these four high-temperature, high-dose concepts. **Fig. 1.3** compares the void swelling behavior for type 304L, 316 SS, Ti-modified austenitic stainless steel and 9-12% Cr-tempered ferritic/martensitic steels [3-5] irradiated at 400-550 °C to high doses. It can be found that 304 and 316 SS both reached a high void swelling levels >5% which is unacceptable based on typical engineering design considerations. Although more radiation-resistant alloys such as 9-12 Cr FM steel are being considered for high-dose, the phase instability due to radiation-induced or enhanced solute segregation and ballistic dissolution of precipitates by energetic displacement cascades is another problem.

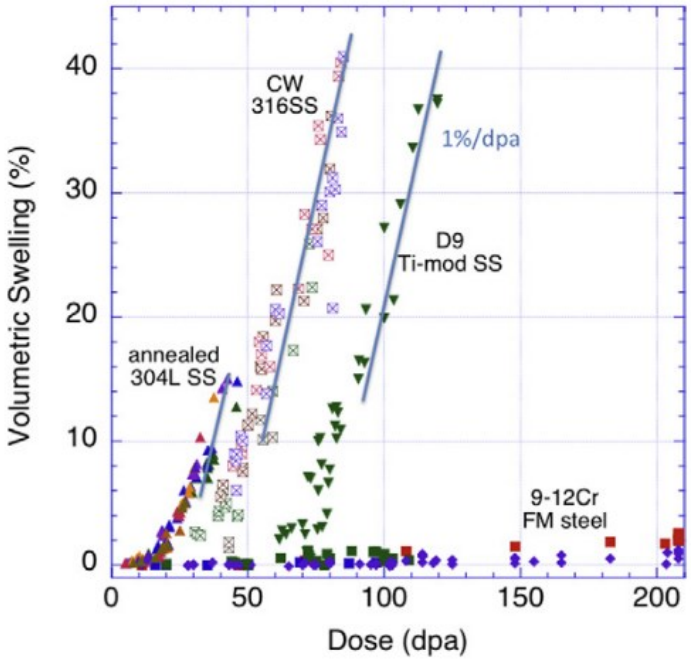

Fig. 1.3 Comparison of the volumetric void swelling behavior of Type 304L, 316 [5] and a Ti-modified (D9) [5] austenitic stainless steel and 9–12% Cr-tempered ferritic/martensitic steels [3-5] following irradiation at 400–550 °C to high doses in a fast fission reactor spectrum.

To date, the research and development of advanced radiation-resistant and oxidation-resistant materials is still a key technical problem restricting the practical application and sustainable development of nuclear energy systems. Therefore, the design and development of a new generation of new alloys with excellent mechanical properties, oxidation resistance, as well as radiation resistance has important scientific significance and engineering application value for solving the material bottleneck problem and improving the long-term safe and stable operation of nuclear power plants.

1.2 Research and development of high entropy alloys

1.2.1 Overview and recent progress

In recent years, high-entropy alloys (HEAs) or multi-principal high-concentration solid solution alloys (CSSAs) are expected to achieve the combination of mechanical properties, high-temperature oxidation resistance, and radiation resistance due to their high mixing entropy, lattice distortion, slow diffusion, and cocktail effect. Research and development of HEAs has become a research hotspot in the field of nuclear materials [6-10]. In contrast from the conventional diluted alloys stand in corners and edges of multicomponent phase diagrams, the CSSAs and the HEAs contain 5 or more elements in equiatomic or near equiatomic ratios with element concentrations between 5 % and 35 %, which lies in the centre of multicomponent phase space and are highly stabilized due to high configurational entropy.

Since 2004, Cantor and Yeh independently found the FeCoCrNiMn [6] and $Al_xCuCoCrFeNi$ (x= 0 ~ 0.5) [11] alloy with a single face-centered cubic (FCC) structure, an increasing group numbers of researchers focus on the development of HEAs with single phase (FCC or BCC), dual phase or multi-phases. The early study mainly concentrated on the single phase HEAs fabrication and mechanical properties characterization. Recently, the society is more kind to accept HEAs with multi-phases (eg: FCC+$L1_2$, FCC+BCC, BCC+B_2), which could benefit from the cocktail effect to obtain the combined properties.

Fe-based high-entropy alloys have attracted continuous attention due to their excellent mechanical properties (ductility, fracture toughness). In order to further improve the strength of the alloy, researchers have carried out a lot of exploration from different angles such as plastic deformation, grain refinement, and addition of precipitated phase elements [12-14]. Recently, the method of constructing ordered $L1_2$ nano-precipitation strengthening in the FCC matrix is considered to be an effective method to simultaneously obtain strength and plasticity, which coincides with the idea of γ/γ' precipitation strengthening in nickel-based superalloys [15-17].

Considering about the long-term stable operation of nuclear power plants, the content of high radioactive elements (such as ^{60}Co) in structural materials needs to be effectively controlled. Reduced activation HEAs, especially Co-free HEAs should be well developed. Guo et al [18, 19] removed the high radioactive Co with Ni in the $Al_xCoCrCuFeNi$ HEA and studied the phase stability and mechanical properties of the $Al_xCrCuFeNi_2$ HEAs. They found that the alloy tended to show FCC single phase within the composition range of $x < 0.7$, and show BCC and B_2 phase when $x > 1.5$. The followed researchers subsequently found that nano-sized ordered $L1_2$ phase and copper-rich phase can be precipitated in the FCC matrix through different

homogenization annealing and aging processes, and the $L1_2$ precipitates can remain stable in a large temperature range, which provides a potential for improving the high-temperature mechanical properties of the alloy [19-22].

1.2.2 Oxidation resistance of HEAs

Generally, high oxidation resistance of the alloys can be achieved by forming a barrier between the matrix and the oxidizing environment through a dense oxide layer that quickly forms and grows slowly on the surface of the alloy at high-temperature, and the protective scale could prevent further oxidation of the alloys.

According to the Gibbs free energy of oxides formation and high-temperature stability of metal oxides, Cr and Al elements are widely added to alloys aims to form chromium oxide (Cr_2O_3) and aluminum oxide (Al_2O_3) protective layers, which can effectively improve the high-temperature oxidation performance. However, the formation of a stable outer oxide layer requires the addition of a large amount of oxide-forming elements, which is often difficult to achieve in traditional single principal alloys due to the limitation of brittle phase formation, while high-entropy alloys are suitable for forming highly alloyed single concentrated solid solution. In recent years, the high-temperature oxidation performance of high-entropy alloys has attracted continuous attention and has become a research hotspot in the field of corrosion.

Liu et al. [23] reported the high-temperature oxidation behavior of $CoCrFeNiAl_x$ HEAs and HR3C steel in supercritical water environment, and they found that the HEAs exhibited better oxidation resistance at 550-600 °C. Mohanty [24] and W. Kai [25] studied the effect of Al content on the high-temperature oxidation behavior of $Al_xCoCrFeNi$ and $Al_xCoCrFeNi_2$ high-entropy alloys, founding that the oxidation resistance can be enhanced by increasing the Al content to control the structure,

thickness and continuity of the oxide layer. In addition, the preparation of high-entropy alloy thin films on the surface of traditional alloys can also effectively improve their oxidation resistance, which has become a new way to improve the high-temperature oxidation performance of traditional materials [26].

However, there are few reports on the high-temperature oxidation of Co-free high-entropy alloys. In summary, the study of the high-temperature oxidation behavior of cobalt-free high-entropy alloys is of great significance for the practical application of nuclear power materials.

1.2.3 Irradiation effects of HEAs

Irradiation-induced degradation of material properties is an important issue in the development of nuclear energy system. Ion irradiation technology is an effective method for simulating the irradiation damage of reactor neutrons to materials by using the heavy ion beam generated by the accelerator to produce lattice dislocation atoms through the cascade collision process. Compared with the neutron irradiation experiment, it has the advantages of reaching a high irradiation dose in short time period, and the ion irradiated materials are non-radioactive which can be characterized safely without time delay. There are many kinds of beam lines or accelerators which can conduct heavy-ion irradiation in the world, such as Argonne National Laboratory (IVEM), Japan Atomic Energy Agency (TIARA), Kyoto University (DuET) [27], and Tokyo University (HIT). The main topic of ion irradiation experiment focus on the mechanical properties (hardness) and defect microstructure evolution of materials under different temperatures, ion sources, and irradiation doses.

In terms of the evaluation of the radiation damage behavior of high-entropy alloys,

W.Y. Chen et al. [28, 29] used in-situ transmission electron microscopy to study the $Al_{0.3}$CoCrFeNi, CoCrFeMnNi HEAs and 316H under different irradiation temperatures under Kr ion irradiation. It is found that the size and number density of dislocation loops formed in HEAs are close to those of 316H, and the degree of radiation hardening is equivalent at 300°C; however, at higher temperature of 500°C, compared with 316H, HEAs exhibited larger dislocation loops size and smaller number density, and lower irradiation hardening, indicating potentially excellent radiation resistance of HEAs at high temperatures (>500 °C). Hashimoto et al. [30, 31] systematically studied the irradiation defect morphology of CoCrFeNiMnx high-entropy alloy and Co-free $FeCr_{0.8}Ni_xMn_y$ HEAs under Fe^{3+} ion irradiation, by calculating the stacking fault energy in the deformed sample, the influence of Ni, Mn content on stacking fault energy and the correlation between stacking fault energy and irradiation defect evolution are discussed. The results show that the stacking fault energy in the alloy system increases with the increase of Ni and Mn content, and the alloy with high Ni/Mn content shows lower dislocation density and radiation hardening degree. The perspective provides a research idea for improving the radiation resistance. Recently, E.G. Fu and Z. P. Lu et al. [32] discovered the defect annihilation behavior of coherent nanoparticles, revealed the defect annihilation mechanism of its cyclic dissolution and re-precipitation, and proposed a design with small lattice mismatch and large composition tolerance. High-density nanoparticles can greatly improve the swelling resistance, and this strategy has been proved effective in martensitic steels and medium-entropy alloys, and is expected to be applied in alloy material systems such as high-entropy alloys.

In summary, it is of importance to study the radiation damage behavior of nuclear materials by ion irradiation and evaluate their radiation resistance for future applications. Evaluating the radiation damage effect of HEAs and understanding of

their radiation-resistant mechanism is helpful for alloy design and improvement of materials reliability for practical application of new nuclear power plants.

1.3 Objective and strategy

The development of next generation nuclear systems for higher efficiency and longer lifetime requires the new structure materials with enhanced properties of corrosion and radiation resistance. The oxidation and irradiation behavior of HEAs has limited studies, especially for Co-free HEAs with reduced radioactivity. Thus, the element effects and oxidation kinetics of Co-free HEAs should be well investigated in order to applied at high temperatures. Besides, Irradiation-induced degradation of material properties is another important issue in the development of nuclear energy system.

The objective of this study is to develop Co-free Cu containing HEAs and evaluate the oxidation resistance and irradiation effect at high temperature and irradiation dose as potential candidate materials for advanced reactors. The formation of protective Al_2O_3 scale is expected on the surface of $Al_xCrCuFeNi_2$ HEAs to improve its oxidation resistance. The damage microstructure and irradiation hardening effect of the alloys will be estimated with comparison of conventional alloy in order to applied on radiation conditions.

So far, limited research on the development of Co-free HEAs has been conducted, especially for the evaluation of oxidation and irradiation behavior. Therefore, the findings of the present work will provide insights into materials design and modification for high temperature nuclear applications.

1.4 Dissertation structure

In chapter 1, the materials challenges and advantages of high entropy alloys for advanced nuclear energy system was introduced. Moreover, the background and objectives of this study were illustrated.

In chapter 2, fundamental theories of high temperature oxidation and irradiation were briefly introduced, and technical methods used in this study were identified.

In chapter 3, the element effect and temperature dependence on oxidation behavior of concentrated solid solution alloys (CSSAs, CuNi, CuNiFe), HEAs ($Cu_{0.3}CrFeNi$, $Al_{0.4}CrCuFeNi_2$) and 316 SS were investigated. The steam oxidation experiment conducted at 500, 600, and 700°C for 25 h indicated a better corrosion resistance of HEAs than normal 316 SS. Cross-sectional electron probe microanalysis (EPMA) and X-ray diffraction (XRD) results revealed that the addition of Cr and Al significantly improved the oxidation resistance of the alloys, and the $Al_{0.4}CrCuFeNi_2$ showed the best oxidation resistance due to the formation of protective Cr_2O_3 and Al_2O_3 oxide scale.

In chapter 4, the effect of Al content on the oxidation resistance of $Al_xCrCuFeNi_2$ HEAs (x = 0.2, 0.4, 0.6) were studied at 700 °C in steam. The oxidation kinetics of all the alloys followed parabolic behavior, with their oxidation rates decreasing with increasing Al concentration. Thick triplex oxide scales with discontinuous Al_2O_3 formed on the $Al_{0.2}CrCuFeNi_2$ alloy, while a continuous Al_2O_3 layer and thinner spinel oxide scale grew on $Al_{0.4}CrCuFeNi_2$ and $Al_{0.6}CrCuFeNi_2$ alloys. The Al content of $Al_{0.2}CrCuFeNi_2$ alloy were found to be the border line of external Al_2O_3 formation. Short-term oxidation analysis indicates that the early formation of continuous Al_2O_3 scale in the initial stage of oxidation contributes to the enhanced oxidation resistance of high Al content alloys.

In chapter 5, the irradiation effects of $CrCu_{0.3}FeNi$ and $Al_{0.4}CrCuFeNi_2$ HEAs were evaluated by comparison with commercial 316L SS, and the irradiation hardening were correlated with the irradiated microstructure by TEM observation. The lower step height of irradiated and unirradiated region in CrCu0.3FeNi than 316L indicated a higher swelling resistance of HEA. Two types of nano-indentation experiments: single depth indentation showed a higher irradiation hardening of 316L (1.5GPa) than $Al_{0.4}CrCuFeNi_2$ HEA (0.8GPa), while no significant difference of hardening behavior was found by continuous stiffness measurement (CSM) indentation. The dark field TEM images suggests that the HEAs have similar averaged number density of Frank loop with 316L in the whole damage region. However, in a shallower depth, 316L tends to show a higher loop number density than HEAs. In deeper irradiation area, HEAs present a wider damage distribution and slightly larger amount of defects than 316L, which is reasonable for the higher irradiation hardening tested by single depth indentation and a similar hardening behavior by CSM indentation.

In chapter 6, the main conclusions and most relevant findings of this study are summarized.

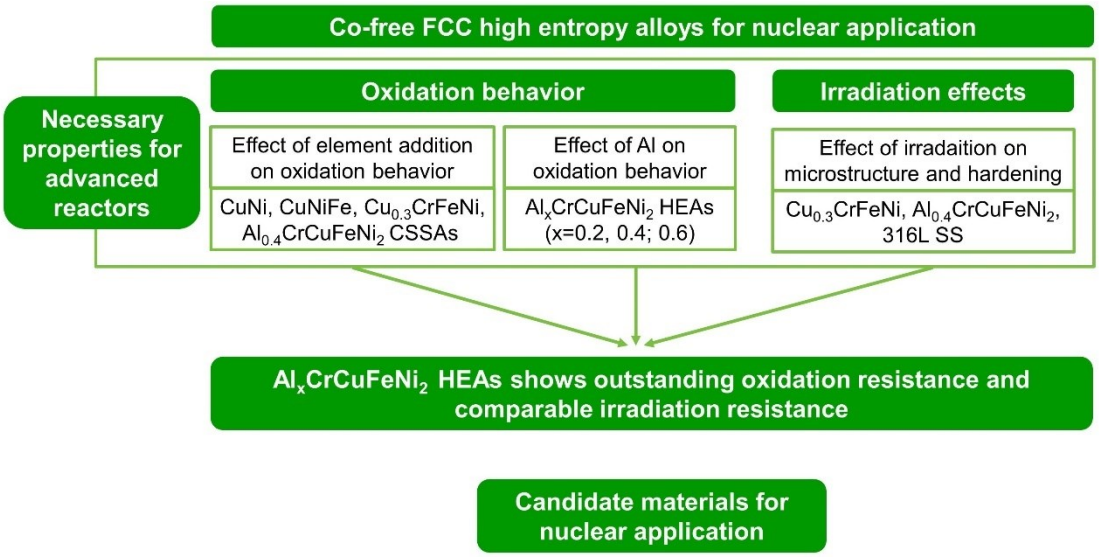

Chapter 2 Fundamentals and Methodology

2.1 High temperature oxidation theory

2.1.1 Oxidation of alloys

At high temperatures, most metals will inevitably oxidize over a wide range of conditions. The alloys and coatings employed for heat-resisting applications are usually based on iron, nickel or cobalt and contain Cr and/or Al to provide protective oxide scales. The choice of Cr and Al is based on the slow rate at which their oxides grow and the fact that these oxides are considerably more stable than those of iron, nickel or cobalt. Thus, Cr_2O_3 and Al_2O_3 are thermodynamically favored and will form preferentially if this is kinetically possible.

In an initial, transient stage, all reactive alloy components oxidize, yielding a product with essentially the same relative proportions of metallic constituents as the parent alloy. Subsequently, local equilibrium is achieved at alloy-scale and scale-gas interfaces, and steady-state reaction follows. During this stage, the scale morphology and composition are invariant with time.

By far the most common method of measuring oxidation rates is the observation of oxide accumulation with time, gravimetric measurements can be performed continuously with a microbalance or discontinuously by weighing a series of samples subjected to different reaction times. The discontinuously measurement is helpful for understanding the oxidation process and check the cross sections of the samples after different duration of oxidation.

The measured weight change (ΔW) of the alloys can be divided to two groups: weight loss and weight gain. The weight loss of the alloys mainly due to the poor adhesion of the oxide scale and the matrix, resulting in the spallation of the oxides. On the other hand, if the oxides formed on the alloy surface is stable with no metal

volatilization or the oxides formed internally, then mass gain corresponds to oxidant uptake can be measured.

According to the relationship between the obtained mass gain per unit area (ΔW/A) with the oxidation time, the oxidation kinetics of different alloys can be divided as follows:

(1) Linear kinetics

$$\Delta W/A = k_1 \cdot t,$$

k_1 is the linear rate constant, under certain conditions the oxidation of a metal proceeds at a constant rate, the linear rate law is usually observed where a phase-boundary process is the rate-determining step for the reaction. Principally, diffusion through the scale is unlikely to be rate limiting when the scale is thin, i.e. in initial stage of process. In this case, the metal-oxide and oxide-gas interfaces cannot be assumed to be in thermodynamic equilibrium although there are a few cases that the reaction at metal-scale interface play a rate-determine role. It can be assumed that the reaction occurring at the metal-scale interface are fast, and attention can be turned to the process occurring at the scale-gas interface for an interpretation of the linear rate law.

(2) Parabolic kinetics

$$(\Delta W/A)^2 = k_2 \cdot t \text{ or } \Delta W/A = (k_2 \cdot t)^{1/2},$$

k_2 is the parabolic rate constant, it indicates that the process is diffusion controlled, in which ideal protective scale growth on the alloy. More generally, $(\Delta W/A)^n = k_2 \cdot t$ or $\Delta W/A = (k_2 \cdot t)^{1/n}$ was used to evaluate the parabolic kinetics.

(3) Logarithm growth law

$$\Delta W/A = k_3 \cdot \log (Ct + A),$$

indicate the fast oxidation at the start, and the rate decreases to a low value.

2.1.2 Selective oxidation and third element effects

Selective oxidation will occur if only one oxide is stable. This is the case for alloys consisting of a noble metal such as Pt, Ag or Au, which does not form an oxide under normal conditions, and a reactive metal, which does. An example of this alloy class is Pt-Ni. It is also the case for more practically relevant alloy systems such as Fe-Cr and Ni-Cr, if the ambient oxygen potential is below the minimum necessary to form any iron or nickel bearing oxide but still above the value required for Cr_2O_3 formation. Successful alloy design leads to the selective oxidation of a particular alloy component, forming a slow-growing and protective oxide scale.

The third element in question is that component of a ternary alloy which forms an oxide of stability intermediate to those of the other two metals. Thus chromium is the third element in both Ni-Cr-Al and Fe-Cr-Al. Early work on the Cu-Zn-Al system showed that ternary alloys formed protective Al_2O_3 scales at lower N_{Al} values than were required for Cu-Al binaries. The explanation lay in the ability of Zn (the third element) to lower the oxygen activity at the scale-alloy interface, which was called ‘‘third element effect’’. The third element reduced the value of minimum supply for protective scale formation (eg: $N_{Al,min}$ for establishment of a protective Al_2O_3 scale).

2.1.3 Internal and external oxidation

(1) Internal oxidation, external oxidation and exclusive oxidation.

When an alloy component is selectively oxidized but cannot reach the surface quickly enough to develop a scale, then internal oxidation results. We consider an alloy AB exposed to an oxygen potential high enough to react with B, but not with A, and suppose that alloy diffusion is negligible compared with inward oxygen movement. Internal oxidation will result if the oxygen solubility in the B-depleted alloy ($N_o^{(S)}$), and

its diffusion coefficient (D_o) are high enough. The ideal exclusive oxide was supposed to show the best oxidation resistance due to the single protective oxide scale formed above the initial surface of the alloy. However, in many cases, multiple scales can be formed externally.

Fig. 2.1 shows the effect of alloy chromium content on oxidation behavior of Fe-Cr alloy [33]. It can be found that, dilute alloys (Fe-5Cr) form only internal oxide, while Fe-10Cr forms both external and internal oxide and Fe-17Cr forms only an external scale.

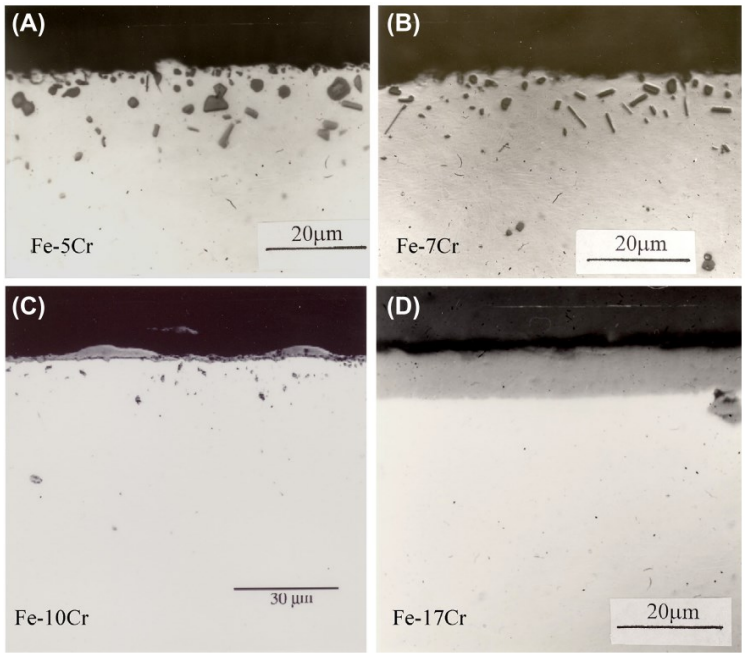

Fig. 2.1 Change in oxide morphology with composition of Fe-Cr alloys exposed to P_{O2}=8.7×10^{-17} atm at 1000℃: (A) Fe-5Cr; (B) Fe-7Cr; (C) Fe-10Cr; (D) Fe-17Cr [33].

(2) Transition from internal oxidation to external oxidation

The critical content for an external oxide BO formation (N_B^O) can be estimated by the equation [34]:

$$N_{\mathrm{B}}^{\mathrm{O}} = (\mathrm{g}_{\mathrm{BO}}^{*} \frac{\pi}{2v} \frac{V_{\mathrm{A}}}{V_{\mathrm{OX}}} \frac{N_{\mathrm{O}}^{(\mathrm{s})} D_{\mathrm{O}}}{D_{\mathrm{B}}})^{1/2}$$

Where $\mathrm{g}_{\mathrm{BO}}^{*}$ is the specified volume fraction of BO, V_{A} and V_{OX} are the molar volumes of the alloy and the oxide; $N_{\mathrm{O}}^{(\mathrm{s})}$ is the oxygen solubility in the B-depleted alloy substrate; D_{O} and D_{B} denote the diffusion coefficient of O and B, respectively.

From the equation, the formation of external oxide scale is a competition between the oxidant permeability $N_{\mathrm{O}}^{(\mathrm{s})} D_{\mathrm{O}}$ and the corresponding alloy quantity $N_{\mathrm{B}}^{\mathrm{O}} D_{\mathrm{B}}$. The equation can be used to discuss the critical content for the transition from internal to external oxidation, not only "exclusive" oxidation.

2.2 Characterization of irradiation effects

2.2.1 Irradiation induced microstructure

One of the simplest optical microscopies is Bright-field (BF) microscopy, however the restrictions of bright-field microscopy include poor contrast for weakly absorbed samples and low resolution. Dark-field (DF) Illumination usually results in a light field or background image. In defect microstructure observation, we usually set two-beam conditions to get both DF and BF images with the combined information.

(1) Two-beam conditions

There is one major difference between forming images to show mass-thickness contrast or diffraction contrast. We can use any scattered electrons to form a DF image showing mass-thickness contrast. However, to get good strong diffraction contrast in both BF and DF images we tilt the specimen to two-beam conditions, in which only one diffracted beam is strong. Of course, the direct beam is the other strong spot in the pattern. the electrons in the strongly excited hkl beam have been diffracted by a specific set of hkl planes and so the area that appears bright in the DF image is the area where

the hkl planes are at the Bragg condition. Hence the DF image contains specific orientation information, not just general scattering information, as is the case for mass-thickness contrast. The specimen can be tilted to set up several different two-beam conditions. **Figure 2.2** includes a zone axis diffraction patten (DP) from a single-crystal specimen in which the beam direction is [011] [35]. The surrounding patterns are a series of two-beam conditions in which the specimen has been tilted slightly so that different hkl spots are strongly excited in each pattern. We can form DF images from each strongly diffracted beam after tilting the specimen, and each will give a different image.

Setting up two-beam conditions is simple. While looking at the DP, tilt around until only one diffracted beam is strong, as in **Fig. 2.2**. However, the other diffracted beams don't disappear because of the relaxation of the Bragg conditions, but they can be made relatively faint. To get the best contrast from defects, your specimen shouldn't be exactly at the Bragg condition (**s**=0, **s** is a measure of how far we deviate from the exact Bragg condition) as in **Fig. 2.3A**. Tilt the specimen close to the Bragg condition but make **s** small and positive (The excess hkl Kikuchi line, just outside the hkl spot). This will give the best possible strong-beam image contrast as in **Fig. 2.3B**. If tilting the specimen slightly, **s** will increases further as shown in **Fig. 2.3C**, the defect images become narrower but the contrast is reduced. Never form strong-beam images with s negative; it's easier to see the defects when s>0.

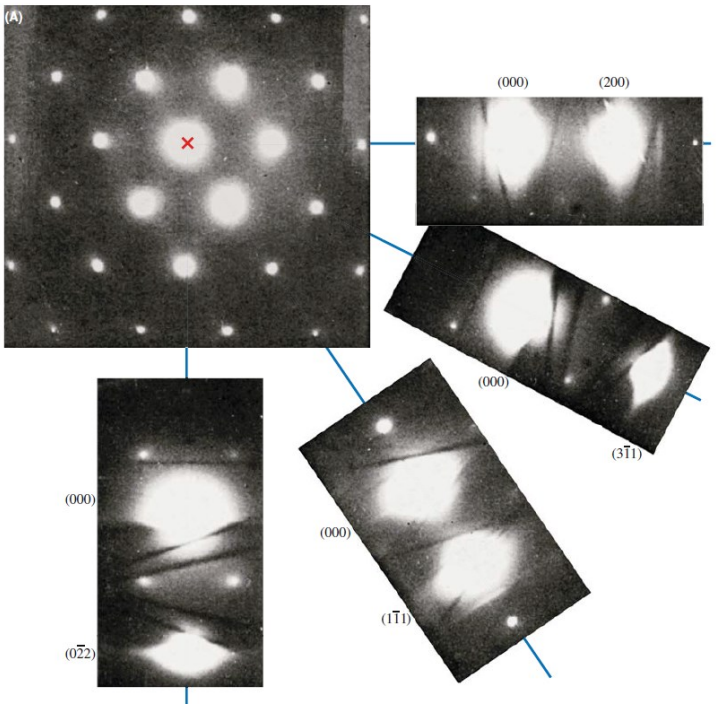

Fig. 2.2 The [011] zone-axis diffraction pattern has many planes diffracting with equal strength. In the smaller patterns, the specimen is tilted so there are only two strong beams, the direct 000 on-axis beam and a different one of the hkl off-axis diffracted beams [35].

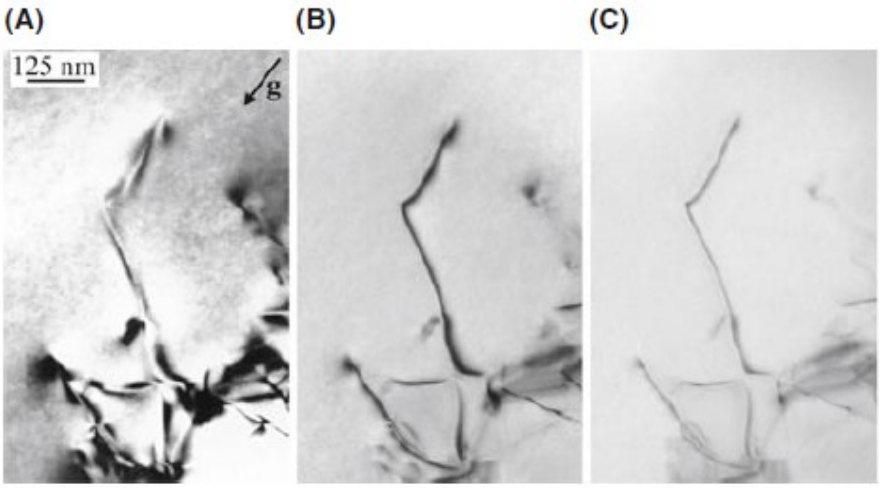

Fig. 2.3 Variation in the diffraction contrast when s is varied from (A) zero to (B) small and positive and (C) larger and positive [35].

(2) Frank loop imaging by relrod technique

The reciprocal lattice is a 3D array of points, each of which we will now associate with a reciprocal-lattice rod (relrod for short), which is centered on the point. The fact that we have rods is the result of the shape of our TEM specimen. When the Ewald-sphere sphere exactly cuts through a point, Bragg's law or the Laue equations are exactly satisfied. When the sphere just misses a point, we define a distance **s** to quantify this excitation error. In other words, **s** is a measure of where we cut the relrod.

A dislocation is a line defect that is characterized by its line direction and its Burgers vector. The crystal around the defect is distorted or strained. However, the distorted volume associated with a single dislocation is so small, it is hard to to see this intensity in the DP unless we have many dislocations in an ordered array (like the second phase or precipitates). It can be demonstrated that this intensity is present by diffracting from an ordered array of dislocations as shown in **Figure 2.4**. The reason we see two extra spots in **Fig. 2.4A** is that we have two arrays of dislocations.

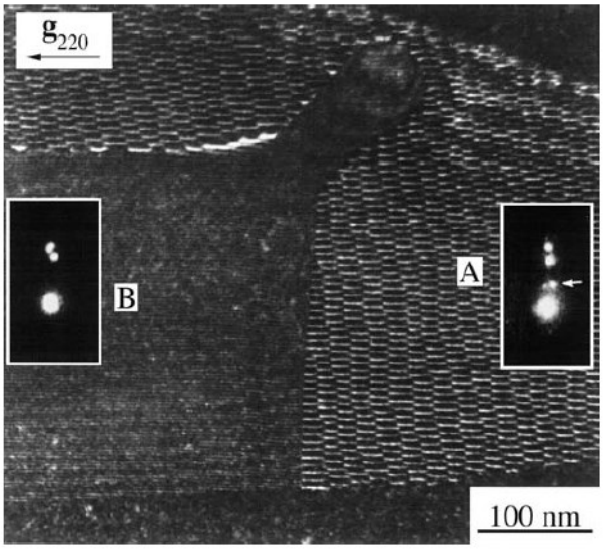

Fig. 2.4 Diffraction from an ordered array of dislocations. Dislocations are present in region A, but not in region B. The insets show a small part of the DP from the two regions. The extra spots present in A are caused by the visible array of dislocations; these spots are a doublet because there is also a second, nearly orthogonal, set of

dislocations present which acts as a separate grating. The other pair is due to the wedge shape and so is common to both DPs [36].

Frank loops are important in irradiated materials because they are often nucleated in a displacement cascade. Since a Frank loop results from addition or removal of close-packed planes, b must be directed normal to the (111) plane and has a length equal to the spacing between planes, $a/\sqrt{3}$; then the Burgers vector is described by b = a/3[111].

Since it is extremely difficult to move on its slip plane (the glide plane is actually a cylinder defined by the edge of the loop), the Frank loop is considered to be sessile or immobile since its glide plane is a cylinder defined by the projection of the loop perimeter in a direction perpendicular to, and above or below the plane of the loop. A Frank loop can also unfault either autocatalytically or by reaction with a dislocation line to form a perfect loop. A Frank loop will always lie on a (111) plane in an FCC lattice.

As mentioned above, Frank loops are faulted dislocation loops lying on the four (1 1 1) planes with a Burgers vector b= a/3(1 1 1), which could clearly present in the irradiated samples. Examples of the diffracting conditions used to image the loops are shown in reference [37] in **Fig. 2.5**. The diffracting conditions are obtained by slightly tilting away from the [0 1 1] zone axis. At this imaging condition two edge-on variants will be visible while the other two are inclined. The relrods (encircled) are due to presence of the (1 1 1) stacking faults in the loops and can be used to image the Frank loops independent of the matrix. Since there are four variants of (1 1 1) stacking faults, each relrod image shows only 1/1 of the total Frank loop existed.

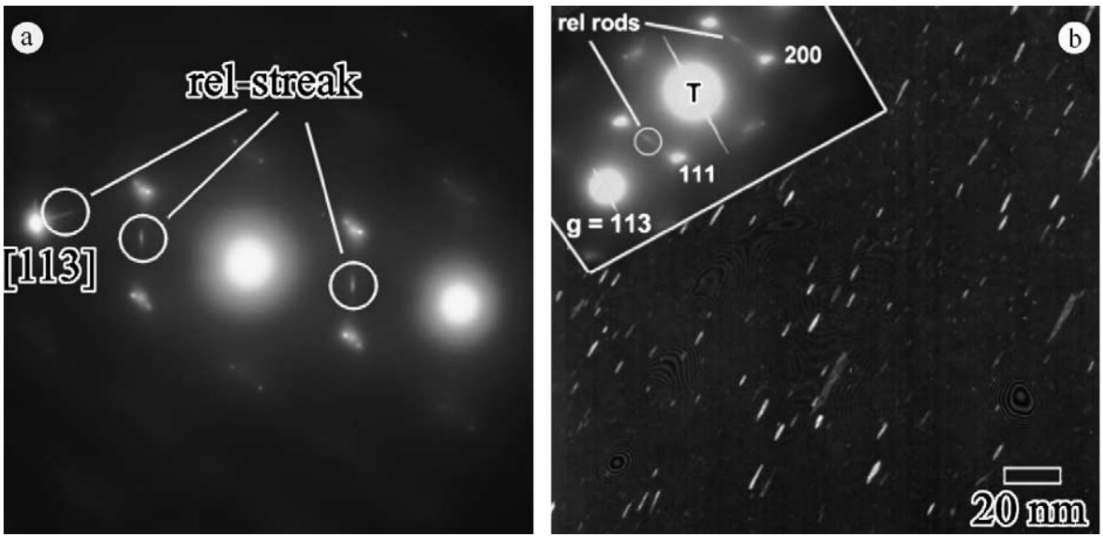

Fig. 2.5 Illustration of the imaging conditions used to image the small Frank loops in all 304 and 316SS heats. The reciprocal lattice streaks (encircled) are shown for (a) 1 dpa and (b) 5.7 dpa. The loop images in (b) show one variant of the loops when imaged using the encircled streak. Newton rings are present in the dark-field image and are simply artifacts of the image scanning [37].

2.2.2 Irradiation induced hardening

Measurement of irradiation hardening

To investigate the mechanical properties of ion-irradiated materials, nanoindentation has been used to measure the hardness of materials in the surface up to a few micron meters since due to the shallow damaged area of irradiation. According to the difference control in indentation depth, there are two typical experimental methods: one is the single depth indentation at a constant depth and the other is continuous stiffness measurement (CSM).

CSM technique was used to continuously obtain the hardness (H)-depth (h) profile with a single indent up to a depth about 2 μm [38]. Yabuuchi et al. [27] measured the depth dependence of Fe–1.4Mn alloy irradiated to 1 dpa at 563 K (shown in **Fig. 2.6**). Therefore, both the irradiated ($H_{\text{irr.}}$) and unirradiated hardness ($H_{\text{unirr.}}$) are defined as the

hardness at an indentation depth of 250 nm in their study. Irradiation hardening ΔH is defined as the difference in the hardness between before and after irradiation; $\Delta H = H_{irr.} - H_{unirr.}$. According to G.M. Pharr. et al. [39], the hardness data up to 0.1 μm should be ignored because of surface preparation may cause the near surface scattering and limitation of the CSM methodology.

(1) Indentation size effect and Nix-Gao model [40]

An indentation size effect (ISE) [39] was observed in **Fig. 2.6**, and the obtained hardness decreased as the indentation depth increased. In an irradiated specimen, the hardness rapidly decreased over an indentation depth of 300 nm, where the strain range exceeds the irradiation damage peak and the obtained hardness reflects the hardness of the unirradiated region.

(2) Softer substrate effect

The softer substrate effect corresponds to the non-irradiated region beyond the irradiation depth range. A film/substrate model would explain the softer substrate effect.

(3) Damage gradient effect

The damage gradient effect is due to the damage profile in the ion-irradiated materials is not considered in the Nix-Gao model. Since the damage displacement value is not constant in the shallow irradiated depth, we need to consider the corresponding damage microstructure which reflects the indentation result at different indentation depth.

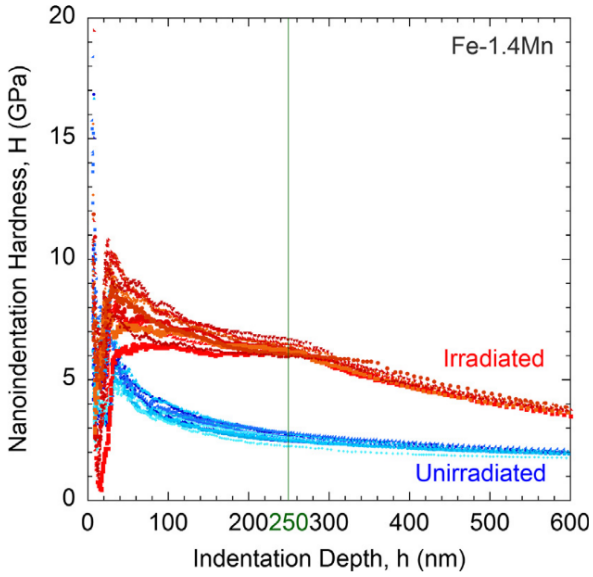

Fig. 2.6 Depth profiles of the hardness of unirradiated and irradiated Fe-1.4Mn alloy [27].

Friction hardening by defect formation

Friction hardening refers to the stress required to sustain plastic deformation. The forces responsible for resisting dislocation motion through a crystal lattice arise from the dislocation network and obstacles such as defect clusters, loops, precipitates, voids. These sources of hardening are characterized as either long range or short range. Long-range stresses are caused by dislocation-dislocation interaction by virtue of their stress fields. Short-range stresses have their origin in the interaction between the moving dislocation and the discrete obstacles in the slip plane. The irradiation induced precipitates, voids, and loops are contributed to short-range stresses.

Short-range forces are due to the interaction between a moving dislocation and an obstacle that lies in its slip plane. Short-range forces arise only when the dislocation contacts the obstacle. Short-range forces can be classified into athermal and thermally activated interactions. An athermal stress interaction is independent of temperature and results in the dislocation bowing around the obstacle. In thermally activated processes,

the dislocation will overcome the obstacle either by cutting through, or climbing over it.

The friction stress due to a dispersion of barriers depends on the average separation between the obstacles in the slip plane of the moving dislocation. **Fig. 2.7** shows a unit area of a slip plane that is intersected by portions of spherical objects of diameter d, which are randomly distributed throughout the solid at a concentration of N cm^{-3}. Any sphere that has its center within the slab of volume d centered on the slip plane intersects the slip plane. The number of obstacles in this volume element is Nd, which is also the number of intersections per unit area on the slip plane. The product of the number of intersections per unit area, Nd, and the square of the distance between obstacles, l^2, is unity, yielding the distance between obstacles:

$$l=(ND)^{-1/2}$$

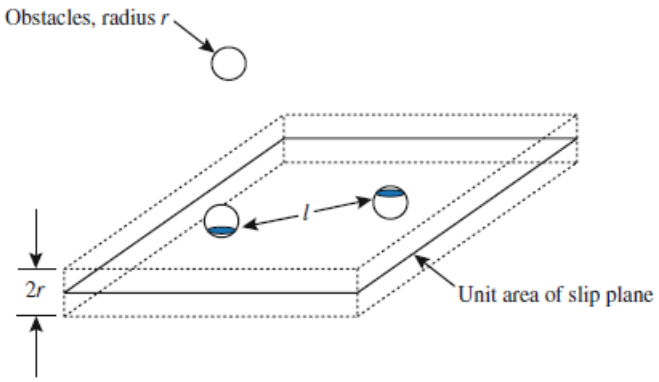

Fig. 2.7 Schematic showing the intersection of spherical obstacles of radius r and spacing l with a unit area of slip plane [41].

When a dislocation encounters an obstacle such as an incoherent precipitate, the short-range interaction occurs when it physically contacts the obstacle. For strong obstacles, an applied stress will cause the dislocation to bow out between the obstacles. Bowing will continue until adjacent segments touch and annihilate each other. This

"pinch-off" process is the same as occurs in a Frank-Read source. Following pinch-off, the dislocation is free to continue along its glide plane until it encounters the next obstacle and the process repeats itself. The obstacles are left with a dislocation loop surrounding them, which presents a stronger obstacle to the next dislocation that comes along (**Fig. 2.8(a)**). The short-range stress due to an array of obstacles of density N and size d is determined as follows. The line tension of an edge dislocation was given as:

$$\Gamma = \frac{\mu b^2}{4\pi} \ln\left(\frac{R}{r_c}\right)$$

where R is equated to the grain radius, r_c is the dislocation core radius and the dislocation core energy is neglected. The shear stress is related to the line tension by $\sigma_s = \Gamma/bR$, and setting $R = l/2$, l is the obstacle spacing $l=(ND)^{-1/2}$:

$$\sigma_s \approx \frac{1}{2\pi} \ln\left(\frac{l}{2r_c}\right) \mu b\sqrt{Nd}$$

while $\alpha \approx \frac{1}{2\pi} \ln\left(\frac{l}{2r_c}\right)$, then $\sigma_s \approx \alpha\mu b\sqrt{Nd}$.

The applied stress at yield, σ_y, is related to the resolved shear stress, σ_s, by the Taylor factor, M such that $\sigma_y = M\sigma_s$, then the equation is generally written as:

$$\Delta\sigma_y \approx M\alpha\mu b\sqrt{Nd}$$

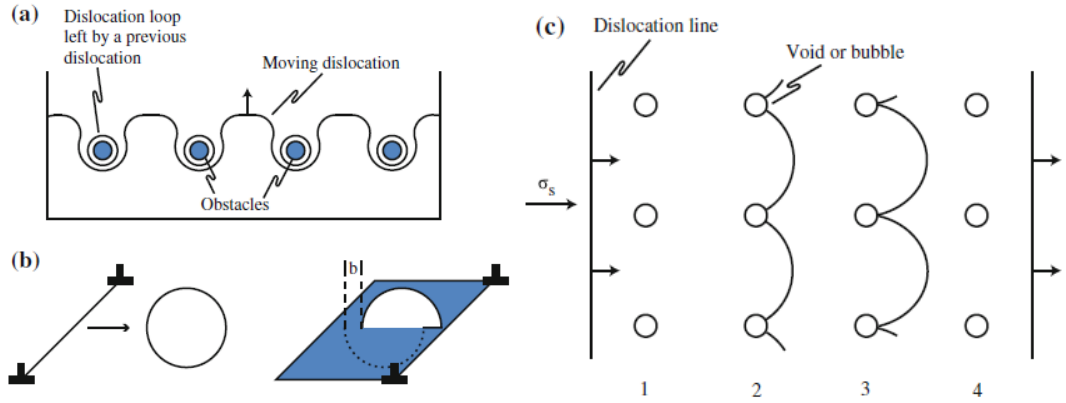

Fig. 2.8 (a) Dislocation bowing around hard obstacles such as precipitates. (b) Dislocation cutting of an obstacle such as a precipitate. (c) Dislocation interaction with voids [41].

Chapter 3 Effect of element addition on oxidation behavior of Co-free Cu-containing CSSAs and HEAs

3.1 Introduction

Supercritical water-cooled reactor (SCWR) is one of the most promising candidates for Generation IV nuclear reactors due to the direct upgrade design of the Generation III water-cooled reactor with comparative plant construction simplicity.1) Combining with the traditional light water reactor (LWR) and the supercritical fossil power plant (FPP), SCWR maintain a core pressure of 25 MPa and an average outlet steam temperature of 500 °C, which offers higher thermal efficiency (~ 45 %) in comparison with the present LWR (~ 33 %) [42, 43]. In SCWR, the use of water as a coolant material is one of the best choices due to its high heat capacity and thermal conductivity. However, the cooling system may suffer from a severe corrosion and irradiation condition at a higher temperature and pressure, which is unbearable by traditional materials. Thus, the research and development of new structure materials with high corrosion and irradiation resistance would be needed for those advanced reactors.

To explore a wide range of available alloys, the concentrated solid solution alloys (CSSAs) and the high entropy alloys (HEAs) have attracted many researchers in the last decade. In contrast from the conventional diluted alloys, the CSSAs and the HEAs contain 5 or more elements in equiatomic or near equiatomic ratios with element concentrations between 5 % and 35 %, which are highly stabilized due to high configurational entropy [6, 8, 9, 11, 44, 45]. It has been reported that some CSSAs and HEAs show good mechanical properties [9, 11], irradiation resistance[9], and corrosion resistance [46, 47] which are very attractive properties as structure materials for nuclear components.

Cantor and Yeh are the pioneers of HEAs, they independently found the

FeCoCrNiMn3) and $Al_xCuCoCrFeNi$ (x= 0 ~ 0.5) [11] alloy with a single face-centered cubic (FCC) structure, respectively. The enhanced ductility and strength of these alloys were further achieved by other researchers [48, 49]. Diffusion coefficient of constituent elements in FeCoCrNiMn alloys was found to be lower than those in conventional FCC alloys, that had been recognized as "sluggish diffusion effect" of HEAs [50]. Although the reduced diffusivity of constituent elements in HEAs is expected to decrease the oxidation resistance since it results in reduced supply of Cr or Al to the alloy surface to establish a protective oxide scale, reduced oxygen diffusion in HEAs [51-53] might be favourable for protective oxide scale formation. Moreover, Cr and Al can be important elements for oxidation resistance since those significantly affects the oxidation behavior of alloy due to a formation of a protective chromia or alumina scale. Comparing with traditional high temperature alloys such as Fe-Cr-Ni stainless steel, HEAs would include a high concentration of Cr (> 20 wt.%), which could suppress detrimental sigma phase formation. Thus, HEAs are considered to be the candidate materials for high-temperature applications, such as heat-exchange part of nuclear power plant.

Several researchers have reported the effect of alloying elements to evaluate the oxidation resistance of HEAs. Chen et al.[54] investigated the oxidation resistance of $Al_xCrFe_{1.5}MnNi_{0.5}$ alloy at 800 °C, and found that the oxidation resistance of HEAs increased with increasing Al content. G.R. Holcomb et al. [55] investigated the oxidation performance of several CoCrFeMnNi based HEAs alloys and found that the CoCrFeNi alloy exhibits comparable oxidation resistance with 304H at 650 °C. On the other hand, CoCrFeMnNi HEAs experienced more rapid oxidation than CoCrFeNi, suggesting that the addition of Mn decreases the oxidation performance. Furthermore, Adomako et al. studied the oxidation behavior of CoCrNi, CoCrNiMn, and

CoCrNiMnFe equimolar alloys. They found that the CoCrNi alloy showed the strongest oxidation resistance in dry air from 800 to 1000 °C. In addition, the oxidation rate was increased by only adding Mn to CoCrNi, but further addition of Fe reduced the oxidation rate of CoCrNiMn[56].

As mentioned above, the research on oxidation resistance of HEAs has been reported, but not sufficiently conducted and most of the studies were performed on Co-containing HEAs in air. Co is not feasible element for the long-term operation in nuclear reactor due to its high radioactivity, thus Co should be replaced to lower activation elements in terms of the material cost [19, 21]. Moreover, the oxidation performance should be evaluated in water vapor since it is closer to the expected operating condition of SCWR compared to dry environment. In fact, the water vapor is known to accelerate the oxidation rate of alloys [57, 58].

In our previous work, Co-free Cu-containing FCC concentrated solid solution alloys were successfully fabricated [59] and indicated comparable mechanical properties comparing with that of structure materials such as 304H and CuCrZr alloy which are applicable to nuclear reactor components [60, 61]. Recent research also found that Cu addition was beneficial to enhance the formation of external Al_2O_3 scale on both the Fe and Ni-based FCC alloys [62]. Therefore, the oxidation performance of Cu-containing CSSAs and HEAs must be properly estimated.

In this study, the Co-free Cu-containing alloys were fabricated, and their oxidation performance were investigated in steam at different temperatures from 500 °C to 700 °C. The element effect and temperature dependence on the oxidation behavior of these Cu-containing alloys would be the key in this study.

3.2 Experimental method

Four kinds of concentrated solid solution alloys: $Cu_{50}Ni_{50}$, $Cu_{33.3}Fe_{33.3}Ni_{33.3}$, $Cr_{30}Cu_{10}Fe_{30}Ni_{30}$ and $Al_{7.5}Cr_{18.5}Cu_{18.5}Fe_{18.5}Ni_{37}$ in atomic percentage (referred to as CuNi, CuFeNi, $CrCu_{0.3}FeNi$ and $Al_{0.4}CrCuFeNi_2$ thereafter, respectively) were fabricated using commercially high purity metals (> 99.9 % purity). CuNi and CuFeNi alloy ingots were prepared by argon (Ar) gas protected arc-melting with pure titanium as the oxygen getter. The ingots were flipped over and melted for more than five times to guarantee the chemical homogeneity of the alloy. $CrCu_{0.3}FeNi$ and $Al_{0.4}CrCuFeNi_2$ alloys were prepared by induction furnace in high-purity Ar atmosphere. Cr and Al were added to expect the formation of a protective oxide scale on the specimen surface. The normal 316 SS (Nilaco Corporation) was also tested as a typical material for coolant system as comparison. The chemical compositions and heat treatment conditions of these alloys are listed in **Table 3.1**. All Cu-containing alloys show simple FCC phase. The details of these alloys can be found in the literature [59].

Table 3.1 Chemical composition of the investigated alloys.

Element (at.%)	Cu	Ni	Fe	Cr	Al	Mn	Mo	Heat treatment
CuNi	48.77	51.23	-	-	-	-	-	1000 ℃, 24h
CuFeNi	32.75	33.02	34.23	-	-	-	-	1050 ℃, 24h
$CrCu_{0.3}FeNi$	9.11	30.35	30.77	29.77	-	-	-	1076 ℃, 72h
$Al_{0.4}CrCuFeNi_2$	18.05	38.07	19.31	18.22	6.35	-	-	1000 ℃, 24h
316 SS	-	9.51	Bal.	17.88	-	0.74	1.14	1050 ℃, 24h

For the steam oxidation test, the rectangular sheet samples (10 × 5 × 1 mm) were cut from the ingots and drilled a hole of 1.5 mm in diameter. All the samples were ground using papers and were sequentially polished by a diamond spray of 1 μm, and

finally rinsed in acetone and ethanol.

The oxidation test was performed in Ar-20 % H_2O. The water vapor was obtained by passing a high purity Ar gas (purity 99.9995 %, O_2 < 0.2 ppm) through a distilled water maintained at 60 °C with a flow rate of 80 ml/min. The oxygen partial pressure at current condition (Ar-20% H_2O, *D*o < 0.2 ppm) can be calculated by FactSage software: $P\,O_2 = 2.1\times10^{-7}$ atm.

The samples were hung on Pt wire and set the surface to be parallel to the gas stream. The furnace was heated in a flowing Ar gas with a heating rate of 10 °C /min. After reaching to the oxidation temperature, the gas stream was switched to Ar - H_2O gas mixture. Oxidation tests were performed over a period of 25 h at 500 °C, 600 °C, and 700 °C. After oxidation, the samples were cooled in a flowing Ar stream with a cooling rate of 10 °C /min. Detailed experimental method can be also found elsewhere [63].

Before the oxidation test, the sample surface area (6 surfaces) was scanned and measured by Image J software. The initial weight of each sample was measured by using a microbalance (Sartorius, Model MC5) with 1 μg resolution. X-ray diffraction (XRD, Rigaku SmartLab, Cu Kα radiation) with a scanning speed of 4 °/min and step of 0.02° was conducted on each sample to characterise the phase structure of the matrix.

After the oxidation test, the oxidation mass gain of samples per unit area was evaluated after different durations of exposure (0, 4, 9, 16, 25 h). The surface morphology and oxidation products structure of the samples were observed by a scanning electron microscope (SEM, JSM-6510LA) and measured by XRD, respectively. The cross-sections of the samples were prepared by a cross section polisher (CP, JEOL SM-09010) using Ar ion beam at 6 kV. The elemental distribution of the oxide scale and matrix was examined by electron probe microanalysis (EPMA,

JEOL JXA-8530F).

3.3 Results and discussion

3.3.1 oxidation kinetics

Fig. 3.1 shows the specific mass changes of the prepared Co-free Cu containing alloys and one commercial alloy (316 SS) exposed in Ar-20 % H_2O atmosphere for 25 h at temperatures ranging from 500 °C to 700 °C. The mass gain of all the alloys increased with increasing the oxidation temperature. It is noted that all the Cu-containing alloys showed lower mass gain compared with 316 SS. Furthermore, Cr- or Al-containing alloy, $CrCu_{0.3}FeNi$ and $Al_{0.4}CrCuFeNi_2$ showed very small increase in mass gain with increasing oxidation temperature. These results could indicate the potential advantage to application for the new generation advanced nuclear plant operating in higher temperature environment.

Fig. 3.2 shows the change of the mass gain of Cu-containing alloys and 316 SS oxidized at 700 °C in Ar-20 % H_2O for 25 h. It is obvious that the oxidation rate of 316 SS was the highest and the oxidation performance of Cu-containing alloys was improved by addition of Al and/or Cr. The $CrCu_{0.3}FeNi$ and $Al_{0.4}CrCuFeNi_2$ exhibited the similar and the lowest oxidation rates among the alloys. Although the oxidation mass gain of CuNi and CuFeNi was much smaller than that of 316 SS, the addition of Fe into CuNi alloy resulted in the increase in the oxidation mass gain. On the other hand, the addition of Cr or Cr and Al to the CuFeNi alloys showed one order magnitude decrease in the oxidation mass gain compared with that of CoCrFeMnNi (about 0.4 mg/cm^2) after 25 h of oxidation at 700 °C in air [64].

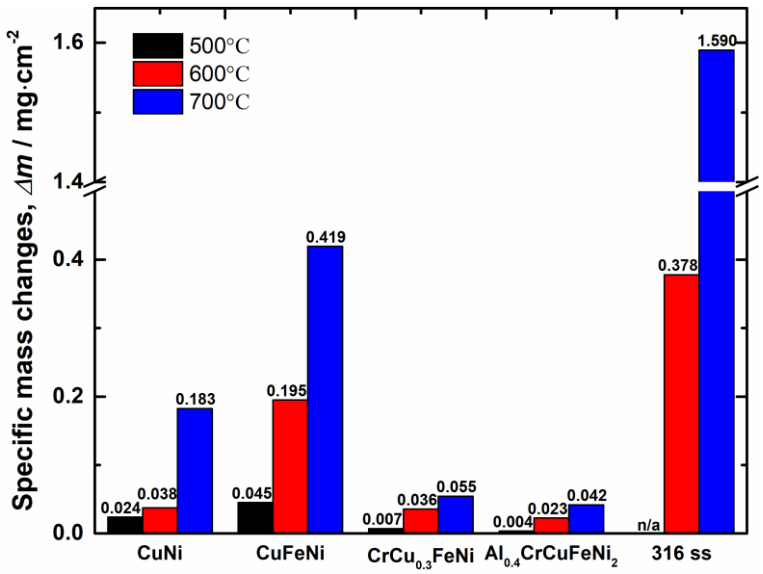

Fig. 3.1 Specific mass changes of CuNi, CuFeNi, $CrCu_{0.3}FeNi$, $Al_{0.4}CrCuFeNi_2$ and 316 SS exposed in Ar-20 % H_2O for 25 h at temperatures ranging from 500 to 700 ℃.

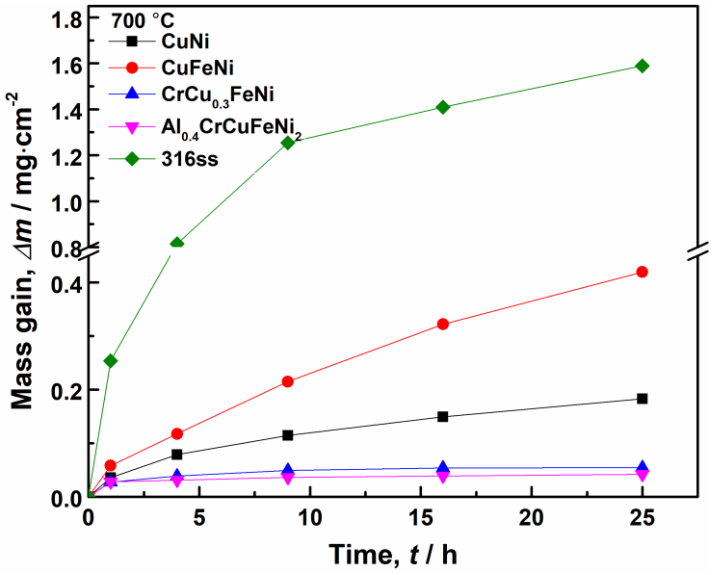

Fig. 3.2 Oxidation kinetics of the Cu-containing alloys and 316 SS at 700 ℃ in Ar-20 % H_2O.

Fig. 3.3 represents the mass gain per unit area (Δm) between 500 and 700 °C as a function of square root of time ($t^{1/2}$). In all oxidized Cu-containing alloys, Δm is increased linearly with $t^{1/2}$, which implies that the oxidation kinetics of these alloys followed parabolic law:

$$\Delta m = (k_p \cdot t)^{1/2} + C \quad (1)$$

where k_p is the parabolic rate constant, t is the corresponding exposure time, C is a constant [65]. The k_p values calculated from **Fig. 3.3** are listed in **Table 3.2**, along with the goodness of the fit (Coefficient of determination, R^2). It seems that there is no apparent effect of Fe on the oxidation kinetics in Cr- and Al-free CuNi alloy at 500 °C, but the values of k_p significantly increased at higher temperature range between 600 and 700 °C. It was also found that the Al-containing HEA showed the minimum value of k_p at all testing temperatures. It seemed that the $CrCu_{0.3}FeNi$ showed similar k_p values to $Al_{0.4}CrCuFeNi_2$ at lower temperatures (500 and 600 °C), while the k_p value at 700 °C was much higher. This indicates that a small Al addition, ~3 wt.%, is beneficial for oxidation resistance at higher temperatures. Those results suggest that Cr and Al would be responsible elements for the reduced oxidation rate of $CrCu_{0.3}FeNi$ and $Al_{0.4}CrCuFeNi_2$. Furthermore, Cr and Al could eliminate the detrimental Fe effect on the oxidation performance.

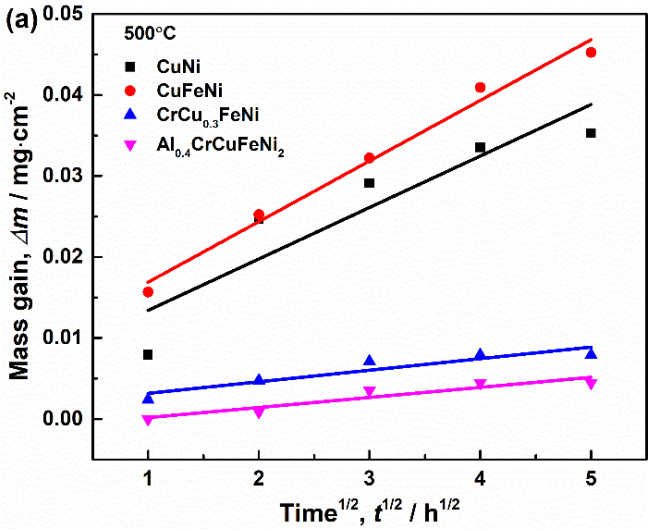

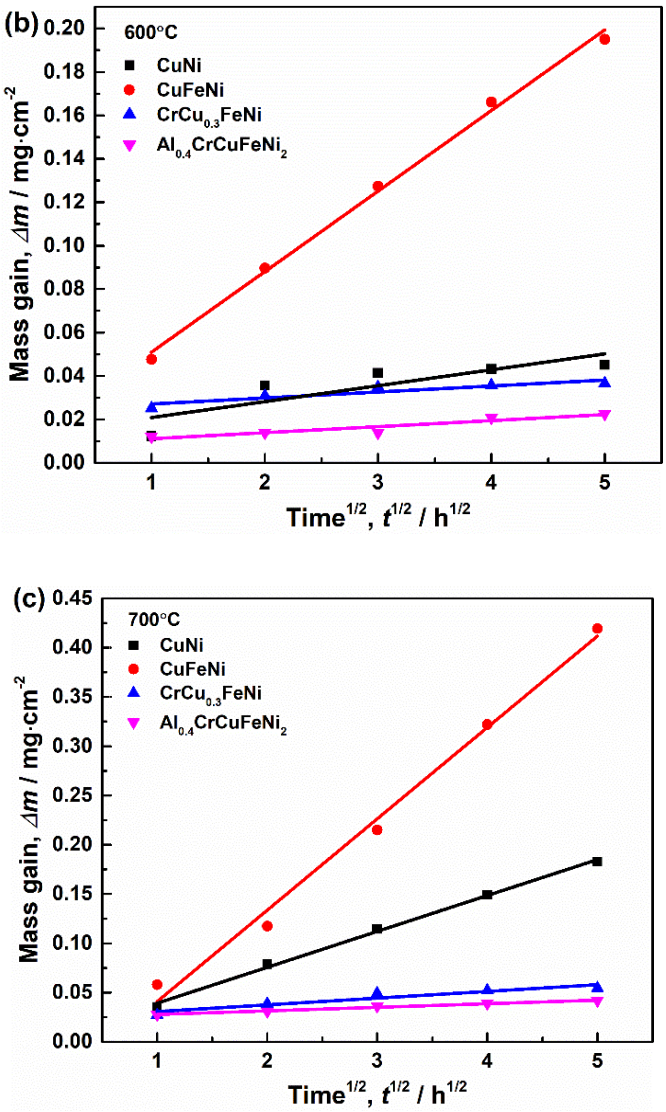

Fig. 3.3 Parabolic curves for oxidation kinetics of Cu-containing alloys at different temperatures for 25 h.

Table 3.2 Parabolic rate constants of the Cu-containing alloys oxidized at 500 - 700 ℃ for 25 h.

Alloys	Parabolic rate constant, $k_p \times 10^{-14}$ / $g^2 \cdot cm^{-4} \cdot s^{-1}$					
	500 ℃	R^2	600 ℃	R^2	700 ℃	R^2
CuNi	1.14	0.839	1.50	0.738	36.88	0.997
CuFeNi	1.56	0.987	38.23	0.996	238.75	0.991
$CrCu_{0.3}FeNi$	0.06	0.871	0.21	0.858	1.28	0.902
$Al_{0.4}CrCuFeNi_2$	0.04	0.891	0.21	0.877	0.37	0.983

3.3.2 Surface morphology and phase structure of oxide scales

Fig. 3.4 shows the surface morphology of the oxide scale formed after oxidation at 500 °C and 600 °C. Large oxide particles of several micrometer in size were uniformly distributed on the relatively smooth surface of CuNi and CuFeNi at all temperatures, whereas $CrCu_{0.3}FeNi$ and $Al_{0.4}CrCuFeNi_2$ formed a very thin oxide scale with tiny oxide particles along the polishing scratches at 500 and 600 °C. At 700 °C, the oxide particles formed on alloys containing Cr, Cr and Al grew larger but those formed on CuFeNi and CuNi alloys became smaller. There was no obvious spallation observed on all the Cu-containing alloys. From these results, it is suggested that HEAs show better oxidation behavior than medium and low entropy alloys especially at higher temperatures, which might be attributed to addition of Cr and Al.

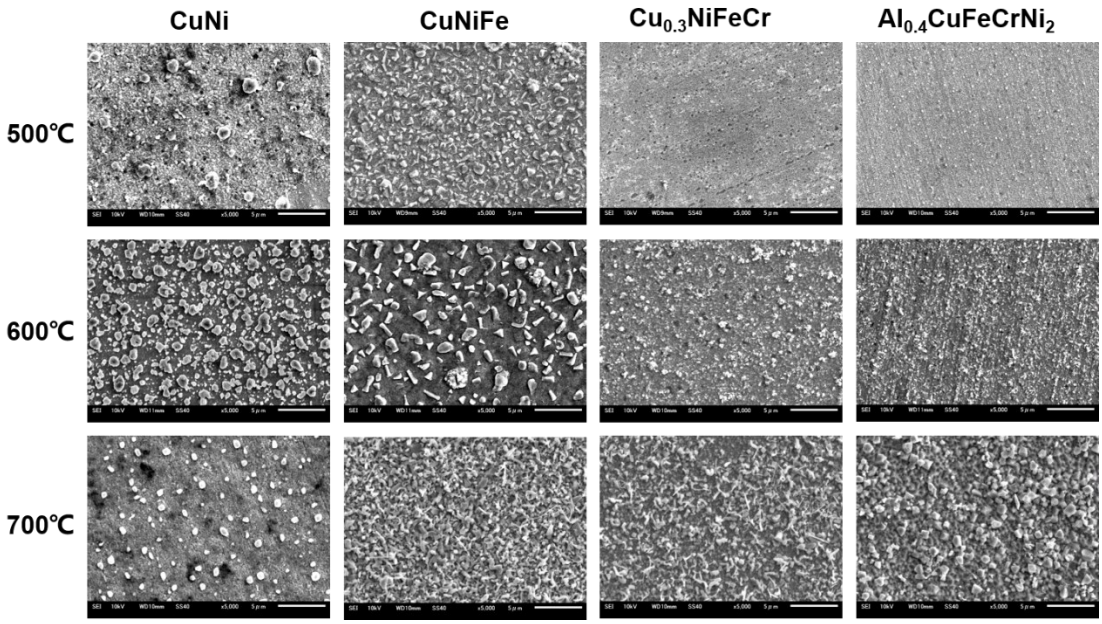

Fig. 3.4 SEM images of surface morphology of oxide scales after oxidation at 500 ℃, 600 ℃ and 700 ℃ for 25 h.

Fig. 3.5 shows the results of XRD analysis in the scale formed after oxidation. At

500 °C, a few oxide phases were detected on the surface of all samples. This is probably due to the formation of the very thin oxide scale, which is not detectable by XRD. A similar result was reported on the oxidized CrMnFeCoNi alloy [64]. On the other hand, NiO phase was detected on the CuNi alloy (Fig. 5a) and the intensities of NiO peaks were increased with increasing the oxidation temperature. This indicates the formation of a thicker oxide scale at higher temperatures. The oxide scale formed on the CuFeNi was composed with NiO, Fe_3O_4, and small amount of CuO (**Fig. 3.5b**). The peaks of Cr_2O_3 were also recognized on the surface of $CrCu_{0.3}FeNi$ oxidized at 700 °C (**Fig. 3.5c**). The presence of Cr_2O_3 and Al_2O_3 was recognized on the $Al_{0.4}CrCuFeNi_2$ oxidized at 700 °C. However, at lower temperatures (500 ~ 600 °C), the signals from Cr or Al-rich oxides are too weak to identify probably due to less amount of the oxide scale as mentioned above. The current results indicate that Cr and Al-containing HEAs would have oxidation resistance especially at lower temperatures.

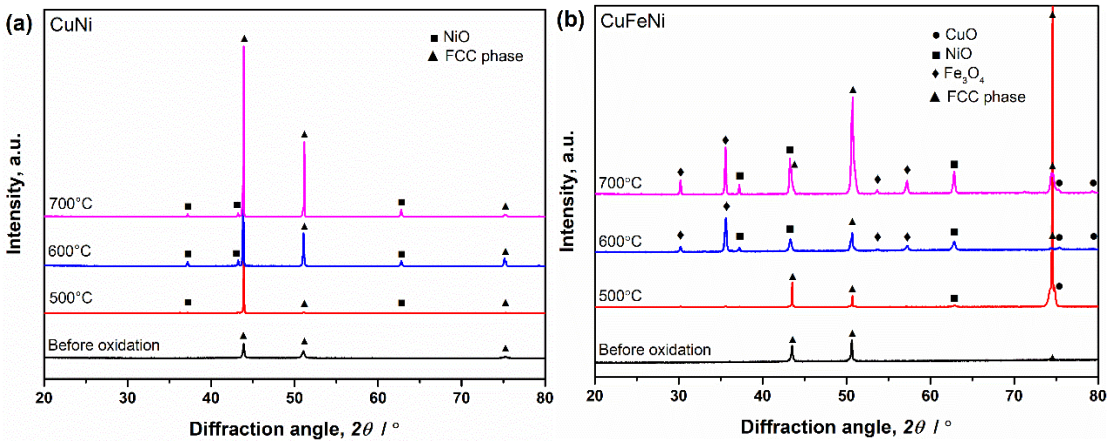

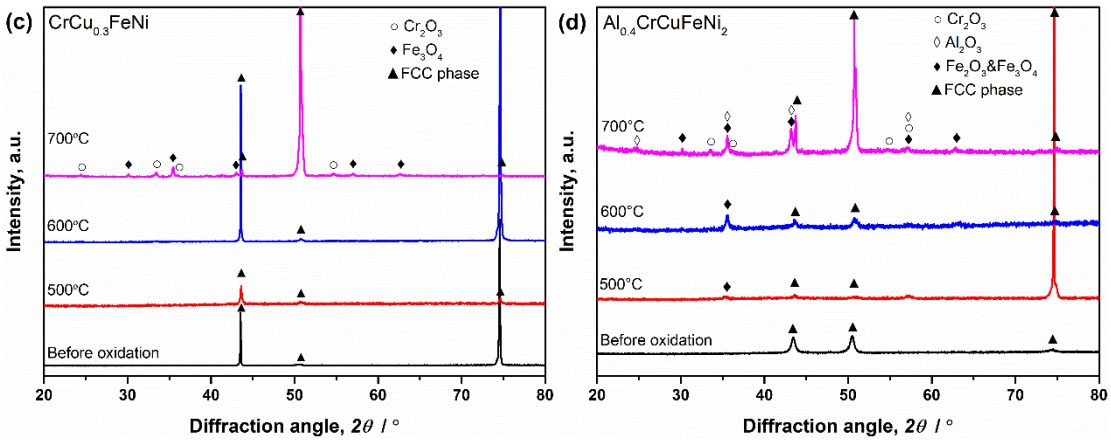

Fig. 3.5 XRD results of the alloys before and after oxidation at 500 ~ 700 °C for 25 h: (a) CuNi; (b) CuFeNi; (c) $CrCu_{0.3}FeNi$; (d) $Al_{0.4}CrCuFeNi_2$.

3.3.3 Cross-sectional microstructure of oxide scales

The cross-sectional microstructure of the oxide scales formed on the alloys at different temperatures after 25 h of oxidation is shown in **Fig. 3.6**. The oxide scales formed at 500 °C was too thin to observe by SEM, however, some thicker nodules formed on CuFeNi. The oxidized CuFeNi showed the formation of the thickest scale of 1.5 μm and 3 μm at 600 °C and 700 °C, respectively. However, $CrCu_{0.3}FeNi$ and $Al_{0.4}CrCuFeNi_2$ showed much thinner oxide scales to be about 0.3 μm and 1 μm at 600 and 700 °C, respectively. These experimental results support the less oxidation mass gain and the smaller k_p values in HEAs.

Figs. 3.7 ~ 3.10 show the element mapping by EPMA and the corresponding backscattered electron micrograph of the oxide scale formed at 700 °C for 25 h. The element distributions after oxidation at 600 °C appears similar to that at 700 °C. The scale formed on the oxidized CuNi was NiO. The enrichment of Cu was observed in the subsurface region due to the selective oxidation of Ni. The scales formed on the oxidized CuFeNi were the duplex layers with an outer Fe-rich oxide and an inner Ni-

rich oxide. The Cu-rich layer was also formed in the subsurface of CuFeNi. It is noted that the needle-shaped and the round-shaped internal Fe-rich oxide precipitates were observed in and around the Cu-rich layer. Furthermore, some pores were found in the oxide scale formed on the CuFeNi. It was reported that the pores could be produced through the counter vacancy injection due to fast outward diffusion of Fe in the oxide scale [66, 67].

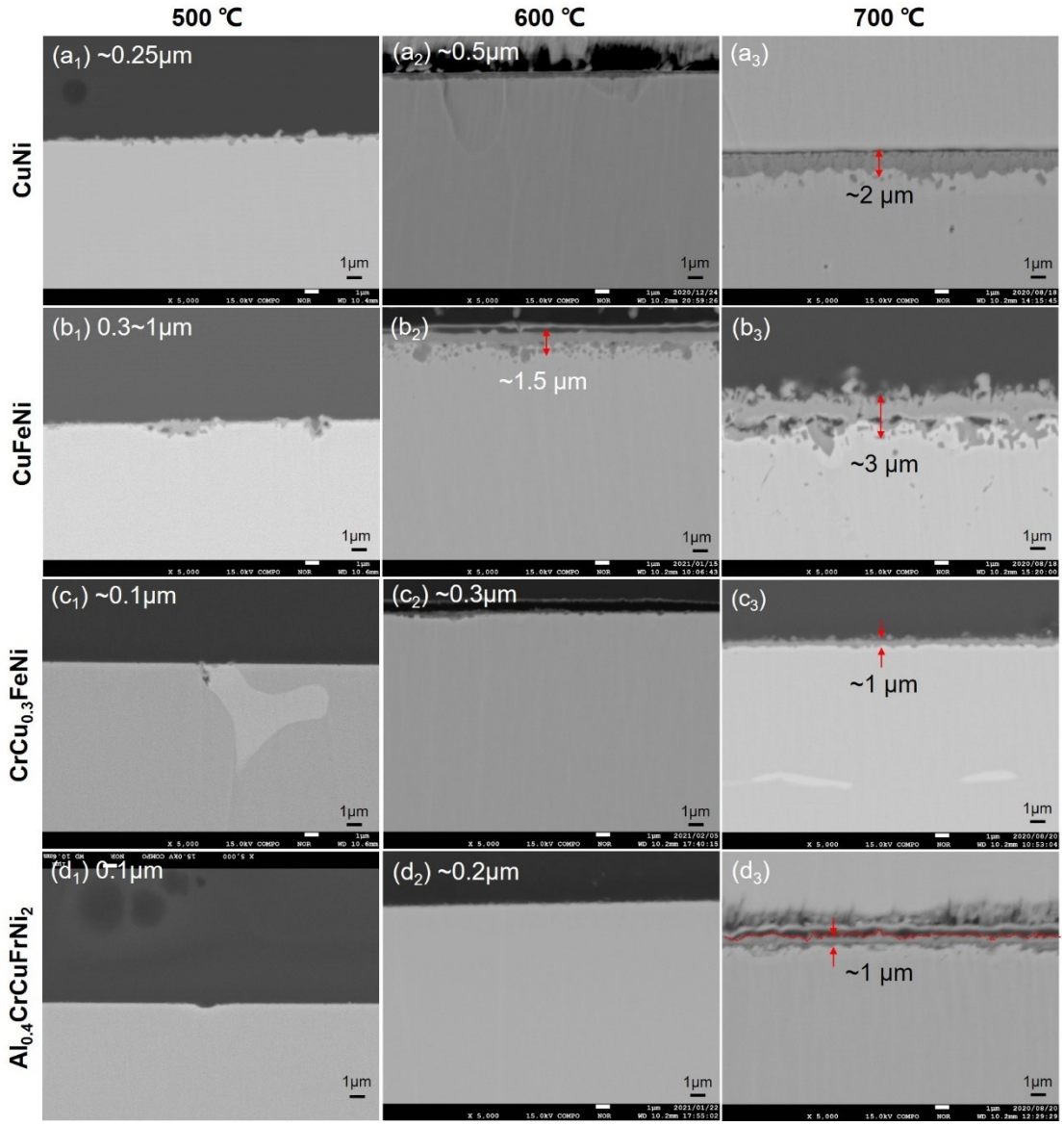

Fig. 3.6 Cross-sections of the oxide scale formed on the alloys after 25 h at 500, 600, and 700 ℃: (a_1-a_3) CuNi, (b_1-b_3) CuFeNi, (c_1-c_3) $CrCu_{0.3}FeNi$, (d_1-d_3) $Al_{0.4}CrCuFeNi_2$.

The oxide scale on $CrCu_{0.3}FeNi$ also consisted of the outer Fe-rich layer and the inner Cr-rich layer. Cu enrichment occurred below the Cr_2O_3 layer as shown in **Fig. 3.9**. Even though the alloy contains 27 wt.% of Cr, the oxidation experiment resulted in the Fe oxide formation in the transient stage of oxidation. This is probably due to the presence of water vapor. The similar oxidation behavior was reported in Ni-based Fe-containing alloys such as Inconel 718 [68]. In the transient stage of oxidation, Fe oxide might form initially, then a stable Cr_2O_3 layer subsequently developed below the Fe-oxide. The Cr_2O_3 layer performed as a protective oxide scale, preventing further oxidation of alloying elements such as Fe in the following steady state oxidation period. The effect of Cu on the oxidation behavior, in particular the formation of Cr_2O_3 scale was not apparently confirmed.

The oxide scale formed on $Al_{0.4}CrCuFeNi_2$ consisted of the outer most Fe-rich layer, the inter mediate Cr-rich layer, and the inner Al-rich layer as shown in **Fig. 3.10**. The formation of Fe-, Cr- and Al-rich oxide layers would result in the depletion of those elements in the subsurface region of the matrix, correspondingly, other elements Ni and Cu were enriched in same region. Probably, Fe-rich oxide also formed on $Al_{0.4}CrCuFeNi_2$ in the transient stage of oxidation. The formation of the stable Cr_2O_3 scale below the Fe-rich oxide scale could lead to the formation the Al_2O_3 scale with low Al content, ~3 wt.% in the alloy. As mentioned in the introduction, one of the important effects reported in HEAs is sluggish diffusion. Unfortunately, the diffusivity of Al and Cr in the alloys is unknown in the present study, however, apparently 3 wt.% Al would be insufficient to form the continuous Al_2O_3 layer on the conventional FCC Ni and Fe based alloys. It was reported that Cu could reduce the critical Al content in FCC matrix alloys [62]. Therefore, the excellent oxidation performance by formation of an external protective Al_2O_3 scale on HEAs might be attributed to higher Cu content in the alloy.

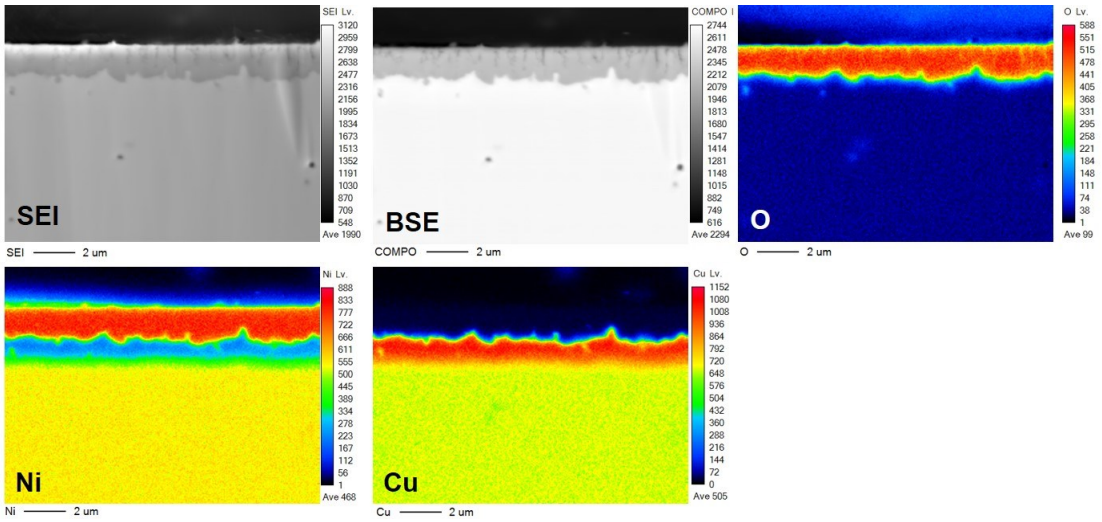

Fig. 3.7 Cross sectional backscattered electron micrograph and corresponding elemental maps of the CuNi alloy after steam oxidation at 700 ℃ for 25 h.

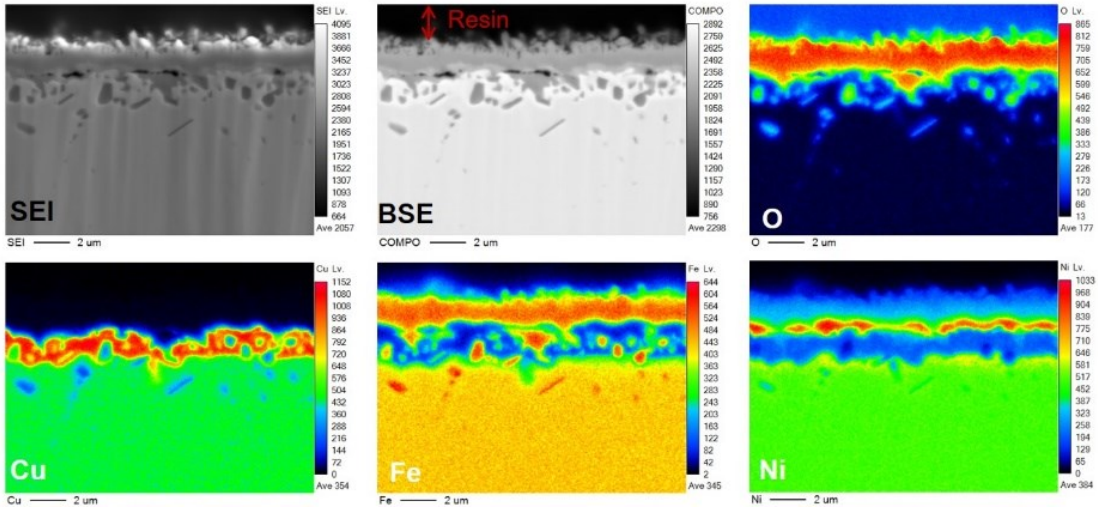

Fig. 3.8 Cross sectional backscattered electron micrograph and corresponding elemental maps of the CuFeNi alloy after steam oxidation at 700 ℃ for 25 h.

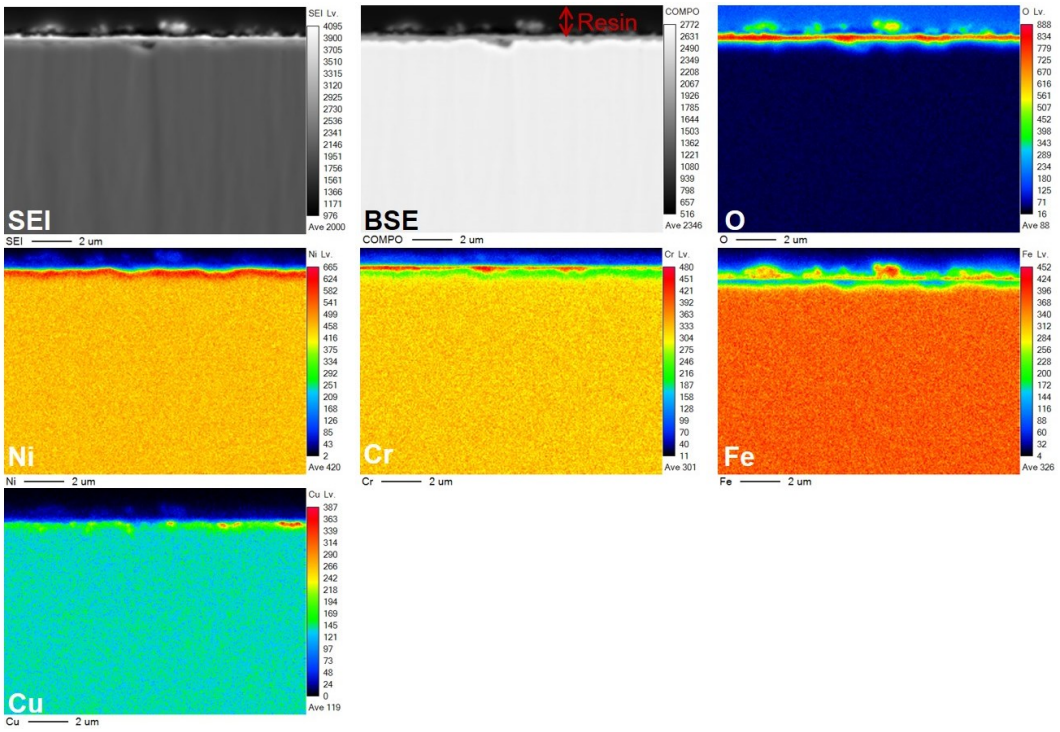

Fig. 3.9 Cross sectional backscattered electron micrograph and corresponding elemental maps of the $CrCu_{0.3}FeNi$ alloy after steam oxidation at 700 ℃ for 25 h.

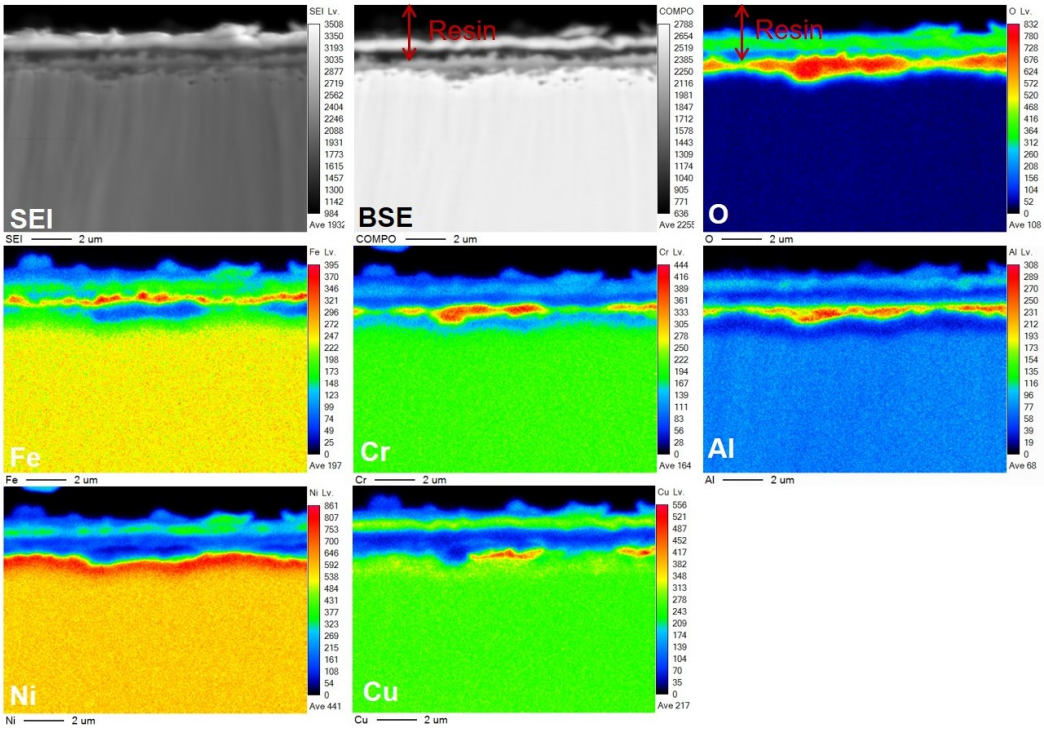

Fig. 3.10 Cross sectional backscattered electron micrograph and corresponding elemental maps of the $Al_{0.4}CrCuFeNi_2$ alloy after steam oxidation at 700 ℃ for 25 h.

3.4 Summary

Four kinds of Co-free Cu-containing CSSAs with FCC structure were oxidized in the atmospheres containing water vapor at 500, 600, and 700 ℃ for 25 h in order to evaluate the oxidation performance. Oxidation performance of the CSSAs was much better than that of the commercial 316 SS in this experimental condition. The decrease in the mass gain of Cu-containing alloys was in the order from CuNi, CuFeNi, $CrCu_{0.3}FeNi$, and $Al_{0.4}CrCuFeNi_2$. The addition of Fe significantly decreased the oxidation resistance of CuNi alloy even it contains high Ni. The element of Cr and Al is contributing to the protective scale formation, and the parabolic rate constant shows a significant decrease at high temperatures. $Al_{0.4}CrCuFeNi_2$ showed the best oxidation resistance in this study probably due to the formation of protective Al_2O_3 scale.

Chapter 4 Effect of Al content on oxidation behavior of Co-free $Al_xCrCuFeNi_2$ HEAs

4.1 Introduction

The research and development of advanced nuclear power systems are critically important for achieving the goals of carbon neutrality by 2050. Supercritical water-cooled reactor (SCWR) is one of Generation IV reactors, which offers higher thermal efficiency (~ 45 %) and enhanced safety comparing with the light water reactor (LWR) [42]. However, currently available austenitic stainless steels could not provide sufficient oxidation and irradiation resistance for the higher outlet temperature (> 500 °C) and irradiation dose in advanced reactors for extended operation [2, 69]. Differing from conventional alloys with one or two main components, high entropy alloys (HEAs) normally contain five or more principal elements with relatively high concentrations (5-35 at%), presenting the formation of stabilized simple solid-solution structure by the high configurational entropy [6, 8, 9, 11]. Moreover, compared with traditional alloys, the higher activation energy for oxygen diffusion and higher vacancy mobilities in HEAs show potential for a better oxidation and radiation resistance [29, 51, 52, 70, 71].

FCC-based HEAs aroused constant attention in nuclear application due to the outstanding ductility and fracture toughness property [12-14, 72-74]. While, higher operation temperature of advanced reactors requires more excellent properties. Several methods have been employed to improve the strength of HEAs, such as plastic deformation, grain refinement, and precipitate former addition [15, 16, 49, 75, 76]. Recently, the precipitation strengthening by formation of ordered $L1_2$ nanoprecipitates in the FCC matrix was considered to be an effective way for achieving strength-ductility synergy, which is similar as γ/γ′ strengthening in Ni-base superalloys at elevated temperature [15-17, 77-79]. However, the most well studied HEAs contains the element

of Co, which shows high radioactivity during extensive lifetime of operation in nuclear reactors. Guo et al. investigated the phase stability and mechanical properties of $Al_xCrCuFeNi_2$ HEAs by fully replacing the radioactive Co element with Ni in the $Al_xCoCrCuFeNi$ HEAs, which shows simple FCC structure at a low Al content (x < 0.7) [18, 19]. Further characterizations on this HEA system confirmed the precipitation of the nanoscale $L1_2$ and Cu-rich precipitates under different homogenization and annealing process and found that the $L1_2$ nanoprecipitates were stable at a wide temperature range, indicating the potential of enhanced mechanical properties at higher temperatures [19-22].

The oxidation behavior of HEAs is another important aspect need to be considered for real application. Basically, the ideal alloys designed for high temperatures are protected by the rapid formation of dense oxide scale with slow growing rates, which provides a barrier between the substrate and the atmosphere to prevent further oxidation [80]. Due to the lower Gibbs free energies of oxides and high temperature stability, the addition of Cr and/or Al elements are frequently applied to the alloys for the protective Cr_2O_3 and/or Al_2O_3 scale formation. By contrast, the critical Cr or Al content for their oxide scale formation is quite high in conventional alloys [81, 82], and the high alloying of Al could be restricted by the formation of detrimental phases in one-principal element alloys. HEAs are more feasible for developing a high alloying composition alloy with simple structures. The study on $CoCrFeNiAl_x$ (x = 0.15, 0.4) HEA system reported that $CoCrFeNiAl_x$ HEAs exhibited better oxidation resistance than HR3C steel in supercritical water at 550 and 600 °C, and the properties of HEA are greatly affected by Al addition [23]. Mohanty et al. investigated the high temperature oxidation performance of $Al_xCoCrFeNi$ (x = 0.3, 0.7) HEAs, they found the oxidation resistance was enhanced by increasing Al content and the thickness and continuity of oxide scales

are different from Al concentrations [24]. Similarly, the short-term oxidation study of $Ni_2FeCoCrAl_x$ (x = 0, 0.5, 1.0) HEAs at 900 °C by W. Kai et al. showed that Al-free HEA formed multiple scales with preferentially oxidized Cr_2O_3, while Al-containing HEAs experienced to form an exclusive alumina scale with decreasing oxidation rates [25]. However, most of the above-mentioned study showed the substrate with different phases by changing the Al content, which significantly affect the oxidation behavior. To get a better understanding of the effect of Al, as well as finding the critical Al content for protective scale formation, a design of alloy composition with similar microstructure would be needed.

To date, the oxidation study on the HEAs has not been extensively investigated, especially for the Co-free FCC-typed HEAs. Our previous study on the mechanical property and oxidation behavior of Co-free Cu containing HEAs showed that the $Al_{0.4}CrCuFeNi_2$ HEAs exhibited comparable hardness and much lower oxidation rate than stainless steel at 700 °C in steam, indicating the potential for advanced nuclear application at higher temperatures [59, 83]. In a most recent work by Huang et al., the oxidation resistance of $Al_{0.3}CrCuFeNi_2$ HEAs after different aging treatment were evaluated, and the formation of multiple oxide scales including protective Cr_2O_3 and Al_2O_3 scales were identified [84]. Nevertheless, there is still limited work focus on the effect of Al on the oxidation performance of Co-free HEAs. In this study, we selected the Al concentration of $Al_xCrCuFeNi_2$ HEAs from 0.2 to 0.6 to obtain simple FCC phase, and investigate the steam oxidation behavior of these HEAs at 700 °C. The cross-sectional oxide scale morphology and detailed microstructures were characterized to understand the effect of Al content on the oxidation kinetics and scale formation process.

4.2 Experimental

Three kinds of Co-free $Al_xCrCuFeNi_2$ HEAs with different Al concertation, namely the Al0.2 ($Al_{0.2}CrCuFeNi_2$), Al0.4 ($Al_{0.4}CrCuFeNi_2$), Al0.6 ($Al_{0.6}CrCuFeNi_2$) were prepared using commercially high purity metals (> 99.9 % purity) and arc-melted in Ar atmosphere with pure titanium as the oxygen getter. The ingots were re-melted for more than five times to guarantee the chemical homogeneity and solution annealed in evacuated quartz tubes at different temperatures to form simple FCC structure. The compositions and solution annealing conditions of the HEAs are given in **Table 4.1**. Specimens for oxidation test were cut into rectangular coupons (10 × 5 × 1 mm) from the annealed ingots and drilled a hole of 1.5 mm in diameter. All surfaces of the samples were sequentially ground to 2000 grit SiC paper, polished by 1 μm diamond spray, and finally cleaned ultrasonically in acetone and ethanol.

Table 4.1 Chemical composition of the $Al_xCrCuFeNi_2$ alloys.

Element (at%)	Al	Cr	Cu	Fe	Ni	Heat treatment
$Al_{0.2}CrCuFeNi_2$	3.92	19.12	18.87	19.58	38.51	1000 °C, 24h
$Al_{0.4}CrCuFeNi_2$	7.57	18.55	17.88	18.95	37.05	1000 °C, 24h
$Al_{0.6}CrCuFeNi_2$	10.52	17.98	17.58	18.21	35.71	1000 °C, 24h 1050 °C, 24h

Oxidation experiments were conducted at 700 °C in a steam oxidation equipment by flowing Ar-20 % H_2O gas mixture (Ar purity > 99.9995%) to the samples with low oxygen partial pressure ($P\,O_2 = 2.1\times10^{-7}$ atm). The samples were hung on Pt wire in an alumina boat in the hot zone of a horizontal tube furnace. The heating and cooling rates of the furnace kept 10 °C/min in all experiment. After different durations of exposure (0, 4, 9, 16, 25, 49, 100 h), the mass gains of each sample were measured by using a

microbalance (Sartorius, Model MC5) with 1 μg resolution. Detailed experimental method can be also found in literature [83].

Phase constitutions of the specimens were characterized by X-ray diffraction (XRD, Rigaku SmartLab) using Cu Kα radiation and the surface morphologies were examined by scanning electron microscope (SEM, JSM-6510LA). The cross-sections of the oxidized samples were prepared by a cryo-cross section polisher (CCP, JEOL IB-19520) using Ar ion beam at 6 kV and the oxide scales and matrix were analyzed by electron probe microanalysis (EPMA, JEOL JXA-8530F). Further characterization on the microstructure and chemical composition of the specimens were conducted by transmission electron microscopy (TEM, JEOL JEM-2010), SEM (30 kV high resolution SEM with EDS detector, Hitachi Regulus SU-8230) and scanning transmission electron microscopy (STEM, Hitachi HD-2000). The TEM/STEM samples were picked up by focused ion beam system (FIB, Hitachi FB-2100; JEOL JIB-4601F) and milled with a thickness of about 100 nm.

4.3 Results

4.3.1 Substrate analysis

The XRD pattens of the as cast and solution annealed $Al_xCrCuFeNi_2$ (x = 0.2, 0.4, 0.6) HEAs are given in **Fig. 4.1**. Only FCC-typed solid solutions were detected in as cast HEAs in **Fig. 4.1a**, with weak intensities of ordered FCC ($L1_2$) phase co-existed in Al0.4 and Al0.6 HEAs. The current alloy composition has been reported to have Cu segregation at inter dendritic regions which has close lattice constant with the main FCC phase in the as cast condition[19, 76], hence the solutionization was done to get a more homogenous structure. After solution annealing at 1000 °C for 24 h, the Al0.2 and

Al0.4 HEAs remained FCC phases as shown in **Fig. 4.1b**, however, Al0.6 HEA formed BCC phase. Those peaks of BCC phase disappeared by increasing annealing temperature to 1050 °C. Similarly, it was reported that BCC phases were observed in 900 °C annealed $Al_{0.5}CrCuFeNi_2$ HEA and they disappeared after 1100 °C annealing [18-20, 22]. The possibility of BCC phase formation in $Al_xCrCuFeNi_2$ HEA can be explained by the Phase diagram calculation. **Fig. 4.S1** shows the calculation results of phase fractions versus temperature by Pandat software. It is suggested that BCC phase could be formed in Al0.6 HEA at temperature below 975 °C. To keep the alloys for oxidation test simple FCC phase, we select the solution annealing temperature of 1000 °C for Al0.2 and Al0.4 HEAs and 1050 °C for Al0.6 HEAs, respectively.

To further confirm the existence of ordered FCC phase and its microstructure, TEM observation was conducted on the solution annealed alloys. **Fig. 4.2a** shows the selected area diffraction pattens (SADP) from near [011] zone axes (ZA) of Al0.6 HEA. The superlattice reflections in SADP pattens confirms the presence of $L1_2$ ordering. Dark field TEM image obtained from the superlattice spot (100) shown in **Fig. 4.2b** indicated a homogenous distribution of fine γ′ precipitation in FCC matrix. The average precipitate diameter was measured to be 10.4 nm by ImageJ software.

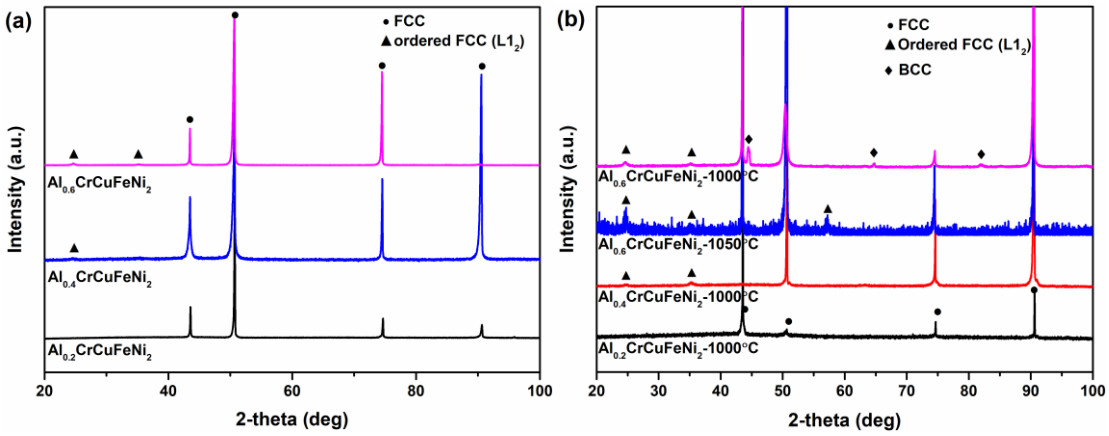

Fig. 4.1 XRD profiles of (a) as-cast and (b) solution annealed $Al_xCuFeCrNi_2$ HEAs at different temperatures.

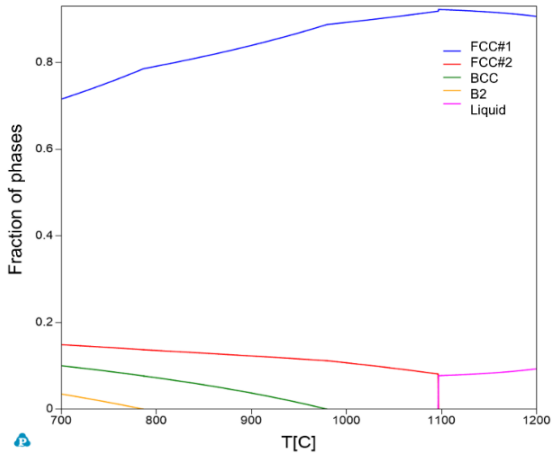

Fig. 4.S1 Calculated diagram of phase fractions versus temperature in $Al_{0.6}CrCuFeNi_2$ HEA by Pandat software.

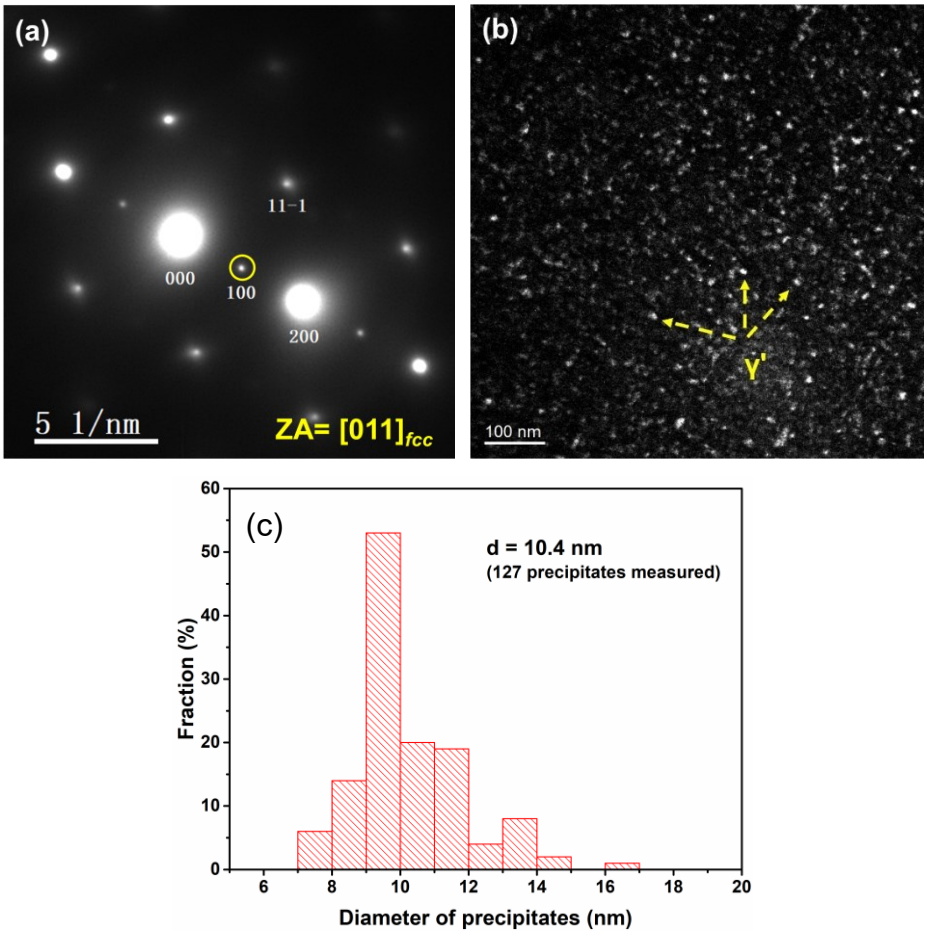

Fig. 4.2 TEM images of Al0.6 HEA after solute annealing: (a) selected area diffraction pattens (SADP) close to [011] zone axes (ZA) showing the super-lattice spot at (100) position marked in circle. (b) weak-beam dark field (DF) TEM image obtained from

the marked super lattice spot in (a) showing the fine distribution of $L1_2$ (γ′) precipitates. (c) Fraction distribution of $L1_2$ precipitates in Fig. 2 (b).

The scanning transmission electron microscopy (STEM) images and corresponding elemental mappings of solution annealed $Al_{0.6}CrCuFeNi_2$ HEA in **Fig. 4.3** show homogenous composition distribution of each alloyed element. Some researchers reported the composition fluctuation of Cu in 10-20 nm scale in $Al_{0.3}CuFeCrNi_2$ HEA by atom probe tomography observation [30], which may probably be found in current study. However, deeper analysis on nano-scale microstructure goes too far from the point of this study. The above-provided substrate information of HEAs is sufficient for comparison with the alloys after oxidation.

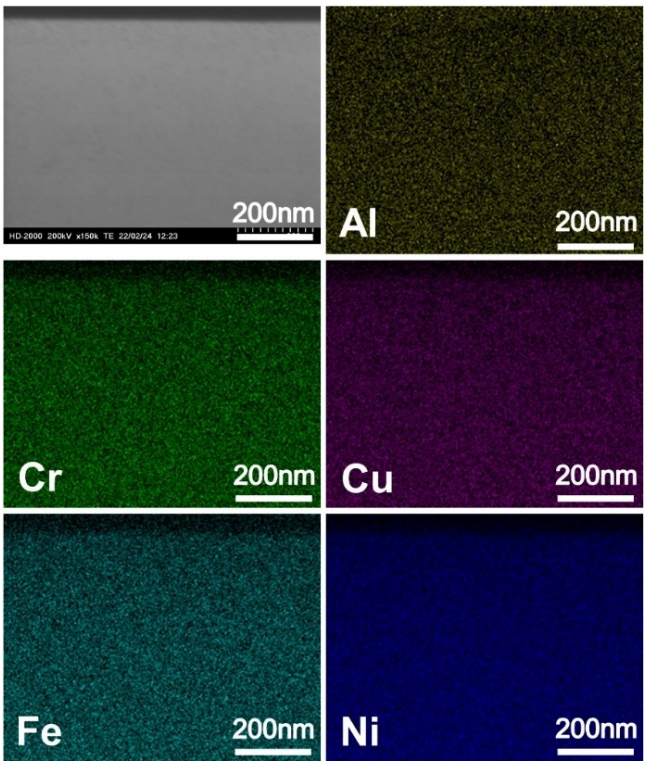

Fig. 4.3 Scanning transmission electron microscopy (STEM) image and corresponding elemental mappings of solution annealed $Al_{0.6}CrCuFeNi_2$ HEA.

4.3.2 Oxidation kinetics

Fig. 4.4a shows the mass gains of all HEAs oxidized at 700 °C in Ar-20% H_2O for 100 h. All alloys show a low total mass gain value less than 0.2 mg/cm^2, which is lower than that of 316 SS and Cantor alloys, suggesting the advantages of the current set of $Al_xCrCuFeNi_2$ HEAs for nuclear application at elevated temperature [64, 83]. Compared to low-Al containing (Al0.2) HEA, the mass gains of Al0.4 alloy decreased by half and Al0.6 shows the lowest mass gain value within 100 h, indicating an improved oxidation resistance by increasing the Al concentration of the alloys.

The mass gain per unit area (Δm) as a function of square root of time ($t^{1/2}$) were plotted in **Fig. 4.4b**. The oxidation kinetics of all alloys followed a parabolic law:

$$\Delta m = (k_p \cdot t)^{1/2} + C \qquad (1)$$

where k_p is the parabolic rate constant, t is the corresponding exposure time, C is a constant [65]. The parabolic behavior of Al0.2 HEA showed a two-stage oxidation kinetics with a marked change of k_p after 25 h, while Al0.4 and Al0.6 HEAs can be fitted by single parabolic rate constants due to the non-obvious change of k_p based on the cyclic oxidation measurement. The k_p values of each alloy were calculated and listed in **Table 4.2**, along with the fitness (Coefficient of determination, R^2) of the curves.

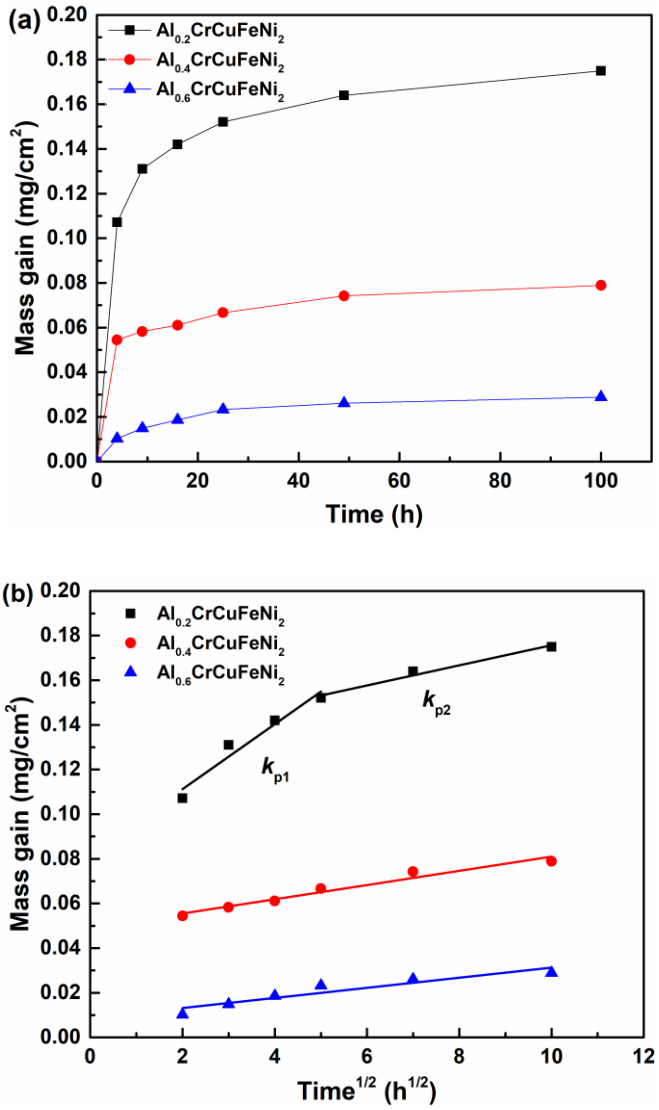

Fig. 4.4 (a) Mass gains and (b) parabolic plots of mass gain versus square root of time of $Al_xCrCuFeNi_2$ HEAs oxidized at 700 °C in Ar-20 % H_2O.

Table 4.2 Parabolic rate constants of the HEAs oxidized at 700 °C for 100 h.

Alloys	Parabolic rate constant, $k_p \times 10^{-14}$ / $g^2 \cdot cm^{-4} \cdot s^{-1}$	R^2
$Al_{0.2}CrCuFeNi_2$	(1) 5.89	0.95
	(2) 0.57	0.98
$Al_{0.4}CrCuFeNi_2$	0.28	0.98
$Al_{0.6}CrCuFeNi_2$	0.14	0.88

It is apparent that Al0.2 HEA show much larger k_{p1} values than k_{p2}, corresponding to the higher oxidation rate in the initial stage of oxidation. By increasing Al content from 3.9 at % (Al0.2) to 7.6 at% (Al0.4), the k_p value of Al0.4 HEA decreased about one order of magnitude to 0.28×10^{-14} $g^2\cdot cm^{-4}\cdot s^{-1}$ comparing with k_{p1} of Al0.2 HEA, suggesting that there would be a significant difference in the initial oxidation behavior of them. However, the k_p value of Al0.4 HEA seems not change much comparing with k_{p2} of Al0.2 HEA, which may due to the formation of protective oxide scales on both alloys during long-term oxidation. By the further increment of Al to 10.5 at%, Al0.6 HEA exhibited the lowest k_p value among all three HEAs. Further analysis on the short-time oxidation would be helpful for a better understanding of the oxidation kinetics and scale formation process, which will be discussed in section **4.4.1**.

4.3.3 Morphologies and phase compositions of oxide scales

Fig. 4.5 shows the surface morphologies and cross sections of the oxidized Al0.2, Al0.4 and Al0.6 HEAs after oxidation at 700 °C for 100 h. The Al0.2 and Al0.4 HEAs show relative rough surface with large particles (**Fig. 4.5a** and **b**), while the Al0.6 HEA appears to be less oxidation with smaller particles (**Fig. 4.5c**). The oxide scale morphologies were further observed on the cross-sections of each sample. As shown in **Fig. 4.5d-f**, the thickness of oxide scale formed on each alloy decreased with the increased Al content, which is consistent with the order of mass gain among these three alloys. Al0.2 and Al0.4 alloys display thicker oxide scales including at least two layers, a top layer with some holes in bright contrast and a relatively adherent inner layer with dark contrast. The oxide scale formed on Al0.6 was thinner than 1 μm, indicating the best oxidation resistance in this study. The above-mentioned results support the less

oxidation mass gain and the smaller k_p values in high Al HEAs.

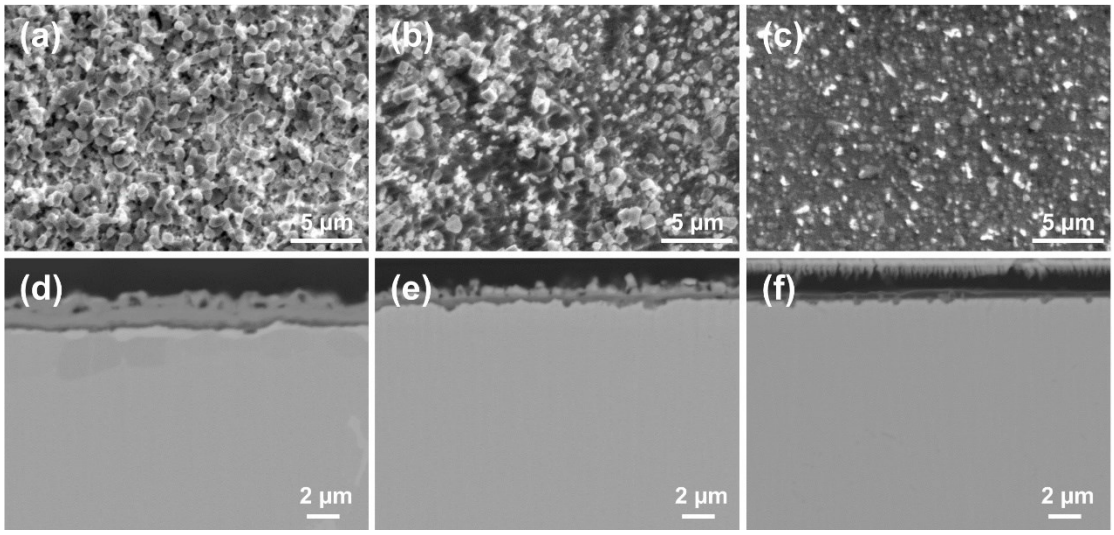

Fig. 4.5 SEM surface morphologies and cross sections of HEAs after oxidation at 700 °C for 100 h: (a, d) $Al_{0.2}CrCuFeNi_2$; (b, e) $Al_{0.4}CrCuFeNi_2$; (c, f) $Al_{0.6}CrCuFeNi_2$.

The XRD pattens of Al0.2, Al0.4 and Al0.6 HEAs after oxidation were shown in **Fig. 4.6**. All three alloys keep the FCC-typed substrate structure with similar oxides formation, suggesting similar oxidation mechanisms. The spectra of Al0.2 HEA shows the oxide scale mainly consists of spinel-type oxides ($NiFe_2O_4$, which will be confirmed later in section **4.3.4**) with Cr_2O_3 and Al_2O_3. By increasing the Al concentration, the intensity of $NiFe_2O_4$ ($2\theta \approx 30.2°$, 35.6°, 62.8°) decreased gradually in Al0.4 and Al0.6 HEA, indicated a decrease in the formation of spinel oxide. The presence of Cr_2O_3 and Al_2O_3 were also recognized on the Al0.4 and Al0.6 HEAs, however the signals are relatively weak due to the less amount of the oxide scale. Besides, a small amount of Cu_2O and NiO were also detected in the diffraction peaks of Al0.2 and Al0.4 HEAs, which may probably form in the initial oxidation stage. The formation of protective Cr_2O_3 and Al_2O_3 would be the reason of a better oxidation resistance in this HEAs system.

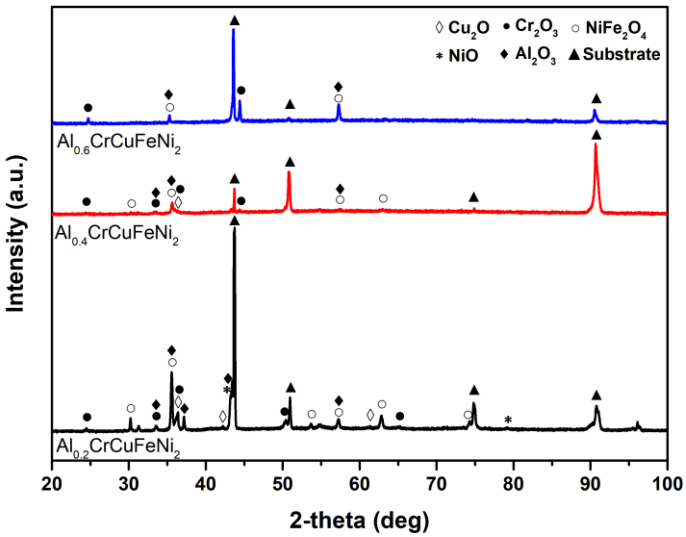

Fig. 4.6 XRD spectra of HEAs after oxidation at 700 °C for 100 h.

4.3.4 Microstructure and chemical compositions of oxide scales

Fig. 4.7 shows the cross-sectional EPMA elemental mappings with the corresponding backscattered electron (BSE) micrograph of the oxide scale formed on each tested sample, in which (a), (b) and (c) belongs to the Al0.2, Al0.4 and Al0.6 HEA, respectively. According to the element distribution of oxygen and BSE images, it is apparent that the Al0.2 HEA possessed the thickest oxide scale (~2 μm), which agrees well with the largest mass gain exhibited in **Fig. 4.4**. With increasing the Al content to 7.6 at% and 10.5 at%, Al0.4 HEA and Al0.6 HEA show significant decrease in scale thickness to less than 1 μm and 0.5 μm, respectively. The oxide scale formed in three alloys displayed similar triplex oxide layer structure: an external layer composed of Fe, Ni and O, an intermediate layer rich in Cr and O, and an inner layer formed by reaction between O and Al in the substrate. The Fe, Cr, and Al-rich scales formed on alloys were corresponding to the oxides of $NiFe_2O_4$, Cr_2O_3 and Al_2O_3 observed by XRD spectra in **Fig. 4.6**. Although the scale structures of the alloys are close to each other, the elemental

distribution of them changed a lot by adjusting Al concentration. From the elemental maps of Fe, it can be seen that Al0.2 alloy displays a continuous Fe-rich scale with the largest thickness, and the Al0.4 alloy shows relative continuous Fe oxide with decreased scale thickness, while the enrichment of Fe on Al0.6 alloy was not obvious, with very low intensity in EPMA mapping result. Similar Cr behavior can be also found in the mappings. The Fe and Cr enrichment in the oxide scale led to a significant depletion of these element in the underlying substrate. The enrichment of Cu and Ni were observed at the alloy/oxide interface due to the selective oxidation of other elements. Besides, a small amount of needle-like enrichment of Cr inside the substrate can also be detected in Al0.6 HEA, which demonstrate the existence of Cr-rich precipitates (probably BCC phase) during long time oxidation. Similar precipitation phenomena were also found in $AlCrCuFeNi_2$ HEA after 700 - 900 °C annealing for 1-5 days [29].

For further analysis on the detail microstructure information of each scale, STEM observations on each alloy were conducted. **Fig. 4.8** shows the STEM HADDF images of the cross sections of $Al_xCrCuFeNi_2$ HEAs. **Figs. 4.9-11** show the enlarged view of STEM images and corresponding EDS analysis, which was conducted in the same square regions in **Figs. 4.8a-c**, respectively. From **Fig. 4.8a** and **Fig. 4.9a**, the triplex oxide scale can be observed in Al0.2 alloy. However, in contrast with the relative homogeneous Al-rich scale observed by EPMA (**Fig. 4.7a**), the inner oxide scale in **Fig. 4.8a** shows a discontinuous Al-rich area (left middle) and relative continuous Al-rich area (black contrast layer in the right middle of the image). The STEM mappings in **Fig. 4.9a** identified the existence of internally oxidized Al as well as external Al_2O_3 scale formation. By further checking the EPMA cross sections, we found that the discontinuous Al-rich scale contains about 20 % of the total CCP polished specimen. This interesting finding suggests that the Al content of Al0.2 (~4 at% Al) is probably

the boarder-line composition of internal and external Al_2O_3 formation in the current $Al_xCrCuFeNi_2$ HEA system. The formation of multiple oxide scales can be verified by STEM-EDS mappings and point analysis. As can be seen from Al0.2 alloy in **Fig. 4.9**, the atomic ratio of the Cu-rich (point1) and Ni-rich (point 2) particles are close to Cu_2O and NiO, respectively. Combining with the XRD and EDX mapping results, it can be concluded that Cu_2O and NiO were formed on Al0.2 alloy. Similarly, the Fe-Ni rich region (point 3) shows close proportion to $NiFe_2O_4$, which further support the determination of the Fe-Ni rich spinel oxide in the outer scale. It is also clear to see the high enrichment of Cr (point 4) and Al (point 6) in the inner oxide layer, which corresponds to the formation of Cr_2O_3 and Al_2O_3. A strong intensity of Cu-rich layer with lack of oxygen can be also detected just above the matrix, which probably due to the outward diffusion of other elements.

In the case of Al0.4 and Al0.6 HEA shown in **Fig. 4.10-11**, the total scale thickness decreased significantly from ~2 μm in Al0.2 HEA to ~0.7 μm and 0.3 μm in Al0.4 and Al0.6 HEA, which is consistent with the results of EPMA and the lower mass gain of high Al content alloy. In addition, the volume fraction of each oxide layer also changed. By increasing Al content from 4 at% (Al0.2) to 7 at% (Al0.4) and 11 at% (Al0.6), the amount of outer Fe-rich spinel oxide scale decreased almost one order of magnitude, from 1 μm thickness to less than 0.3 and 0.1 μm, respectively. On the other hand, the volume fraction of protective Cr and Al-rich scales increased, from about 45% in Al0.2 to 66% in Al0.6 alloy. The decrease of spinel oxide scale can be explained by the more continuous and uniform protective scale formation due to the higher Al supply in high Al content alloys, which prevent further oxidation. In addition, the oxide of Cu_2O can be also found on Al0.4 HEA in smaller size and amount compared with Al0.2 alloy, while it was hard to found on Al0.6 alloy. No NiO oxide was detected either on Al0.4

or Al0.6 HEA.

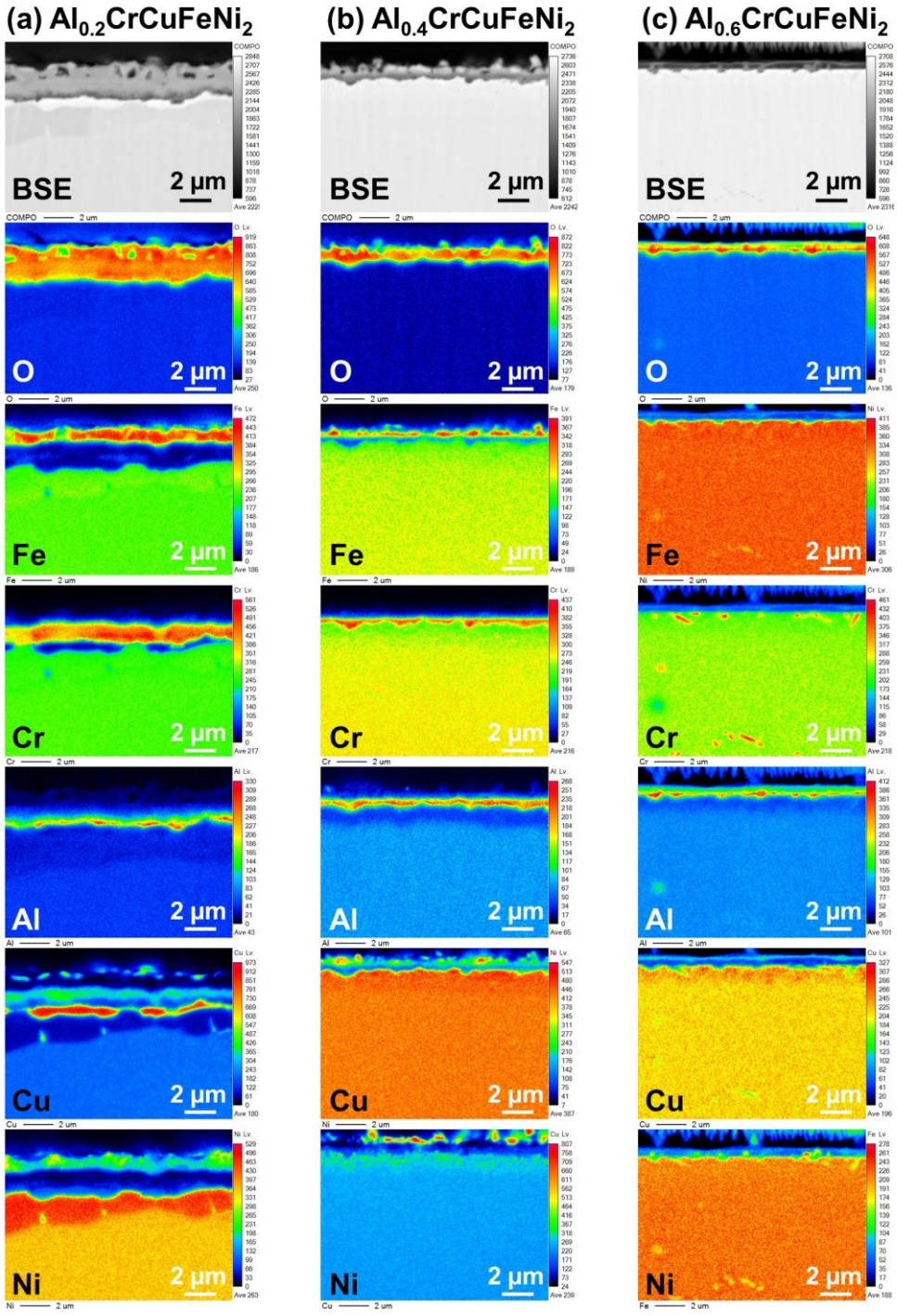

Fig. 4.7 EPMA elemental maps of $Al_xCrCuFeNi_2$ alloys after steam oxidation at 700 °C for 100 h.

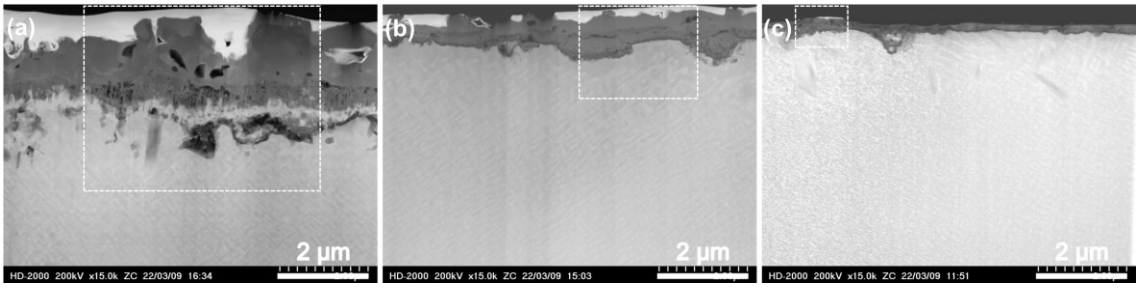

Fig. 4.8 STEM HADDF images of (a) $Al_{0.2}CrCuFeNi_2$ (b) $Al_{0.4}CrCuFeNi_2$ and (c) $Al_{0.6}CrCuFeNi_2$ HEAs after steam oxidation at 700 °C for 100 h.

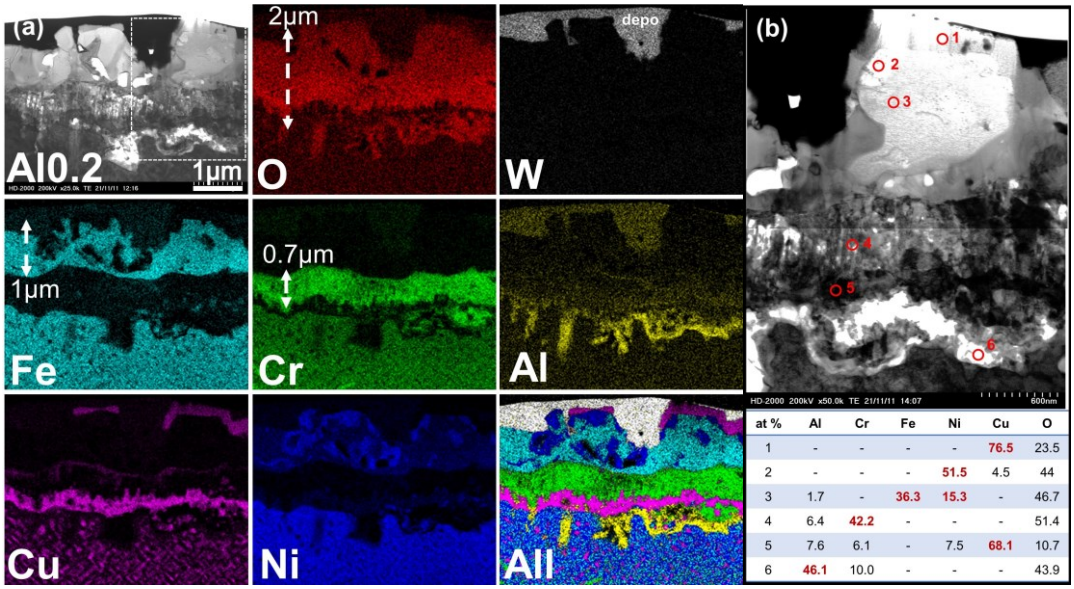

at %	Al	Cr	Fe	Ni	Cu	O
1	-	-	-	-	76.5	23.5
2	-	-	-	51.5	4.5	44
3	1.7	-	36.3	15.3	-	46.7
4	6.4	42.2	-	-	-	51.4
5	7.6	6.1	-	7.5	68.1	10.7
6	46.1	10.0	-	-	-	43.9

Fig. 4.9 (a) STEM image and corresponding elemental mappings and (b) zoomed view of white square area in (a) with STEM-EDS point analysis of oxide layers in $Al_{0.2}CrCuFeNi_2$ alloy after steam oxidation at 700 °C for 100 h.

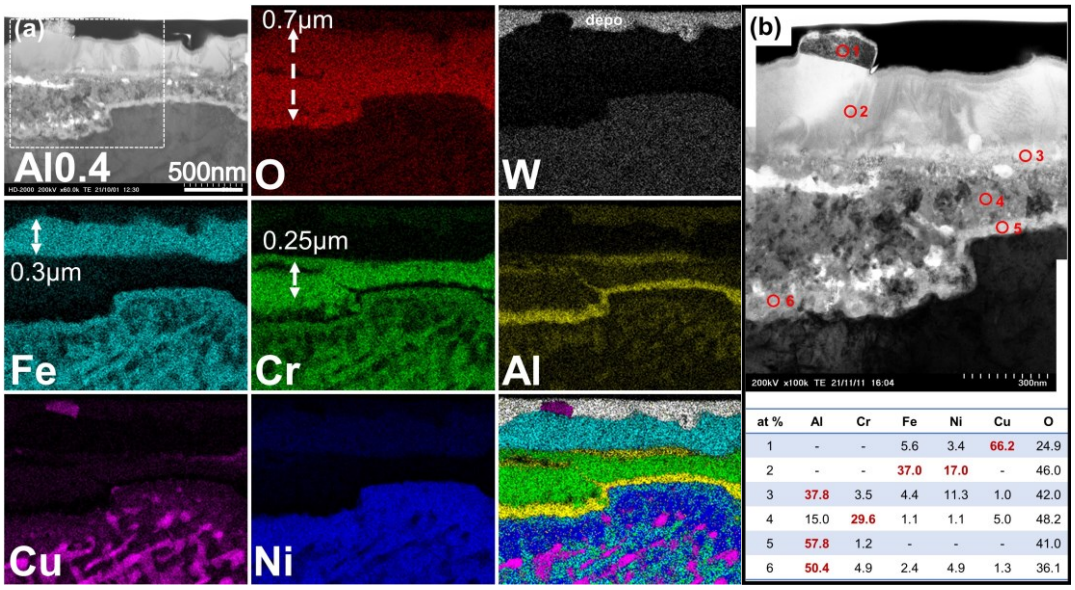

at %	Al	Cr	Fe	Ni	Cu	O
1	-	-	5.6	3.4	66.2	24.9
2	-	-	37.0	17.0	-	46.0
3	37.8	3.5	4.4	11.3	1.0	42.0
4	15.0	29.6	1.1	1.1	5.0	48.2
5	57.8	1.2	-	-	-	41.0
6	50.4	4.9	2.4	4.9	1.3	36.1

Fig. 4.10 (a) STEM image and corresponding elemental mappings and (b) zoomed view of white square area in (a) with STEM-EDS point analysis of oxide layers in $Al_{0.4}CrCuFeNi_2$ alloy after steam oxidation at 700 °C for 100 h.

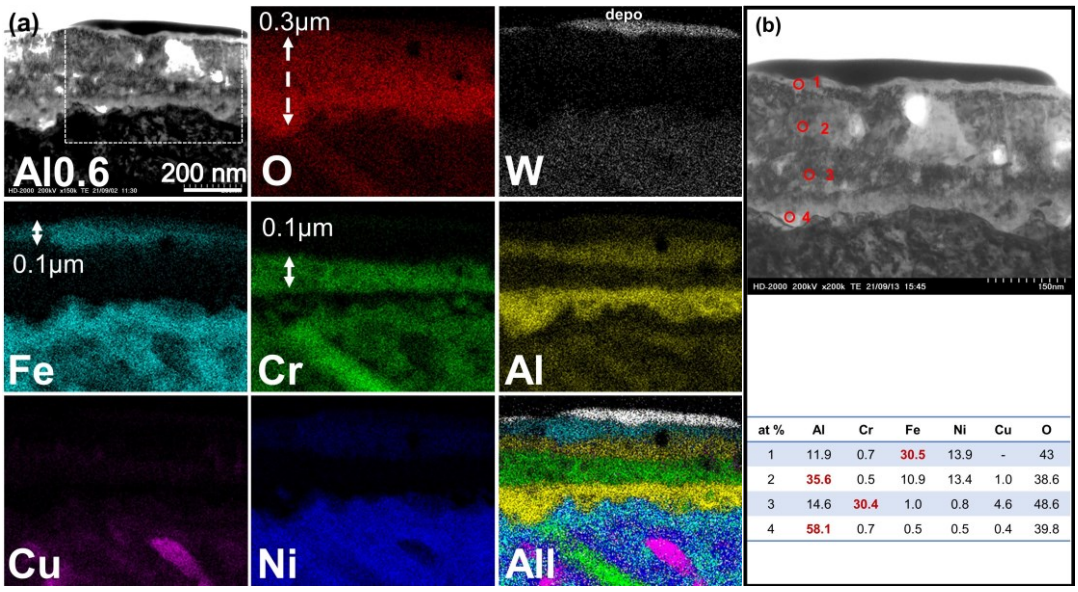

at %	Al	Cr	Fe	Ni	Cu	O
1	11.9	0.7	30.5	13.9	-	43
2	35.6	0.5	10.9	13.4	1.0	38.6
3	14.6	30.4	1.0	0.8	4.6	48.6
4	58.1	0.7	0.5	0.5	0.4	39.8

Fig. 4.11 (a) STEM image and corresponding elemental mappings and (b) zoomed view of white square area in (a) with STEM-EDS point analysis of oxide layers in $Al_{0.6}CrCuFeNi_2$ alloy after steam oxidation at 700 °C for 100 h.

4.4 Discussion

4.4.1 Short term oxidation

To further understand the influence of Al on the scale formation process, short-term oxidations of were conducted on all three $Al_xCrCuFeNi_2$ HEAs at 700 °C in steam. **Fig. 4.12 and Fig. 4.13** show the STEM EDS mappings of Al0.2, Al0.4 and Al0.6 HEA after 4 h and 16 h oxidation, respectively. As shown in **Fig. 4.12**, Al0.2 HEA has already formed Fe-Ni rich spinel oxide on the top of the scale within 4 h of oxidation. A large scale of Cr coexisted with Cu and O was just formed below the spinel oxide. However, no obvious Al-rich oxide layer was found in this early stage of oxidation in Al0.2 HEA. On the other hand, slight enrichment of Al oxide was observed in Al0.4 alloy, and the external Al oxide scale became more continuous in Al0.6 HEA. This suggests that the Al0.2 HEA was not able to develop the protective Al_2O_3 scale within 4 h, leading to relatively fast oxidation with a higher k_{p1} value than Al0.4 and Al0.6 HEAs in the initial stage of oxidation.

Further oxidation of Al0.2 alloy to 16 h evidenced a thicker spinel-type oxide scale than 4 h (**Fig. 4.13a**), while that of Al0.4 and Al0.6 alloys does not change much (**Fig. 4.13b-c**). Besides, a small amount of Cu-rich oxide was also detected on the upper side of spinel oxide in Al0.2 HEA. Moreover, the Al starts to enrich below the inner Cr_2O_3 scale in Al0.2 alloy after 16 h, which could somehow prevent the outer diffusion of other elements (Fe, Ni and Cu) for further oxidation, thus the oxidation kinetics starts to decrease slightly. Combining with the parabolic plot in **Fig. 4.4b** and element mappings in **Fig. 4.9a**, the discontinuous internal Al_2O_3 oxide would become more continuous after 25 h and partially changed to external scale after 100 h, leading to a significant decrease in the k_p value during long-term oxidation. On the other hand, the

protective Al_2O_3 oxide scale has already formed on Al0.4 and Al0.6 HEAs after 4 h oxidation and remained for a longer time, which is reasonable for their single oxidation kinetics followed by a single parabolic rate constant.

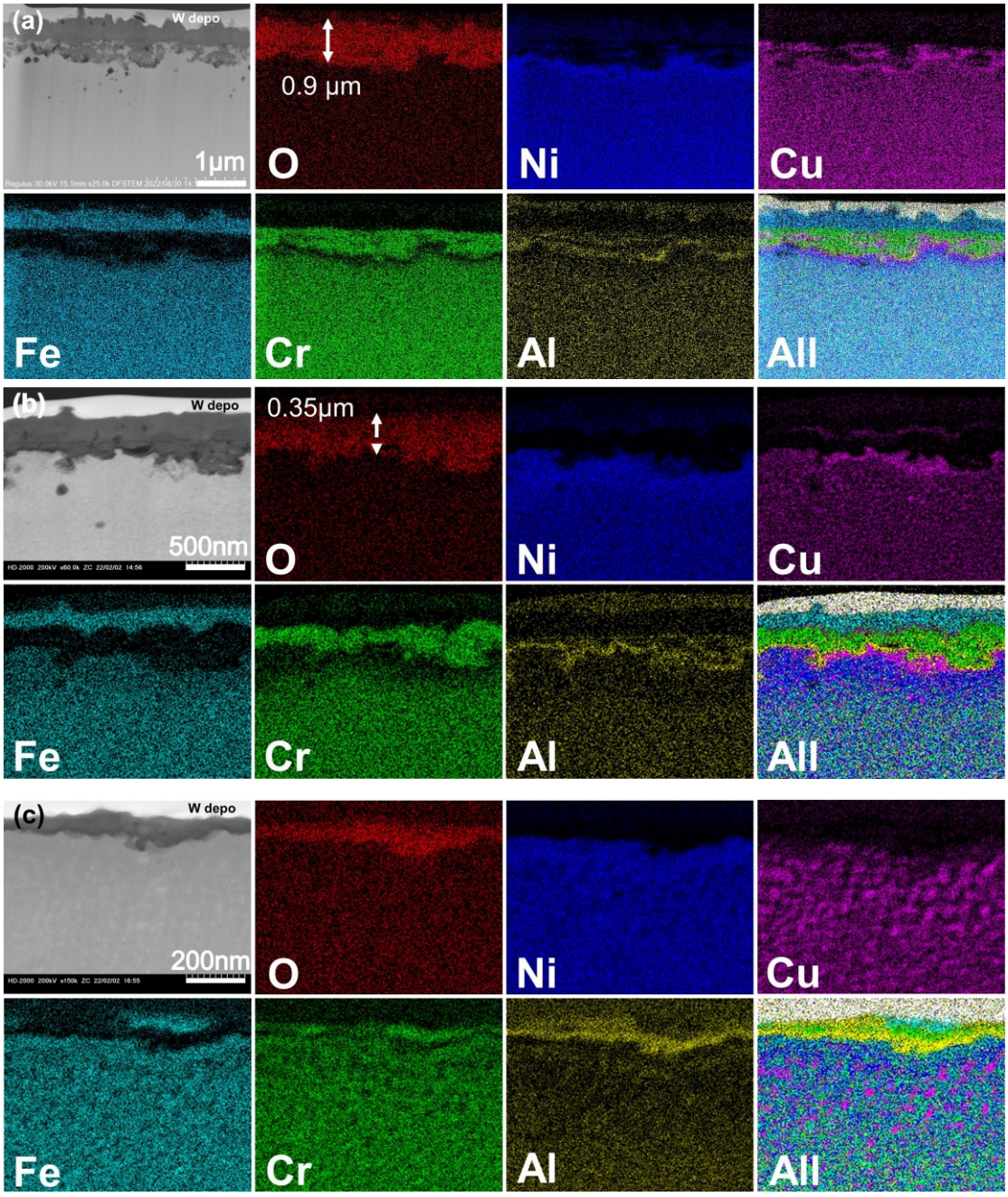

Fig. 4.12 STEM images and corresponding elemental mappings of (a) $Al_{0.2}CrCuFeNi_2$ (b) $Al_{0.4}CrCuFeNi_2$ and (c) $Al_{0.6}CrCuFeNi_2$ HEAs after steam oxidation at 700 °C for 4 h.

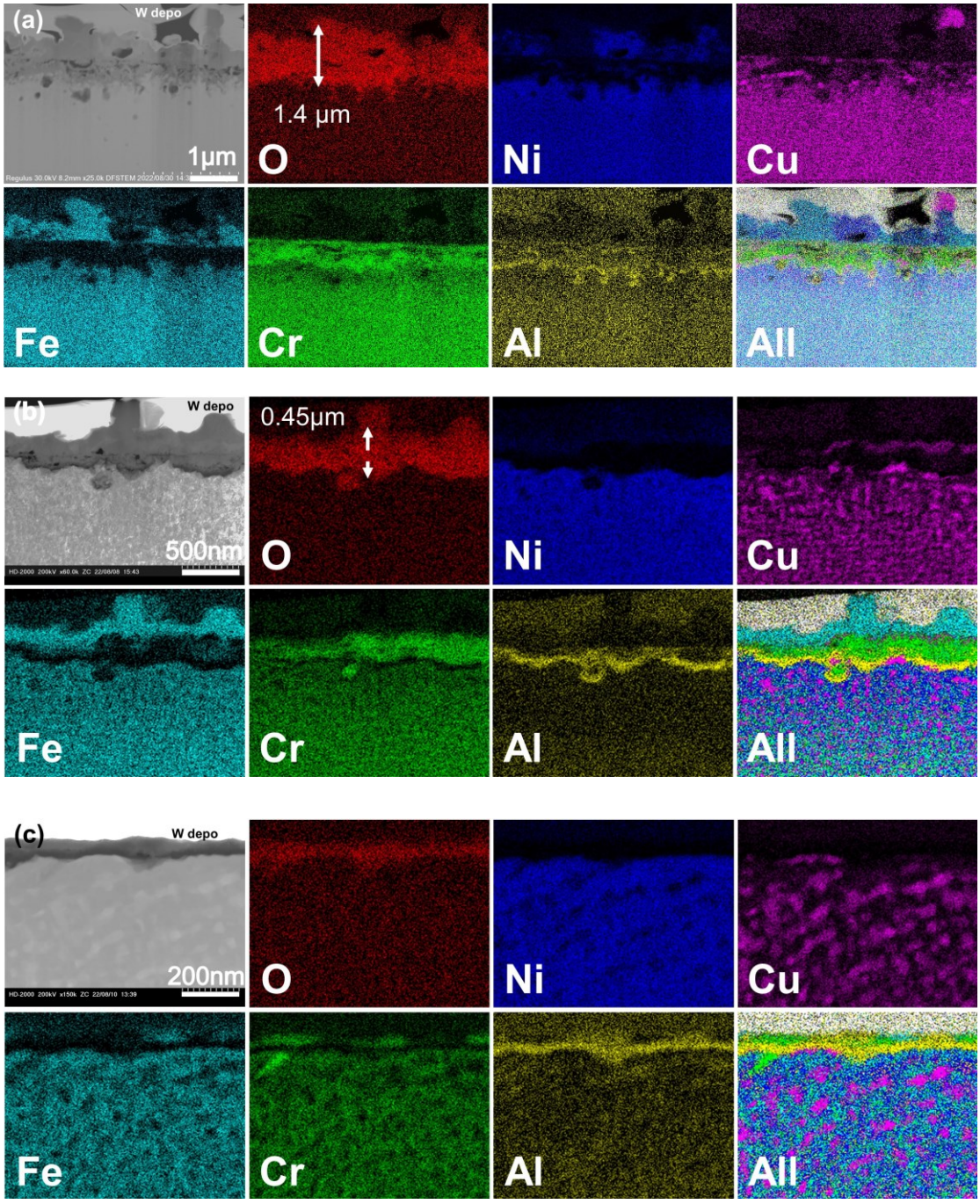

Fig. 4.13 STEM images and corresponding elemental mappings of (a) $Al_{0.2}CrCuFeNi_2$ (b) $Al_{0.4}CrCuFeNi_2$ and (c) $Al_{0.6}CrCuFeNi_2$ HEAs after steam oxidation at 700 °C for 16 h.

4.4.2 Influence of Al on oxidation behavior

The study of short-term and long-term oxidation in $Al_xCrCuFeNi_2$ HEAs show that the formation of protective external Al_2O_3 scale is quite sensitive to the Al content. According to the Gibbs free energy of oxide formation (ΔG_f^O), Al_2O_3 shows the lowest ΔG_f^O value than other possible oxides in this study (Al_2O_3 < Cr_2O_3 < Fe-oxides < NiO < Cu_2O), suggesting a high possibility of prior oxidation thermodynamically. However, the Al supply from the matrix is different from Al0.2 to Al0.6 HEA. The critical content for an external oxide BO formation (N_B^O) can be estimated by the equation [34]

$$N_B^O = (g_{BO}^* \frac{\pi}{2v} \frac{V_A}{V_{OX}} \frac{N_O^{(s)} D_O}{D_B})^{1/2} \quad (2)$$

Where g_{BO}^* is the specified volume fraction of BO, V_A and V_{OX} are the molar volumes of the alloy and the oxide; $N_O^{(s)}$ is the oxygen solubility in the B-depleted alloy substrate; D_O and D_B denote the diffusion coefficient of O and B, respectively.

From equation (2), the formation of external oxide scale is a competition between the oxidant permeability $N_O^{(s)} D_O$ and the corresponding alloy quantity $N_B^O D_B$. In the case of Al0.2 HEA, the oxygen flux on the alloy surface is high enough in the initial stage of oxidation while Al supply was not sufficient compared with other solute elements, hence the Cr_2O_3 and spinel-type oxide were more likely to form before Al_2O_3 scale formation. Besides, the existence of the Cr-rich scale can decrease the oxygen solubility to a deeper part of the matrix, however the formation of Al_2O_3 with lower ΔG_f^O can be possible and it internally precipitated beneath Cr_2O_3 scale in the long-term oxidation, as shown in **Fig. 4.9**. While, different scale formation behavior was observed in high Al content alloys. As shown in **Fig. 4.12 b-c**, the Al content in Al0.4 and Al0.6 alloys is high enough to sustain a sufficient flux for the continued growth of initial precipitates, their enlargement leads to the transformation to a continuous external

Al_2O_3 layer. As indicated previously, the co-exitance of internally oxidized precipitates and external Al_2O_3 scale in Al0.2 alloy suggest that there would be a border-line composition between internally oxidation and external Al_2O_3 scale formation. From an experimental observation work of Ni - 8 at% Cr - 8 at% Al alloy by B. Gleeson et al. [85], after oxidation at 1100 °C in air for 4 h, a “pear” shape morphology of the precipitates and a relative continuous Al_2O_3 layer were both observed on one specimen, and the continuous Al_2O_3 layer were likely to established by the connection of the originally discrete precipitates. Similarly, the result of current study indicated that the Al0.2 alloy with the amount of 4 at% Al is close to the transition point from internal to external oxidation.

In short, $Al_xCrCuFeNi_2$ HEAs tend to form multiple external scales instead of only one exclusive scale on the alloy due to the high alloying composition of elements. The high Al content provide sufficient Al supply for the formation of more continuous external Al_2O_3 layer, which acts as a protective barrier separating the alloy from the oxidant environment, thereby reducing the growth of the oxide layer.

4.4.3 Oxidation mechanism

The oxidation kinetics of three HEAs show different parabolic behavior, which Al0.2 HEA exhibited a two-stage oxidation kinetics with a marked decrease of k_p value in the long-term oxidation, while Al0.4 and Al0.6 HEAs show simple parabolic behavior. The k_p values decreased by increasing the Al content. The reduced mass gain and improved oxidation resistance was mostly achieved by the early formation of Cr/Al rich oxide scales during initial oxidation in high Al HEAs, and further growth of a protective layer contributed to the long-term oxidation resistance.

An early study on Ni-Cr-Al alloys by Giggins and Pettit [86] revealed that the formation of oxide scale between 1000 and 1200 °C can be divided into three groups based on the Cr and Al content. Group I related to the alloy with limited amount of Cr and Al, which is too low to establish continuous Cr_2O_3 or Al_2O_3 scales. Thus, the non-protective NiO and spinel-type phases form with internal oxidation of Al; Group II corresponds to the alloys with large enough Cr but relatively low Al content, which results in the selective oxidation of Cr with external Cr_2O_3 scale and internal subscale of Al_2O_3; Group III related to the alloys with higher concentrations of both Cr and Al, which promotes the formation of a highly-protective external Al_2O_3 scale with or without minor Cr_2O_3 formation. This famous founding was widely accepted and further applied on the Al-Cr-Ni containing HEAs by Butler and Dabrowa [87, 88]. According to the scale morphologies shown in section **3.3**, the evaluated alloys in our work can be classified into two groups: the Al0.2 HEA can be assigned to the Group II due to the relatively low Al content, and Al0.4 and Al0.6 HEAs can be include into the Group III in the Giggins-Pettit theory.

Fig. 4.14 illustrates the schematic graph of the oxide scale formation process of $Al_xCrCuFeNi_2$ HEAs by different stages of oxidation. The total scale thickness of the alloys decreased with the Al content increased. Al0.2 HEA developed the outer spinel oxide scale with no-obvious Al-rich scale in the short-term oxidation, followed by partial internal Al_2O_3 scale formation in the long-term oxidation. Al0.4 and Al0.6 developed less spinel oxide with external Cr_2O_3 and Al_2O_3 scales at 4 h, and those protective scales grew thick at 100 h.

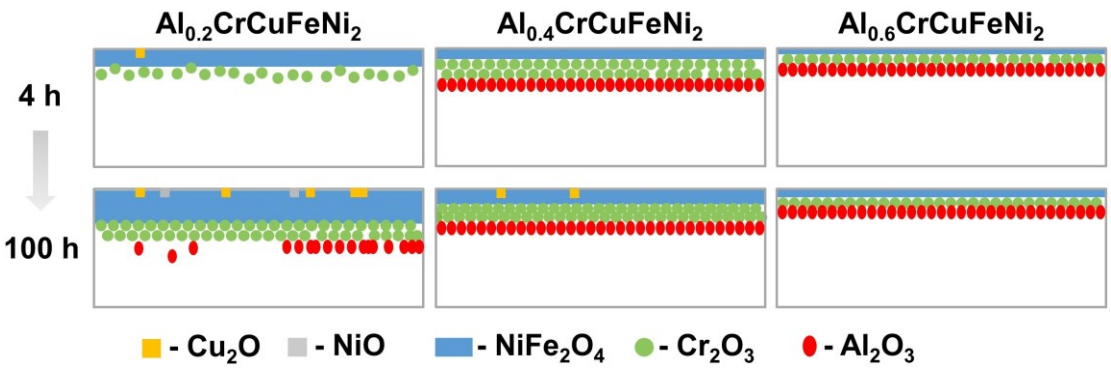

Fig. 4. 14 Schematic graph of the oxide scale formation process on $Al_xCrCuFeNi_2$ HEAs.

The formation of external spinel-type oxide in $Al_xCrCuFeNi_2$ HEAs could be started during a transient period of oxidation before 4 h, according to the reports in Ni-Cr-Al and Fe-Cr-Al alloys [89, 90]. During transient oxidation, all elements including Fe, Ni and Cu in the substrate oxidized simultaneously due to the initial high oxygen partial pressure. Then, the initially formed oxides remained in the longer time of oxidation and grew to a critical sufficient amount to decrease the oxygen partial pressure, thereby a steady state with local equilibrium established. The separation of each scale depends on the stability and diffusivity of each cation. Cu_2O is less stable due to the lowest Gibbs free energy of oxide formation, which should be formed on the upper side of the scale. Then Ni and Fe oxides reacted to form spinel-type oxide ($NiFe_2O_4$) below Cu_2O, followed by Cr and Al oxides to form a layer-by-layer structure. After 16 h oxidation, the outer spinel oxide layer grew thicker in Al0.2 HEA due to the discontinuous Al_2O_3 with limited protection. The protectiveness of Al_2O_3 further increased until a relative continuous Al-rich scale developed, thereby decreasing the growth of the outer spinel oxide layer during long-term oxidation. Compared with Al0.2 HEA, the less formation of spinel oxide in Al0.4 and Al0.6 HEAs also shows the increased protectiveness of the Al_2O_3 scale by increasing Al content.

As mentioned before, the Al content of Al0.2 alloy is close to the transition point from internal to external oxidation. Coincidently, the composition of Al0.2 alloy (3.9 at% Al and 19.1 at% Cr) lies very close to the boundary of Group II and Group III in the schematic oxide map for the ternary Ni-Cr-Al system in reference [87, 88], although the oxidation temperature (1000 °C) is higher than current study (700 °C). Thus, it induced that the above-mentioned oxide formation theory is quite suitable to the $Al_xCrCuFeNi_2$ HEA system in this study. However, the diffusion of Al at 700 °C could be slower than 1000 °C, which may increase the critical concentration of Al for external scale formation. The similar boundary composition shown in Al0.2 HEA at lower oxidation temperature than that of Ni-Cr-Al alloys suggests the advantage of oxidation resistance in HEAs, which might be due to the high entropy effect.

A quite recent study by Huang et al. reported a significant difference between the intragranular and grain boundary (GB) regions of $Al_{0.3}CrCuFeNi_2$ HEA after 750 °C oxidation [84]. They supposed that the two parts of the alloy displays different oxidization behavior. However, in our study, we were mainly focused on the general oxidation behavior inside the grain and the near grain boundary region seems to be less oxidized from the cross-sectional and surface morphology in the **Fig. 4.S2** and **Fig. 4.S3**. The probable reasons may come from the difference on the oxidation temperature and initial microstructure between the literature and the current study. More detailed information from the cross sections of the near boundary area would be needed to get a better understanding.

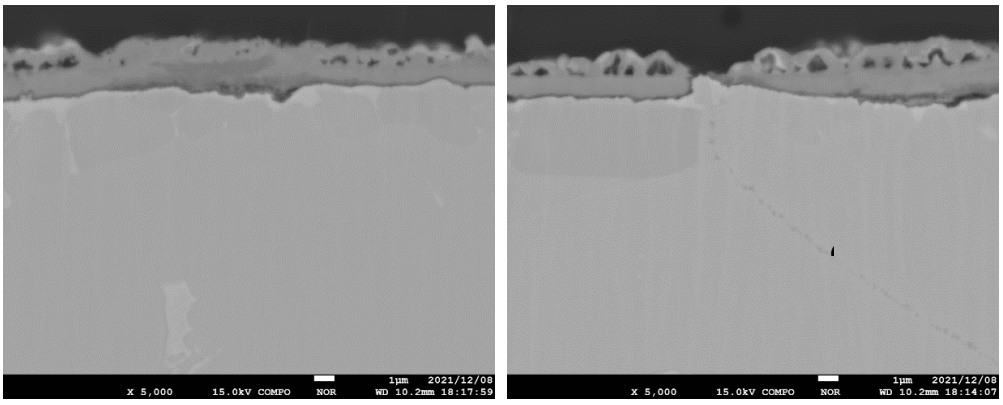

Fig. 4.S2 Cross-sections of $Al_{0.2}CrCuFeNi_2$ HEA after oxidation at 700 °C for 100 h.

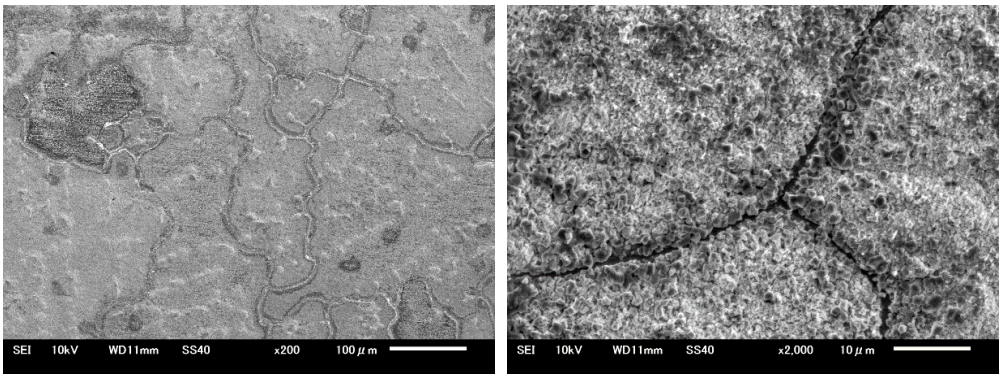

Fig. 4.S3 Surface morphologies of $Al_{0.2}CrCuFeNi_2$ HEA after oxidation at 700 °C for 100 h.

Moreover, another point needs to be mentioned in this $Al_xCrCuFeNi_2$ system is the formation of nano scale Cu segregation below the inner scale region. **Fig. 4.15** compares the STEM multi-element overlapped mappings of each tested HEA after 100 h oxidation. The size and distribution of Cu-rich area can be observed by the areas colored in magenta. It is clear that the size of Cu segregation increased from small particles in Al0.2 alloy to longer needle-shaped precipitates in Al0.4 and Al0.6 alloys. In addition, the Cu-rich area went deeper in high Al content HEAs. However, the effect of Cu segregation on the oxidation behavior of current study was not clearly found. A recent work by Hayashi et al. [62] reported that Cu was beneficial to enhance the

formation of external Al_2O_3 scale on Fe/Ni-based alloys. It is possible that the Cu segregation between the oxide and inner substrate may decrease the oxygen concentration and contribute to the protective scale formation.

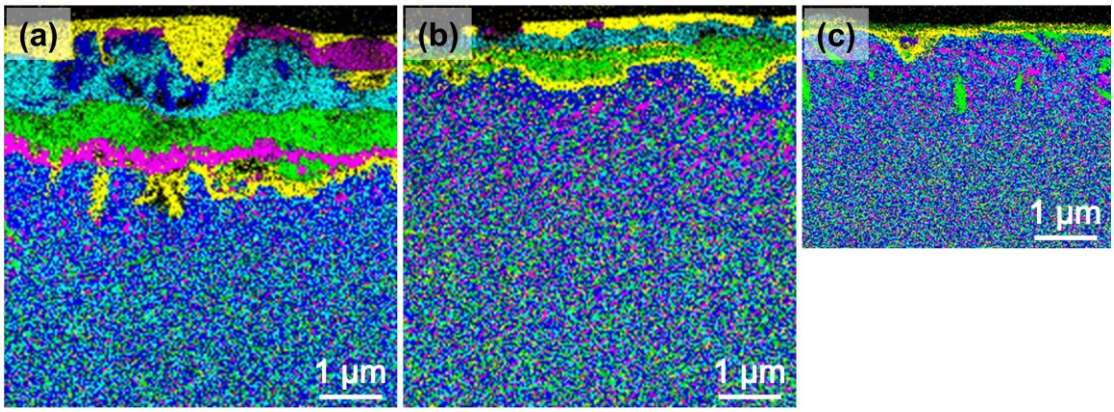

Fig. 4.15 STEM elemental mappings of (a) $Al_{0.2}CrCuFeNi_2$ (b) $Al_{0.4}CrCuFeNi_2$ and (c) $Al_{0.6}CrCuFeNi_2$ HEAs after steam oxidation at 700 °C for 100 h (the element of Cu is colored in magenta).

4.5 Summary

The oxidation behavior of $Al_xCrCuFeNi_2$ (x = 0.2, 0.4, 0.6) HEAs with various Al concentrations (3.9 at%, 7.6 at%, 10.5 at%) was studied at 700 °C in steam. The mass gain of each alloy follows the order of $Al_{0.6}CrCuFeNi_2$ < $Al_{0.4}CrCuFeNi_2$ < $Al_{0.2}CrCuFeNi_2$ after 100 h oxidation. $Al_{0.2}CrCuFeNi_2$ HEA showed two-stage oxidation kinetics with an initial fast-growing stage before 25 h and a slow-growing stage within 100 h, while $Al_{0.4}CrCuFeNi_2$ and $Al_{0.6}CrCuFeNi_2$ HEAs show single parabolic rate constants. The lower solute concentration of Al in $Al_{0.2}CrCuFeNi_2$ alloy led to a discontinuous Al_2O_3 distribution and much thicker Fe-Ni rich spinel oxides formation. By increasing Al content, the oxide scale thickness decreased significantly

by the establishment of continuous external Cr_2O_3 and Al_2O_3 oxide scales. Meanwhile, less Cu_2O and NiO oxide and thinner spinel oxide scales were formed on $Al_{0.4}CrCuFeNi_2$ and $Al_{0.6}CrCuFeNi_2$ HEAs. The analysis of short-term oxidation indicates that the improved oxidation resistance of high Al content HEAs may be due to the early formation of continuous Al_2O_3 scale in the initial stage of oxidation.

Chapter 5 Effect of irradiation on Co-free Cu-containing HEAs

5.1 Introduction

The research and development of advanced reactors require new structure materials with high corrosion and irradiation resistance at high temperatures. Co-free high entropy alloys (HEAs) attract many concerns due to the reduced radioactivity and high-temperature stability. Previous study on $CrCu_{0.3}FeNi$ and $Al_{0.4}CrCuFeNi_2$ HEAs shows better oxidation resistance than 316 SS at 500-700 °C, suggesting a possibility for high-temperature application. In this study, we compare the irradiation effect of $CrCu_{0.3}FeNi$ and $Al_{0.4}CrCuFeNi_2$ HEAs with commercial 316L and correlate the irradiation-induced hardening with the irradiated microstructure by TEM observation. The aim of this chapter is to evaluate the irradiation resistance of Co-free Cu containing HEAs with conventional alloys under high irradiation dose in advanced nuclear reactors.

5.2 Experimental

The $CrCu_{0.3}FeNi$ and $Al_{0.4}CrCuFeNi_2$ high entropy alloys were made by arc melting and solution annealed at different temperatures. All the tested alloys showed FCC phases with homogeneous composition. The atomic composition and solution annealing condition of each alloy are given in **Table. 5.1**. Bulk materials of HEAs and 316L SS were cut into $1 \times 4 \times 0.8$ mm and mechanically polished by 0.1 μm alumina suspension.

The specimens were irradiated with 6.4 MeV Fe^{3+} at 300 ℃ to a nominal damage peak of about 23 dpa using a dual-beam facility for energy science and technology (DuET) at Kyoto University. The total irradiation time is about 5 h. The irradiated region is in the center of the sample, while the unirradiated region s are on both sides of it. After irradiation, the samples were scratched around the boundary of the irradiated

and unirradiated region as a mark for further observation. A typical depth profile of the displacement damage calculated by the SRIM code for DuET facility was reported in [27]. The area near the surface strongly has the effect of surface sink, and the damage peak region has a large dpa gradient. As a results, a nominal dpa was defined as a displacement damage at a depth of 600 nm from the irradiated surface for a general comparison among different materials.

After irradiation, the surface morphology of the irradiated and unirradiated region was acquired by an atomic force microscope (AFM, Hitachi AFM400) with a dynamic force mode (DFM) cantilever (FI-DF40). A 100 μm type scanner with a Z resolution of 0.23 nm was chose to scan a surface area of 35 × 35 μm between the irradiated and unirradiated region.

To investigate the irradiation hardening, two kinds of nano-indentation experiments were conducted on both irradiated and unirradiated areas of the samples:
(1) Nano-indenter (Hysitron TI-950) for single indentation at a constant indentation depth of 250 nm, 16 typical indents were conducted on each areas with a distance of 20 μm which was larger than five times the largest indentation diameter.
(2) Nano-indenter (Agilent G200, Keysight tech.) with a Berkovich-type indentation tip for continuous stiffness measurement (CSM). CSM method was used to continuously obtain the hardness (H)-depth (h) profile with a single indent up to depth about 2 μm [38], which covers the entire irradiation layer. The amplitude and frequency of loading oscillation is 2 nm and 45 Hz, respectively. A total 10 test points were selected at random on each sample to avoid experimental errors. The distance between indents were 100 μm which was larger than five times the largest indentation diameter here.

The specimen for transmission electron microscope (TEM) observation was

extracted by focused ion beam (FIB, Hitachi FB2100; JEOL JIB-4601F) using 30kV Ga^+ for machining and 10kV Ga^+ for polishing. The reciprocal lattice rod (relrod) technique was applied to get the dark filed image of Frank loop on (1 1 1) plane.

Table 5.1 Chemical composition of the alloys for irradiation experiment.

Composition /at%	Al	Cr	Cu	Fe	Ni	Mn	Mo	Si	C	N	Solution annealing
$Cu_{0.3}$CrFeNi	-	29.77	9.11	30.77	30.35	-	-	-	0.005	0.0007	1076℃, 72h
$Al_{0.4}$CrCuFeNi_2	6.35	18.22	18.05	19.31	38.07	-	-	-	0.011	0.0004	1000℃, 24h
316L SS	-	17.59	-	Bal.	12.17	1.08	2.07	0.70	0.020	0.019	1150℃, 1.5h

5.3 Results and discussion

5.3.1 Damaged microstructure after irradiation

(1) Non-destructive observation of irradiated sample surface

Fig. 5.1 shows the AFM surface morphology images of 316L SS and $CrCu_{0.3}FeNi$ HEAs with irradiated and unirradiated regions. The brighter contrast means the higher value of measured surface height. It is clear to see that there is a boundary between irradiated and unirradiated region caused by the surface change by irradiation. To evaluate the step height of both alloys, boxed area was selected to get the averaged surface height of each alloy. The measured data was plotted in **Fig. 5.2**, which shows a significant decrease in step height from 7.2 nm in 316L to 4.6 nm in $CrCu_{0.3}FeNi$, indicating a higher swelling resistance of $CrCu_{0.3}FeNi$ HEA. However, the step height of $Al_{0.4}CrCuFeNi_2$ HEA was not successfully measured, as it shows nearly no distinction from irradiated and unirradiated region and it is hard to find the real

boundary, which may due to very tiny change in surface height that cannot be detected.

(2) TEM observation on the irradiated samples

Fig. 5.3a shows the damage distribution profile calculated by SRIM software. It can be seen that the damage peak reached to about 23dpa at 1.5 μm radiation depth. However, the dark field (DF) image taken from relrod of Frank loop on (111) plane in **Fig. 5.3b** showed that there is an obvious difference in the damage distribution distance between 316L and HEAs. **Fig. 5.3c** is the bright field image corresponding to **Fig. 5.3b**. The observed damage peak of 316L is around 1.56 μm, which is consistence with SRIM calculation results. While, the observed damage peak of HEAs reached about 1.8 μm, which is deeper than 316L. Similar difference in defect distribution between stainless steel and HEAs also reported by Lu et al [91]. The different behavior would be related to the defect nucleation and mobility as well as migration pathways.

In order to calculate the Frank loop size and number density of each alloy, we observed the irradiated area of top surface (from surface to 800 nm depth) and deep area around the damage peak, corresponding figures are shown in **Fig. 5.4** and **Fig. 5.5**, respectively. The calculated results were summarized in **Table 5.2** and **Table 5.3**. The observation from the top surface to 800nm depth shows that the HEAs have a similar averaged Frank loop size and number density with 316L. While, around damage peak of each alloy, the averaged lop size of HEAs seems to be slightly smaller than 316L, and the loop number density slightly increased but still in similar level.

The defect microstructure observation results show that $CrCu_{0.3}FeNi$ and $Al_{0.4}CrCuFeNi_2$ HEA exhibit comparable radiation resistance with 316L SS at relative low temperature of 300℃. Chen et al. [28] also found similar behavior of

$Al_{0.3}$CoCrFeNi and Cantor HEAs at 300℃, which is possibly most dislocation loops were formed through cascade condensation where the involvement of long-range diffusion of point defects was limited. Consequently, the features of HEAs that are supposed to be beneficial for irradiation resistance, such as sluggish diffusion and high configurational entropy, played little role in the microstructural evolution of HEAs at low irradiation temperatures. Another parallel work of Chen et al. [29] did irradiation experiment at 500℃ showed that $Al_{0.3}$CoCrFeNi HEA has the larger loop size and smaller loop density than 316H SS, which may due to a higher vacancy mobility to reduce the nucleation rate of HEAs.

Thus, further study on the irradiation behavior at higher irradiation temperatures (>500℃) would be needed for a better understanding of HEAs.

Table 5.2 Frank loop number density and averaged size of the alloys from surface to 800 nm.

Frank loop (size>5nm)	**316L**	**$Cu_{0.3}$CrFeNi**	**$Al_{0.4}$CrCuFeNi$_2$**
Number Density (N.D. / m^{-3})	1.32×10^{22}	1.63×10^{22}	1.19×10^{22}
Average size (d_{ave} / nm)	11.28	13.08	12.74

Table 5.3 Frank loop number density and averaged size of the alloys around damage peak of each alloy.

Frank loop (size>5nm)	**316L**	**$Cu_{0.3}$CrFeNi**	**$Al_{0.4}$CrCuFeNi$_2$**
Number Density (N.D. / m^{-3})	7.75×10^{21}	7.89×10^{21}	1.05×10^{22}
Average size (d_{ave} / nm)	14.17	15.53	11.43

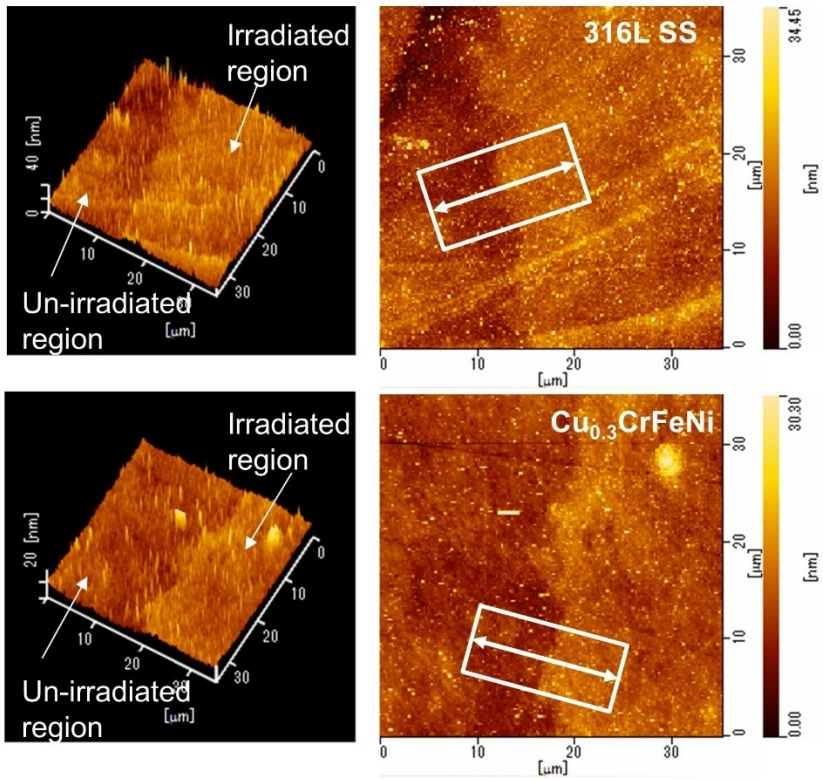

Fig. 5.1 AFM surface morphology after irradiation.

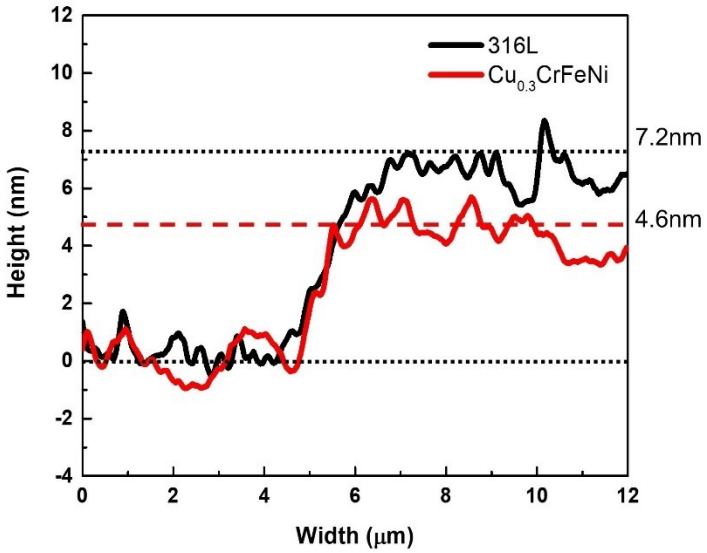

Fig. 5.2 Averaged surface height derived from the boxed area in **Fig. 5.1**.

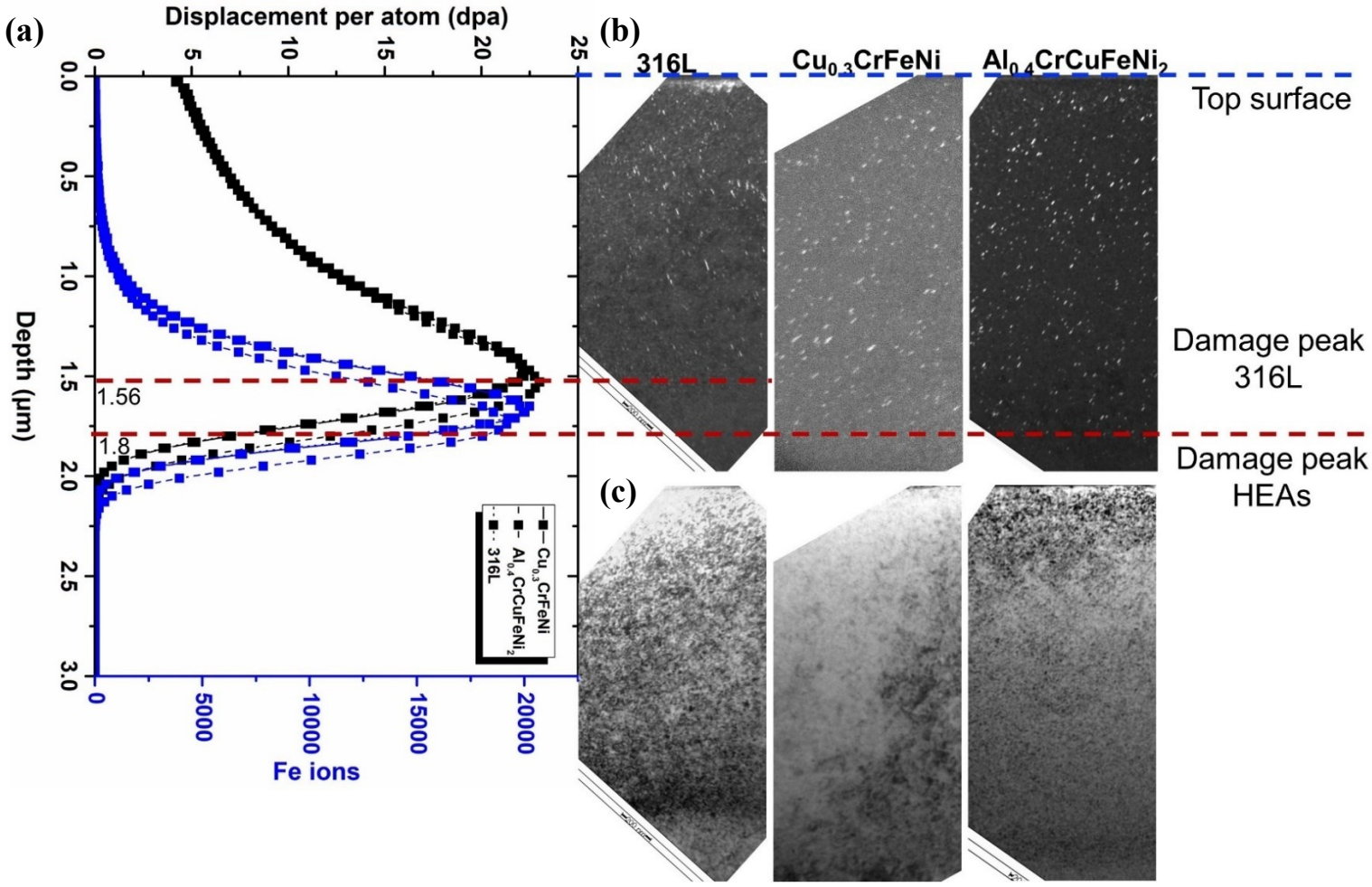

Fig. 5.3 (a) Damage distribution profile by SRIM calculation (b) Dark field image taken from relrod of Frank loop on (111) plane, B=[011] (c) Bright field image taken from the same area as (b).

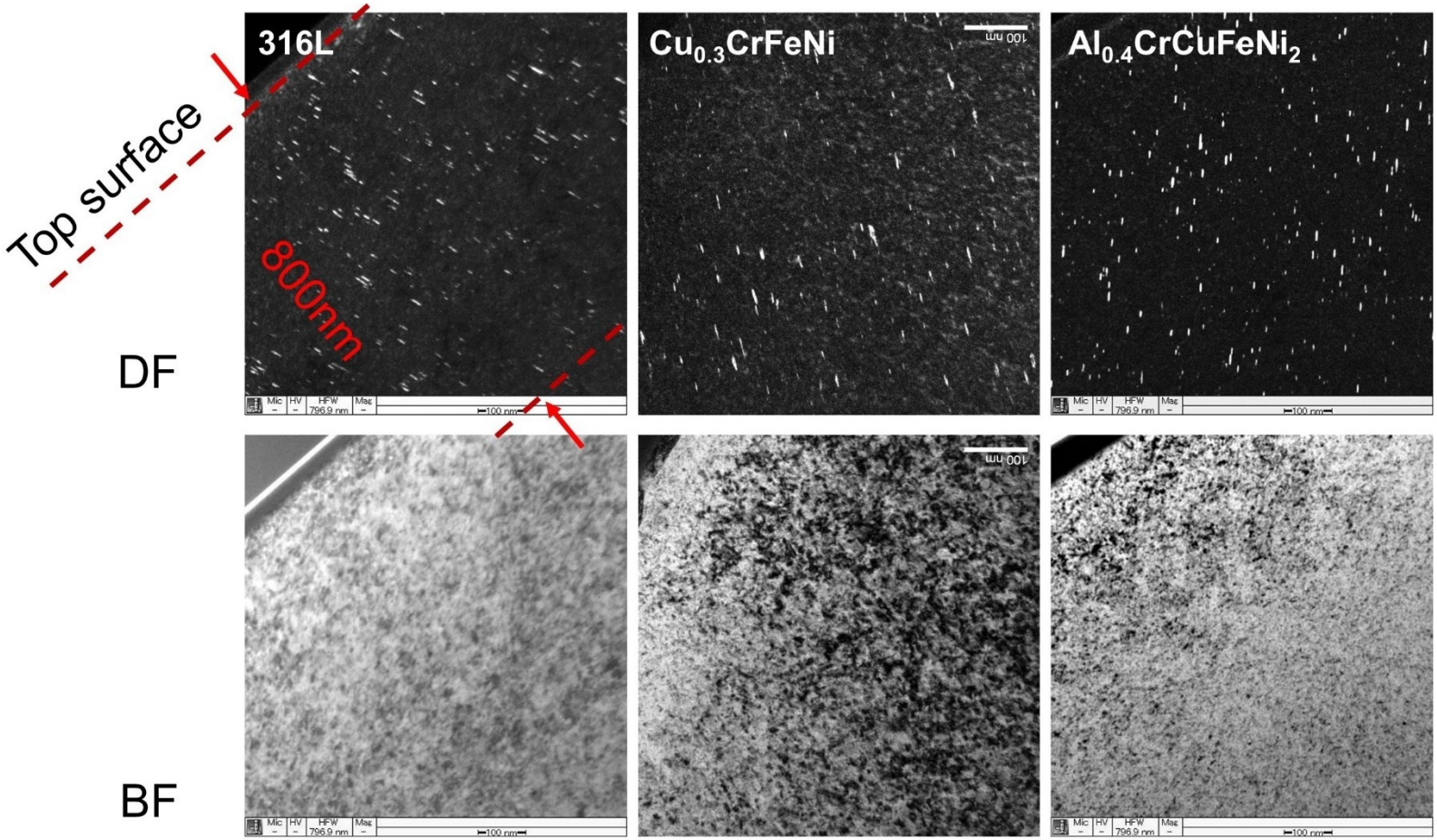

Fig. 5.4 TEM dark field (DF) and bright field (BF) images of 316L and HEAs taken near the top surface to irradiation depth of about 800 nm. DF images were taken from relrod of Frank loop on (111) plane, B=[011].

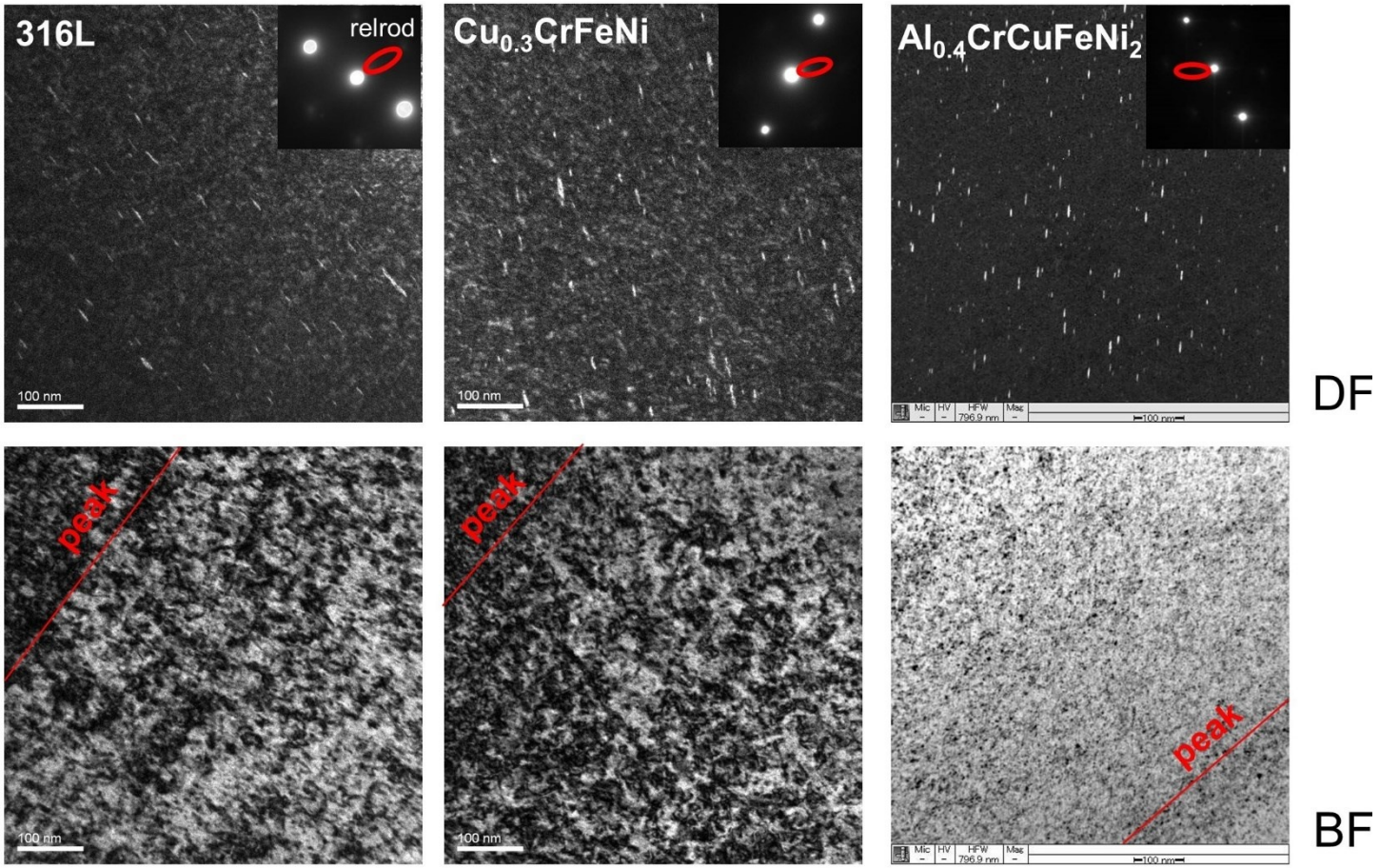

Fig. 5.5 TEM dark field (DF) and bright field (BF) images of 316L and HEAs taken close to the damage peak areas. DF images were taken from relrod of Frank loop on (111) plane, B=[011].

5.3.2 Irradiation induced hardening

Two types of nano-indentation experiments: (1) single depth indentation at a constant indentation depth of 250 nm and (2) continuous stiffness measurement (CSM) indentation from the sample surface to depth about 2 μm.

(1) Single depth indentation

Fig. 5.6 shows the nano-indentation hardness of each alloy. Before irradiation, 316L SS shows the lowest hardness of the matrix, while $Al_{0.4}CrCuFeNi_2$ HEA exhibit the highest hardness. After irradiation, the nano-hardness of 316L increased a lot, result in a highest irradiation hardening at the single indentation depth. The $CrCu_{0.3}FeNi$ and $Al_{0.4}CrCuFeNi_2$ HEA exhibit lower irradiation hardening (0.8GPa) than 316L (1.5GPa).

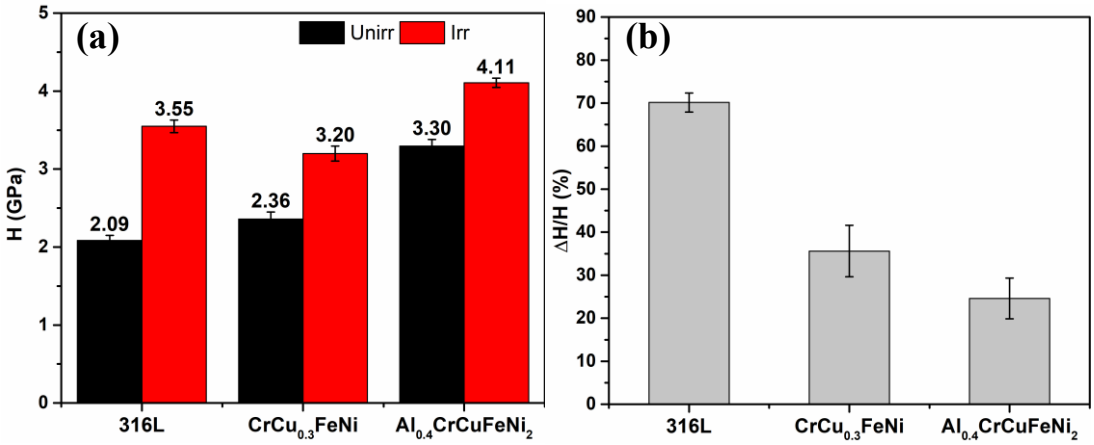

Fig. 5.6 (a) Single depth nano-indentation hardness of 316L SS and HEAs in irradiated and unirradiated region (b) irradiation hardening of 316L SS and HEAs.

(2) continuous stiffness measurement (CSM)

Fig. 5.7 shows the indentation modulus results from irradiated and unirradiated area of 316L and Co-free HEAs. All the tested samples show relative constant values of modulus, indicating a relative high effectiveness of CSM measurements.

Fig. 5.8 shows the relationship between the nano-hardness values and indentation depths of the unirradiated and irradiated samples. Due to factors such as the sharpness of the indenter, flatness of the sample surface and working state of the test machine, the data corresponding to the first 100 nm were highly inaccurate [92]. In this study, the data after 200 nm were took for characterization.

It is observed in **Fig. 5.8** that, the nano-hardness values of all tested alloys both increase after irradiation to a high dose. The "H^2 -1/h" curves were fitted with the Nix-Gao model to obtain the degree of irradiation hardening. These curves show that the hardness values decrease slightly with an increase in the indentation depth. This is well elucidated by the Nix-Gao model [40], which states that the nano-hardness changes with the indentation depth.

$$H = H_0\sqrt{1 + h^*/h}$$

Where H_0 is the hardness at limit infinite depth, while h^* is a characteristic length that depends on the shape of the indenter and the shear modulus of the materials.

Therefore, the nano-hardness of the irradiation layer can be obtained from the H_0. **Table 5.4** listed the calculated nanoindentation hardness and hardening of the tested alloys. The continuous stiffness measurement (CSM) results show that the irradiation induced hardening of HEAs are in the similar level compared with 316L SS at current irradiation condition.

To further explain the difference of single depth indention and CSM indentation, detailed analysis was conducted on TEM DF image to get the number density distribution and averaged size of Frank loop with irradiation depth range from 0 to 1000 nm. **Fig. 5.9** shows the Frank loop number density (N.D.) distribution and the combined contribution of both N.D. and average size (d_{Ave}) in 316L SS, $CrCu_{0.3}FeNi$ and $Al_{0.4}CrCuFeNi_2$ HEAs.

From **Fig. 5.9**, it seems that 316L tends to show a higher loop number density than HEAs in a shallower depth (before 800 nm) while HEAs present a lower distribution. On the other hand, HEAs shows an increase of number density with irradiation depth increased. Note from the damage distribution profile, the dpa value increased from 5dpa on the top surface to about 12 dpa at 1 μm. Based on the damage peak of HEAs and 316L, the saturation depth of Frank loop in HEAs could be deeper than 316L. However, the single indentation of 250 nm could induce a defect area around 1-1.5 μm, which may not include the entire irradiation zone of HEAs, resulting in a relative lower measured hardness value than 316L.

Table 5.4 Nano-indentation hardness and hardening of the alloys.

Hardness (GPa)	**316L**	**$Cu_{0.3}CrFeNi$**	**$Al_{0.4}CrCuFeNi_2$**
H_{unirr}	1.42	1.55	2.58
H_{irr}	3.58	3.87	4.78
ΔH	2.16	2.32	2.2

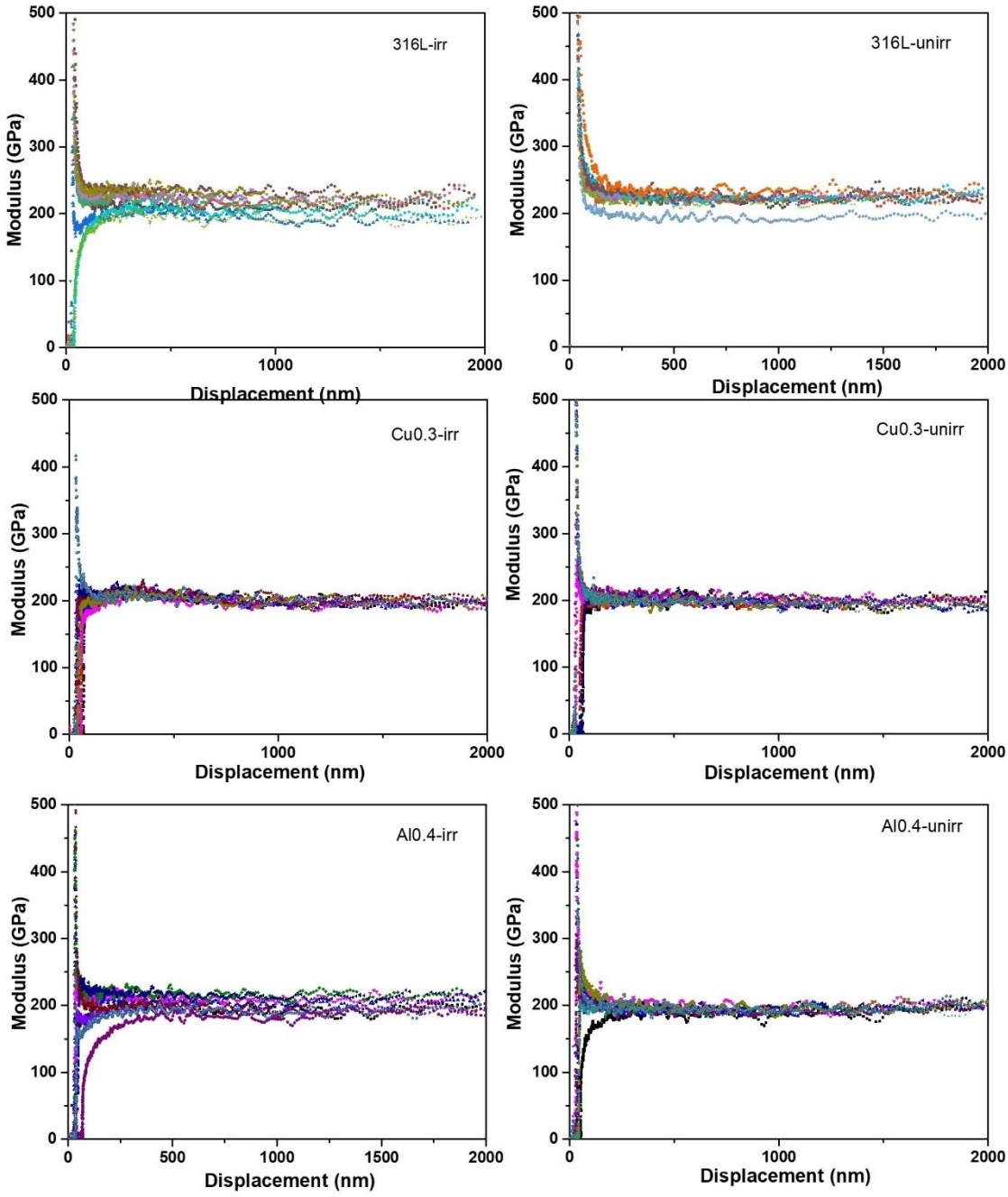

Fig. 5.7 Indentation modulus of 316L SS, $CrCu_{0.3}FeNi$ and $Al_{0.4}CrCuFeNi_2$ HEAs.

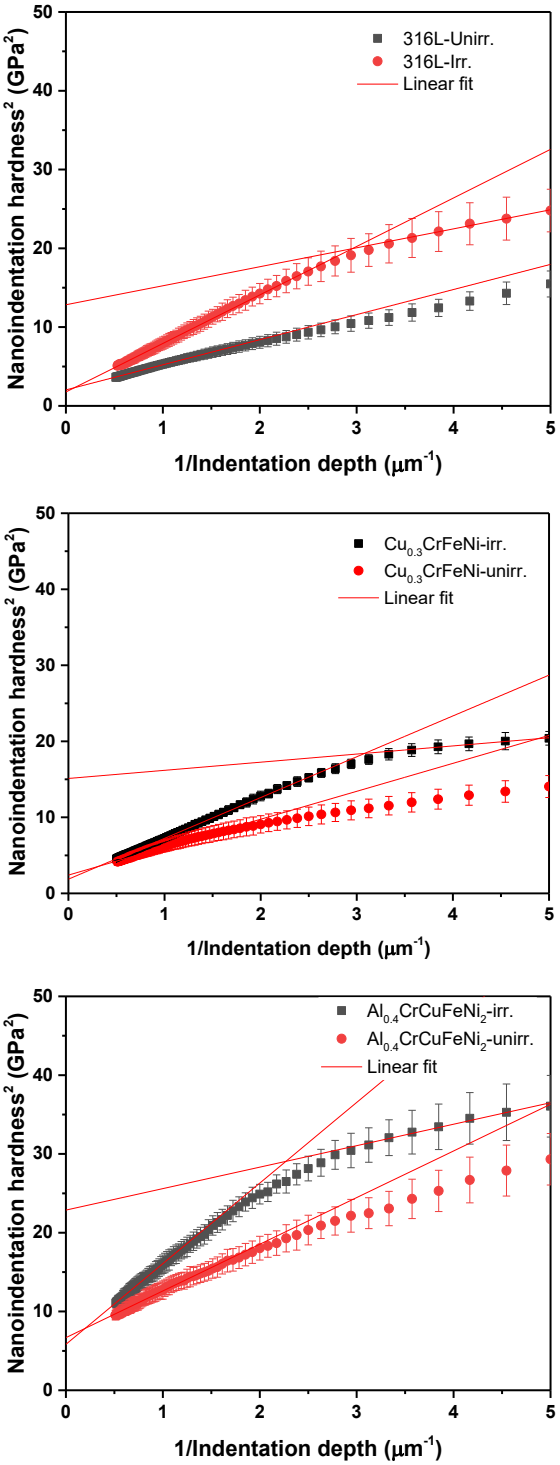

Fig. 5.8 Nix-Gao plots of 316L SS, $CrCu_{0.3}FeNi$ and $Al_{0.4}CrCuFeNi_2$ HEAs.

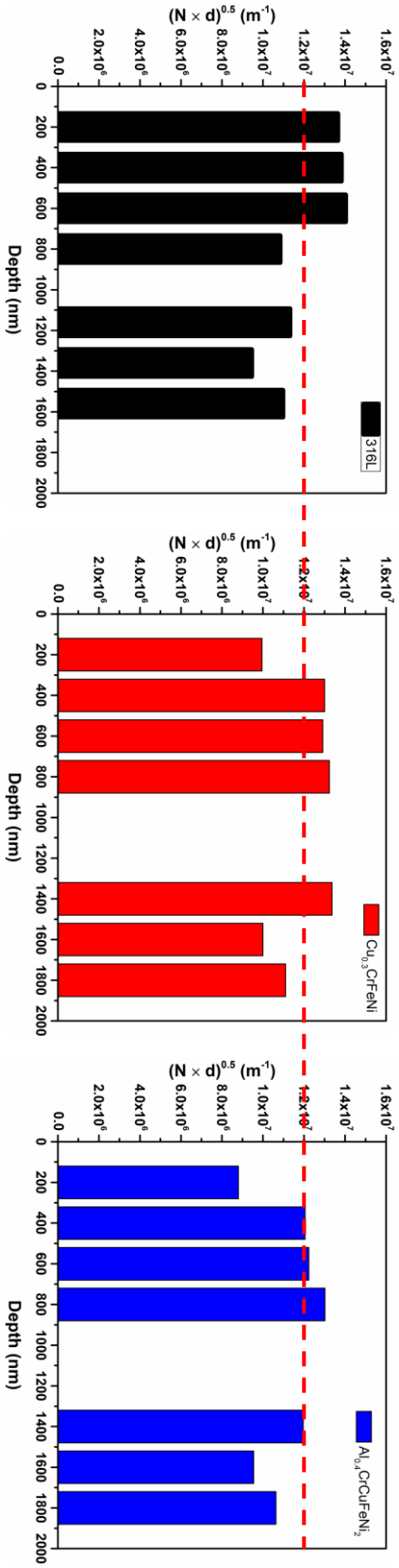

Fig. 5.9 Frank loop number density and average size distribution (N.D.*d_{Ave}) of 316L, $CrCu_{0.3}FeNi$ and $Al_{0.4}CrCuFeNi_2$ HEAs.

5.4 Summary

The irradiation effects of $CrCu_{0.3}FeNi$ and $Al_{0.4}CrCuFeNi_2$ HEAs were evaluated by comparison with commercial 316L SS, and the irradiation-induced hardening were correlated with the irradiated microstructure by TEM observation. The specimens were irradiated with 6.4 MeV Fe^{3+} at 300 ℃ to a nominal damage peak of about 23 dpa at 1.5 μm using DuET facility. The surface morphology of the irradiated and unirradiated region acquired by atomic force microscope (AFM) shows a significant decrease in step height from 7.2 nm in 316L to 4.6 nm in CrCu0.3FeNi, indicating a higher swelling resistance of HEA. Nano-indentation experiments at a depth of 250 nm show that $Al_{0.4}CrCuFeNi_2$ HEA exhibit lower irradiation hardening (0.8GPa) than 316L (1.5GPa), while the nano-indentation using continuous stiffness measurement (CSM) show that the irradiation induced hardening of HEAs are comparable with 316 SS. The transmission electron microscope (TEM) microstructure observation by dark field images taken from the relrod of each specimen suggests that the HEAs have close averaged number density of Frank loop with 316L in the whole damage region. However, 316L tends to show a higher loop number density than HEAs in a shallower depth while HEAs present a wider damage distribution and larger amount of defects than 316L in deeper irradiation area, which is consistent with the higher irradiation hardening tested by single depth indentation and a similar hardening behavior by CSM indentation. The consistency between the measured hardening and corresponding defect microstructure observed indicate a comparable irradiation resistance of $CrCu_{0.3}FeNi$ and $Al_{0.4}CrCuFeNi_2$ HEAs with 316L in the current irradiation condition.

Chapter 6 Conclusions

Conclusions

In order to explore new materials for advanced nuclear reactors application, the Co-free Cu containing concentrated solid solution alloys (CSSAs) and high entropy alloys (HEAs) were developed and the oxidation behavior and irradiation resistance of these alloys were evaluated. The experimental results can be concluded as follows:

(1) Oxidation behavior of Co-free CSSAs and HEAs

According to the mass gain curves and the characterization of oxide scales of CuNi, CuNiFe, $Cu_{0.3}CrFeNi$, $Al_{0.4}CrCuFeNi_2$ HEAs and 316 SS, Co-free Cu containing alloys show better oxidation resistance than 316 SS under 500 - 700°C steam oxidation. The addition of Fe significantly decreased the oxidation resistance of CuNi alloy even it contains high Ni. The element of Cr and Al is contributing to the protective scale formation, and the parabolic rate constant shows a significant decrease at high temperatures. $Al_{0.4}CrCuFeNi_2$ HEAs exhibits the best oxidation resistance due to the formation of external Cr_2O_3 and Al_2O_3 scales.

To further evaluate the effect of Al on oxidation behavior of Co-free HEAs, oxidation test at 700°C for 100 h were conducted on $Al_xCrCuFeNi_2$ HEAs. Detailed observation by STEM-EDS mappings revealed that the sufficient Al content for protective Al_2O_3 formation should be higher than 4 at% ($Al_{0.2}CrCuFeNi_2$). The analysis of short-term oxidation indicates that the early formation of continuous Al_2O_3 scale in the initial stage of oxidation contributes to the enhanced oxidation resistance of high Al content alloys.

(2) Irradiation effects of Co-free HEAs

Irradiation effects of $CrCu_{0.3}FeNi$ and $Al_{0.4}CrCuFeNi_2$ HEAs were evaluated by comparison with commercial 316L SS. The surface morphology acquired by AFM shows a significant decrease in step height from 316L $CrCu_{0.3}FeNi$ HEA, indicating a lower swelling rate of HEA. Nano-indentation experiments at a depth of 250 nm show that $Al_{0.4}CrCuFeNi_2$ HEA exhibit lower irradiation hardening (0.8GPa) than 316L (1.5GPa), while the continuous stiffness measurement show that the irradiation induced hardening of HEAs are comparable with 316 SS. The TEM microstructure observation by dark field images taken from the relrod of each specimen explains the difference by two indentation methods. In the whole damage region, $CrCu_{0.3}FeNi$ and $Al_{0.4}CrCuFeNi_2$ HEAs have close averaged number density of Frank loop with 316L.

However, a higher loop number density of 316L than HEAs were found in a shallower depth before 800 nm while HEAs present a wider damage distribution and larger amount of defects than 316L in deeper irradiation area. The lower irradiation hardness of HEAs in single depth indentation may not include the entire irradiation zone of HEAs, resulting in a relative lower measured hardness value than 316L.

In conclusion, the Co-free $Al_xCrCuFeNi_2$ HEAs shows better high temperature oxidation resistance and comparable irradiation resistance with conventional alloy, which could be candidate materials for advanced reactors.

References

[1] V. Knapp, D. Pevec, Promises and limitations of nuclear fission energy in combating climate change, Energy Policy, 120 (2018) 94-99.

[2] S.J. Zinkle, G.S. Was, Materials challenges in nuclear energy, Acta Mater., 61 (2013) 735-758.

[3] P. Dubuisson, D. Gilbon, J.L. Séran, Microstructural evolution of ferritic-martensitic steels irradiated in the fast breeder reactor Phénix, J. Nucl. Mater., 205 (1993) 178-189.

[4] M.B. Toloczko, F.A. Garner, C.R. Eiholzer, Irradiation creep and swelling of the US fusion heats of HT9 and 9Cr-1Mo to 208 dpa at ~ 400°C, J. Nucl. Mater., 212-215 (1994) 604-607.

[5] F.A. Garner, M.B. Toloczko, B.H. Sencer, Comparison of swelling and irradiation creep behavior of fcc-austenitic and bcc-ferritic/martensitic alloys at high neutron exposure, J. Nucl. Mater., 276 (2000) 123-142.

[6] B. Cantor, I.T.H. Chang, P. Knight, A.J.B. Vincent, Microstructural development in equiatomic multicomponent alloys, Materials Science and Engineering: A, 375-377 (2004) 213-218.

[7] P.K. Huang, J.W. Yeh, T.T. Shun, S.K. Chen, Multi-principal-element alloys with improved oxidation and wear resistance for thermal spray coating, Advanced Engineering Materials, 6 (2004) 74-78.

[8] Y. Zhang, T.T. Zuo, Z. Tang, M.C. Gao, K.A. Dahmen, P.K. Liaw, Z.P. Lu, Microstructures and properties of high-entropy alloys, Prog Mater Sci, 61 (2014) 1-93.

[9] D.B. Miracle, O.N. Senkov, A critical review of high entropy alloys and related concepts, Acta Mater., 122 (2017) 448-511.

[10] B. Cantor, Multicomponent high-entropy Cantor alloys, Prog Mater Sci, (2020).

[11] J.W. Yeh, S.K. Chen, S.J. Lin, J.Y. Gan, T.S. Chin, T.T. Shun, C.H. Tsau, S.Y. Chang, Nanostructured High-Entropy Alloys with Multiple Principal Elements: Novel Alloy Design Concepts and Outcomes, Advanced Engineering Materials, 6 (2004) 299-303.

[12] B. Gludovatz, A. Hohenwarter, D. Catoor, E.H. Chang, E.P. George, R.O. Ritchie, A fracture-resistant high-entropy alloy for cryogenic applications, Science, 345 (2014) 1153-1158.

[13] F. Otto, A. Dlouhý, C. Somsen, H. Bei, G. Eggeler, E.P. George, The influences of temperature and microstructure on the tensile properties of a CoCrFeMnNi high-entropy alloy, Acta Mater., 61 (2013) 5743-5755.

[14] J.Y. He, W.H. Liu, H. Wang, Y. Wu, X.J. Liu, T.G. Nieh, Z.P. Lu, Effects of Al addition on structural evolution and tensile properties of the FeCoNiCrMn high-entropy alloy system, Acta Mater., 62 (2014) 105-113.

[15] T.-T. Shun, Y.-C. Du, Microstructure and tensile behaviors of FCC $Al_{0.3}$CoCrFeNi high entropy alloy, J. Alloy. Compd., 479 (2009) 157-160.

[16] J.Y. He, H. Wang, H.L. Huang, X.D. Xu, M.W. Chen, Y. Wu, X.J. Liu, T.G. Nieh, K. An, Z.P. Lu, A precipitation-hardened high-entropy alloy with outstanding tensile properties, Acta Mater., 102 (2016) 187-196.

[17] Y.J. Liang, L. Wang, Y. Wen, B. Cheng, Q. Wu, T. Cao, Q. Xiao, Y. Xue, G. Sha, Y. Wang, Y. Ren, X. Li, L. Wang, F. Wang, H. Cai, High-content ductile coherent nanoprecipitates achieve ultrastrong high-entropy alloys, Nat Commun, 9 (2018) 4063.

[18] S. Guo, C. Ng, C.T. Liu, Anomalous solidification microstructures in Co-free

$Al_xCrCuFeNi_2$ high-entropy alloys, J. Alloy. Compd., 557 (2013) 77-81.
[19] C. Ng, S. Guo, J. Luan, Q. Wang, J. Lu, S. Shi, C.T. Liu, Phase stability and tensile properties of Co-free $Al_{0.5}CrCuFeNi_2$ high-entropy alloys, J. Alloy. Compd., 584 (2014) 530-537.
[20] B. Gwalani, D. Choudhuri, V. Soni, Y. Ren, M. Styles, J.Y. Hwang, S.J. Nam, H. Ryu, S.H. Hong, R. Banerjee, Cu assisted stabilization and nucleation of $L1_2$ precipitates in $Al_{0.3}CuFeCrNi_2$ fcc-based high entropy alloy, Acta Mater., 129 (2017) 170-182.
[21] B. Gwalani, V. Soni, D. Choudhuri, M. Lee, J.Y. Hwang, S.J. Nam, H. Ryu, S.H. Hong, R. Banerjee, Stability of ordered $L1_2$ and B_2 precipitates in face centered cubic based high entropy alloys - $Al_{0.3}CoFeCrNi$ and $Al_{0.3}CuFeCrNi_2$, Scr. Mater., 123 (2016) 130-134.
[22] L. Guo, W. Wu, S. Ni, Z. Wang, M. Song, Effects of annealing on the microstructural evolution and phase transition in an $AlCrCuFeNi_2$ high-entropy alloy, Micron, 101 (2017) 69-77.
[23] Y.X. Liu, C.Q. Cheng, J.L. Shang, R. Wang, P. Li, J. Zhao, Oxidation behavior of high-entropy alloys $Al_xCoCrFeNi$ (x=0.15, 0.4) in supercritical water and comparison with HR3C steel, Trans. Nonferrous Met. Soc. China, 25 (2015) 1341-1351.
[24] A. Mohanty, J.K. Sampreeth, O. Bembalge, J.Y. Hascoet, S. Marya, R.J. Immanuel, S.K. Panigrahi, High temperature oxidation study of direct laser deposited $Al_xCoCrFeNi$ (X=0.3,0.7) high entropy alloys, Surf. Coat. Technol., 380 (2019) 125028.
[25] W. Kai, F.P. Cheng, Y.R. Lin, C.W. Chuang, R.T. Huang, D. Chen, J.J. Kai, C.T. Liu, C.J. Wang, The oxidation behavior of Ni2FeCoCrAlx high-entropy alloys in dry air, J. Alloy. Compd., 836 (2020).
[26] M. He, H. Kang, S. Lin, Y. Liu, P. Zhang, W. Qin, X. Wu, Impressive high-temperature oxidation resistance of FeCrNiMnAl high entropy alloy coating on the ferritic/martensitic steel with primordial Al2O3 and Mn3O4 gradient films, J. Alloy. Compd., 928 (2022).
[27] K. Yabuuchi, R. Kasada, A. Kimura, Effect of alloying elements on irradiation hardening behavior and microstructure evolution in BCC Fe, J. Nucl. Mater., 442 (2013) S790-S795.
[28] W.-Y. Chen, X. Liu, Y. Chen, J.-W. Yeh, K.-K. Tseng, K. Natesan, Irradiation effects in high entropy alloys and 316H stainless steel at 300 °C, J. Nucl. Mater., 510 (2018) 421-430.
[29] W.-Y. Chen, M.A. Kirk, N. Hashimoto, J.-W. Yeh, X. Liu, Y. Chen, Irradiation effects on $Al_{0.3}CoCrFeNi$ and CoCrMnFeNi high-entropy alloys, and 316H stainless steel at 500 °C, J. Nucl. Mater., 539 (2020) 152324.
[30] N. Hashimoto, E. Wada, H. Oka, Effect of stacking fault energy on irradiation damage in reduced activation high entropy alloys, J. Nucl. Mater., 566 (2022).
[31] N. Hashimoto, T. Fukushi, E. Wada, W.Y. Chen, Effect of stacking fault energy on damage microstructure in ion-irradiated CoCrFeNiMn concentrated solid solution alloys, J. Nucl. Mater., 545 (2021).
[32] J. Du, S. Jiang, P. Cao, C. Xu, Y. Wu, H. Chen, E. Fu, Z. Lu, Superior radiation tolerance via reversible disordering-ordering transition of coherent superlattices, Nat Mater, (2022).
[33] O. Ahmed, D.J. Young, Precipitate Distributions in Internally Carburised and Oxidised Fe-Cr Alloys, in: M. McNallan (Ed.) High Temperature Corrosion and

Materials Chemistry II, The Electrochemical Society, 2000, pp. 77-92.
[34] D.J. Young, Alloy Oxidation II, in: K. Marinakis (Ed.) High Temperature Oxidation and Corrosion of Metals, Elsevier, Oxford, 2016, pp. 261-333.
[35] D.B. Williams, C.B. Carter, Amplitude contrast, Transmission electron microscopy: a textbook for materials science, (2009) 371-388.
[36] D.B. Williams, C.B. Carter, Diffraction from Small Volumes, Transmission Electron Microscopy: A Textbook for Materials Science, (2009) 271-282.
[37] D.J. Edwards, E.P. Simonen, S.M. Bruemmer, Evolution of fine-scale defects in stainless steels neutron-irradiated at 275 °C, J. Nucl. Mater., 317 (2003) 13-31.
[38] W.C. Oliver, G.M. Pharr, An improved technique for determining hardness and elastic modulus using load and displacement sensing indentation experiments, J. Mater. Res., 7 (2011) 1564-1583.
[39] G.M. Pharr, E.G. Herbert, Y. Gao, The Indentation Size Effect: A Critical Examination of Experimental Observations and Mechanistic Interpretations, Annual Review of Materials Research, 40 (2010) 271-292.
[40] W.D. Nix, H. Gao, Indentation size effects in crystalline materials: A law for strain gradient plasticity, Journal of the Mechanics and Physics of Solids, 46 (1998) 411-425.
[41] G.S. Was, Irradiation hardening and deformation, in: Fundamentals of radiation materials science: metals and alloys, springer, 2016, pp. 669-733.
[42] M.M. Rahman, J. Dongxu, N. Jahan, M. Salvatores, J. Zhao, Design concepts of supercritical water-cooled reactor (SCWR) and nuclear marine vessel: A review, Progress in Nuclear Energy, 124 (2020) 103320.
[43] K. Dobashi, A. Kimura, Y. Oka, S. Koshizuka, Conceptual design of a high temperature power reactor cooled and moderated by supercritical light water, Annals of Nuclear Energy, 25 (1998) 487-505.
[44] B. Cantor, Multicomponent and High Entropy Alloys, Entropy, 16 (2014) 4749-4768.
[45] M.-H. Tsai, J.-W. Yeh, High-entropy alloys: a critical review, Materials Research Letters, 2 (2014) 107-123.
[46] Z. Rao, X. Wang, Q. Wang, T. Liu, X. Chen, L. Wang, X. Hui, Microstructure, Mechanical Properties, and Oxidation Behavior of AlxCr0.4CuFe0.4MnNi High Entropy Alloys Advanced Engineering Materials, 19 (2017) 1600726.
[47] Y. Yu, N. Xu, S. Zhu, Z. Qiao, J. Zhang, J. Yang, W. Liu, A novel Cu-doped high entropy alloy with excellent comprehensive performances for marine application, J. Mater. Sci. Technol., 69 (2021) 48-59.
[48] Z.H. Han, S. Liang, J. Yang, R. Wei, C.J. Zhang, A superior combination of strength-ductility in CoCrFeNiMn high-entropy alloy induced by asymmetric rolling and subsequent annealing treatment, Materials Characterization, 145 (2018) 619-626.
[49] S.J. Sun, Y.Z. Tian, H.R. Lin, X.G. Dong, Y.H. Wang, Z.J. Zhang, Z.F. Zhang, Enhanced strength and ductility of bulk CoCrFeMnNi high entropy alloy having fully recrystallized ultrafine-grained structure, Mater. Des., 133 (2017) 122-127.
[50] K.Y. Tsai, M.H. Tsai, J.W. Yeh, Sluggish diffusion in Co–Cr–Fe–Mn–Ni high-entropy alloys, Acta Mater., 61 (2013) 4887-4897.
[51] H.S. Grewal, R.M. Sanjiv, H.S. Arora, R. Kumar, A. Ayyagari, S. Mukherjee, H. Singh, Activation Energy and High Temperature Oxidation Behavior of Multi-Principal Element Alloy, Advanced Engineering Materials, 19 (2017) 1700182.
[52] J. Chen, X. Zhou, W. Wang, B. Liu, Y. Lv, W. Yang, D. Xu, Y. Liu, A review on

fundamental of high entropy alloys with promising high-temperature properties, J. Alloy. Compd., 760 (2018) 15-30.
[53] R. Wang, Y. Tang, S. Li, Y. Ai, Y. Li, B. Xiao, L.a. Zhu, X. Liu, S. Bai, Effect of lattice distortion on the diffusion behavior of high-entropy alloys, J. Alloy. Compd., 825 (2020).
[54] S.-T. Chen, W.-Y. Tang, Y.-F. Kuo, S.-Y. Chen, C.-H. Tsau, T.-T. Shun, J.-W. Yeh, Microstructure and properties of age-hardenable AlxCrFe1.5MnNi0.5 alloys, Materials Science and Engineering: A, 527 (2010) 5818-5825.
[55] G.R. Holcomb, J. Tylczak, C. Carney, Oxidation of CoCrFeMnNi High Entropy Alloys, Jom, 67 (2015) 2326-2339.
[56] N.K. Adomako, J.H. Kim, Y.T. Hyun, High-temperature oxidation behaviour of low-entropy alloy to medium- and high-entropy alloys, Journal of Thermal Analysis and Calorimetry, 133 (2018) 13-26.
[57] S.-Y. Cheng, S.-L. Kuan, W.-T. Tsai, Effect of water vapor on annealing scale formation on 316 SS, Corrosion Science, 48 (2006) 634-649.
[58] C. Stephan-Scherb, W. Schulz, M. Schneider, S. Karafiludis, G. Laplanche, High-Temperature Oxidation in Dry and Humid Atmospheres of the Equiatomic CrMnFeCoNi and CrCoNi High- and Medium-Entropy Alloys, Oxidation of Metals, 95 (2020) 105-133.
[59] Y. Lei, N. Hashimoto, S. Isobe, Cu-Containing High Entropy Alloys for Nuclear Fusion Application, Materials Transactions, 61 (2020) 1247-1251.
[60] A. Gusarov, C. Pohl, T. Pfalz, R.-W. Bosch, S. Van Dyck, V. Barabash, R. Eaton, F. Zacchia, H. Samuli, Assessment of creep in reactor-irradiated CuCrZr alloy intended for the ITER first wall panels, Fusion Eng. Des., 137 (2018) 112-123.
[61] M. Li, P. Hu, Y. Zhang, Y. Chang, Enhancing performance of the CuCrZrTiV alloys through increasing recrystallization resistance and two-step thermomechanical treatments, J. Nucl. Mater., 543 (2021).
[62] S. Hayashi, D. Kudo, R. Nagashima, H. Utsumi, Effect of Cu on oxidation behaviour of FCC Fe-Ni-Cr-Al and Ni-Cr-Al based alloys, Corrosion Science, 163 (2020) 108273.
[63] S. Hayashi, T. Narita, Competitive Effect of Water Vapor and Oxygen on the Oxidation of Fe–5 wt.% Al Alloy at 1073 K, Oxidation of Metals, 56 (2001) 251-270.
[64] G. Laplanche, U.F. Volkert, G. Eggeler, E.P. George, Oxidation Behavior of the CrMnFeCoNi High-Entropy Alloy, Oxidation of Metals, 85 (2016) 629-645.
[65] W.J. Quadakkers, D. Naumenko, E. Wessel, V. Kochubey, L. Singheiser, Growth Rates of Alumina Scales on Fe–Cr–Al Alloys, Oxidation of Metals, 61 (2004) 17-37.
[66] H. Hu, Z. Zhou, M. Li, L. Zhang, M. Wang, S. Li, C. Ge, Study of the corrosion behavior of a 18Cr-oxide dispersion strengthened steel in supercritical water, Corrosion Science, 65 (2012) 209-213.
[67] G.S. Was, P. Ampornrat, G. Gupta, S. Teysseyre, E.A. West, T.R. Allen, K. Sridharan, L. Tan, Y. Chen, X. Ren, C. Pister, Corrosion and stress corrosion cracking in supercritical water, J. Nucl. Mater., 371 (2007) 176-201.
[68] L. Jian, C.Y. Yuh, M. Farooque, Oxidation behavior of superalloys in oxidizing and reducing environments, Corrosion Science, 42 (2000) 1573-1585.
[69] F. Garner, Radiation damage in austenitic steels, in: K. R.J.M. (Ed.) Comprehensive Nuclear Materials, Elsevier, Oxford, 2012, pp. 33-95.
[70] D. Chen, S. Zhao, J. Sun, P. Tai, Y. Sheng, Y. Zhao, G. Yeli, W. Lin, S. Liu, W. Kai,

J.-J. Kai, Diffusion controlled helium bubble formation resistance of FeCoNiCr high-entropy alloy in the half-melting temperature regime, J. Nucl. Mater., 526 (2019) 151747.
[71] S. Praveen, H.S. Kim, High-Entropy Alloys: Potential Candidates for High-Temperature Applications - An Overview, Advanced Engineering Materials, 20 (2018) 1700645.
[72] A. Gali, E.P. George, Tensile properties of high- and medium-entropy alloys, Intermetallics, 39 (2013) 74-78.
[73] Z. Wu, H. Bei, G.M. Pharr, E.P. George, Temperature dependence of the mechanical properties of equiatomic solid solution alloys with face-centered cubic crystal structures, Acta Mater., 81 (2014) 428-441.
[74] G. Laplanche, A. Kostka, O.M. Horst, G. Eggeler, E.P. George, Microstructure evolution and critical stress for twinning in the CrMnFeCoNi high-entropy alloy, Acta Mater., 118 (2016) 152-163.
[75] B. Schuh, F. Mendez-Martin, B. Volker, E.P. George, H. Clemens, R. Pippan, A. Hohenwarter, Mechanical properties, microstructure and thermal stability of a nanocrystalline CoCrFeMnNi high-entropy alloy after severe plastic deformation, Acta Mater., 96 (2015) 258-268.
[76] T. Borkar, B. Gwalani, D. Choudhuri, C.V. Mikler, C.J. Yannetta, X. Chen, R.V. Ramanujan, M.J. Styles, M.A. Gibson, R. Banerjee, A combinatorial assessment of $Al_xCrCuFeNi_2$ ($0 < x < 1.5$) complex concentrated alloys: Microstructure, microhardness, and magnetic properties, Acta Mater., 116 (2016) 63-76.
[77] X. Huang, L. Huang, H. Peng, Y. Liu, B. Liu, S. Li, Enhancing strength-ductility synergy in a casting non-equiatomic NiCoCr-based high-entropy alloy by Al and Ti combination addition, Scr. Mater., 200 (2021) 113898.
[78] D. Li, C. Li, T. Feng, Y. Zhang, G. Sha, J.J. Lewandowski, P.K. Liaw, Y. Zhang, High-entropy $Al_{0.3}CoCrFeNi$ alloy fibers with high tensile strength and ductility at ambient and cryogenic temperatures, Acta Mater., 123 (2017) 285-294.
[79] A.M. Manzoni, U. Glatzel, New multiphase compositionally complex alloys driven by the high entropy alloy approach, Materials Characterization, 147 (2019) 512-532.
[80] D.J. Young, Oxidation of Alloys I, in: K. Marinakis (Ed.) High Temperature Oxidation and Corrosion of Metals, Elsevier, Oxford, 2016, pp. 193-260.
[81] P. Tomaszewicz, G.R. Wallwork, The Oxidation of Fe-Al Alloys Containing Chromium, Nickel, or Manganese, Corrosion, 40 (1984) 152-157.
[82] B. Gleeson, High-Temperature Corrosion of Metallic Alloys and Coatings, in: Materials Science and Technology: A Comprehensive Treatment, 2000, pp. 173-228.
[83] P. Bi, N. Hashimoto, S. Hayashi, H. Oka, S. Isobe, Oxidation Behavior of Cu-Containing Concentrated Solid Solution Alloys under Steam Conditions, Materials Transactions, 62 (2021) 1716-1723.
[84] G. Huang, J. Wu, R. Yuan, Y. Li, F. Meng, P. Lei, C. Lu, F. Cao, Y. Shen, High temperature oxidation behavior and mechanism of $Al_{0.3}CuCrFeNi_2$ high-entropy alloy with a coherent γ/γ' microstructure, Corrosion Science, 195 (2022) 109984.
[85] W. Zhao, Y. Kang, J.M.A. Orozco, B. Gleeson, Quantitative Approach for Determining the Critical Volume Fraction for the Transition from Internal to External Oxidation, Oxidation of Metals, 83 (2014) 187-201.
[86] C.S. Giggins, F.S. Pettit, Oxidation of Ni-Cr-Al Alloys between 1000 ° and 1200 °C, J. Electrochem. Soc., 118 (1971) 1782-1790.

[87] T.M. Butler, J.P. Alfano, R.L. Martens, M. Weaver, High-Temperature Oxidation Behavior of Al-Co-Cr-Ni-(Fe or Si) Multicomponent High-Entropy Alloys, Jom, 67 (2015) 246-259.
[88] J. Dabrowa, G. Cieslak, M. Stygar, K. Mroczka, K. Berent, T. Kulik, M. Danielewski, Influence of Cu content on high temperature oxidation behavior of $AlCoCrCu_xFeNi$ high entropy alloys (x=0; 0.5; 1), Intermetallics, 84 (2017) 52-61.
[89] T.L. Barth, E.A. Marquis, The Effect of Ti on the Early Stages of Oxidation of an Alumina-Forming NiCrAl Alloy, Oxidation of Metals, 92 (2019) 13-26.
[90] S. Yoneda, S. Hayashi, I. Saeki, S. Ukai, Investigation of Initial Transient Oxidation of Fe–xCr–6at.%Al Alloys Using Synchrotron Radiation During Heating to 1000 °C in Air, Oxidation of Metals, 86 (2016) 357-370.
[91] C. Lu, L. Niu, N. Chen, K. Jin, T. Yang, P. Xiu, Y. Zhang, F. Gao, H. Bei, S. Shi, M.R. He, I.M. Robertson, W.J. Weber, L. Wang, Enhancing radiation tolerance by controlling defect mobility and migration pathways in multicomponent single-phase alloys, Nat Commun, 7 (2016) 13564.
[92] C. Fu, J. Li, J. Bai, Y. Li, Q. Chen, G. Lei, J. Lin, Z. Zhu, Y. Meng, Effect of helium bubbles on irradiation hardening of additive manufacturing 316L stainless steel under high temperature He ions irradiation, J. Nucl. Mater., 550 (2021).

Academic Achievements

Journal Articles

1. **Peng Bi**, Naoyuki Hashimoto, Shigenari Hayashi, Hiroshi Oka, Shigehito Isobe. Oxidation Behavior of Cu-Containing Concentrated Solid Solution Alloys under Steam Conditions, *Materials Transactions* 62 (2021) 1716-1723.
2. **Peng Bi**, Naoyuki Hashimoto, Shigenari Hayashi, Hiroshi Oka, Shigehito Isobe. Effect of Al on oxidation behavior of $Al_xCrCuFeNi_2$ (x = 0.2, 0.4, 0.6) high entropy alloys, *Corrosion Science* 208 (2022) 110697.

Presentations on conferences

1. 2020.9.15-18, JIM 2020 autumn meeting (online, general oral session).
2. 2020.10. 23-26, The Nuclear Materials Conference (NuMat. 2020, online poster).
3. 2020.11. 06, HU-SNU Symposium 2020 (online, oral session).
4. 2021.9. 14-17, JIM 2021 autumn meeting (online, general oral session)
5. 2021.12.7, Japanese Microscopy meeting, Hokkaido brunch (Online, poster)
6. 2021.11. 24-29, ICFRM-20 conference (online, poster)
7. 2022.3.15-17, JIM 2022 spring meeting (online, oral session)
8. 2022.9.20-23, JIM 2022 autumn meeting (Fukuoka, general oral session).
9. 2022.11.19, Japanese Microscopy meeting Hokkaido brunch (Sapporo, oral session)